A Study of
Alternative Gas Mixtures of RPC
&
Different Aspects of Neutrino Oscillation
for ICAL at INO

By

JAYDEEP DATTA

PHYS01201504022

Bhabha Atomic Research Center

A thesis submitted to the
Board of Studies in Physical Sciences

In partial fulfillment of requirements
for the Degree of

DOCTOR OF PHILOSOPHY
of
HOMI BHABHA NATIONAL INSTITUTE

April 2021

Homi Bhabha National Institute

Recommendations of the Viva Voce Committee

As members of the Viva Voce Committee, we certify that we have read the dissertation prepared by **Jaydeep Datta** entitled **"A Study of Alternative Gas Mixtures of RPC & Different Aspects of Neutrino Oscillation for ICAL at INO"** and recommend that it may be accepted as fulfilling the thesis requirement for the award of Degree of Doctor of Philosophy.

Chairman - Prof. Supratik Mukhopadhyay *Supratik Mukhopadhyay*	**Date:** 28/07/2021
Guide / Convener - Prof. Nayana Majumdar *Nayana Majumdar*	**Date:** 28/07/2021
Co-guide / Co-convener - Prof. Sankagiri Umasankar *S. Umasankar*	**Date:** 28/07/2021
Examiner - Prof. James Libby	**Date:** 28/7/2021
Member 1 - Prof. Amol Dighe *Amol Dighe*	**Date:** 28/07/2021
Member 2 - Prof. Gobinda Majumder *Gobinda Majumder*	**Date:** 28/07/2021
Member 3 - Dr. Satyanarayan Bheesette	**Date:** 28/07/2021

  Final approval and acceptance of this thesis is contingent upon the candidate's submission of the final copies of the thesis to HBNI.

  We hereby certify that we have read this thesis prepared under our direction and recommend that it may be accepted as fulfilling the thesis requirement.

Date: July 28, 2021

Place: SINP, Kolkata **Prof. S. Umasankar** (Coguide) **Prof. N. Majumdar** (Guide)

STATEMENT BY THE AUTHOR

This dissertation has been submitted in partial fulfillment of requirements for an advanced degree at Homi Bhabha National Institute (HBNI) and is deposited in the library to be made available to borrowers under rules of the HBNI.

Brief quotations from this dissertation are allowable without special permission, provided that accurate acknowledgement of source is made. Requests for permission for extended quotation from or reproduction of this manuscript in whole or in part may be granted by the Competent Authority of HBNI when in his or her judgment the proposed use of the material is in the interests of scholarship. In all other instances, however, permission must be obtained from the author.

July 28, 2021

Kolkata

Jaydeep Datta

DECLARATION

I hereby declare that the investigation presented in the thesis has been carried out by me. The work is original and has not been submitted earlier as a whole or in part for a degree/diploma at this or any other Institution/University.

July 28, 2021

Kolkata

Jaydeep Datta

List of Publications Arising from the Thesis

Publications in Refereed Journal

Published

1. *Matter vs Vacuum Oscillation in Atmospheric Neutrinos*, **J. Datta**, M. Nizam, A. Ajmi and S. Umasankar, *Nuclear Physics B*, **961**, 11521 (2020).

2. *Study of Streamer development in Resistive Plate Chamber*, **J. Datta**, S. Tripathy, N. Majumdar and S. Mukhopadhyay, *Journal of Instrumentation*, **15**, C12006 (2020).

3. *Numerical Qualification of Eco-Friendly Gas Mixtures for Avalanche-Mode Operation of Resistive Plate Chambers in INO-ICAL*, **J. Datta**, S. Tripathy, N. Majumdar and S. Mukhopadhyay, *Journal of Instrumentation*, **16**, P07012 (2021).

Under Preparation

1. *Determination of Neutrino Oscillation Parameters Using Track and Non-Track Hit Information from GEANT4*, **J.Datta**, B.Singh and S. Umasankar

Symposium and Conference Proceedings

1. *Qualification of Eco-Friendly Gas Mixture for Avalanche Mode Operation of RPC*, **J. Datta**, A. Jash, N. Majumdar, S. Mukhopadhyay, *"Advanced Detectors for Nuclear, High Energy and Astroparticle Physics"*, **Chapter 12**, Springer Proceedings, 2018.

Conferences

Oral Presentation

1. *Qualification of Eco-friendly Gas Mixture for Avalanche Mode Operation of RPC*, Advanced Detectors in Nuclear, High Energy, Astroparticle Physics **ADNHEAP 2017**, February 15-17, 2017, Bose Institute, Kolkata, India.

2. *Modelling of Avalanches and Streamers in Resistive Plate Chambers*, International Conference on Mathematical Modelling and Scientific Computing **ICMMSC 2018**, July 19-21, 2018, Indian Institute of Technology, Indore, India.

3. *Study of Streamer Development in Resistive Plate Chamber*, XV Workshop on Resistive Plate Chambers and Related Detectors, **RPC 2020**, February

10-14, 2020, University of Rome, Tor Vergata, Italy (Awarded the best oral presentation).

4. *Matter vs Vacuum Oscillation in Atmospheric Neutrinos*, 40th International Conference on High Energy Physics, **ICHEP 2020**, July 28 - August 6, 2020, Online Conference, Prague

Poster Presentation

1. *Matter vs. Vacuum Oscillations Atmospheric Neutrinos*, XXIX International Conference on Neutrino Physics and Astrophysics, **Neutrino 2020**, Online conference, Chicago (USA), June 22 - July 2 (2020).

2. *Neutrino oscillation parameter determination at INO-ICAL using track and non-track hit information from GEANT*, XIV DAE-BRNS High Energy Physics Symposium, **DAE-HEP**, Online Conference, Bhubaneswar (India), December 14 – December 18 (2020)

July 28, 2021
Kolkata

Jaydeep Datta

DEDICATED TO

My Family

ACKNOWLEDGEMENTS

Throughout my doctoral study, many people have contributed and supported me, directly or indirectly. I would like to use this space to express my gratitude to all of them. First and foremost, I want to thank my supervisor Prof. Nayana Majumdar and co-supervisor Prof. Sankagiri Umasankar for giving me such beautiful and interesting problems to work on. Throughout my doctoral study they have supported, motivated and guided me towards successful completion of the projects. In this five year long beautiful journey members of my doctoral committee, Prof. Supratik Mukhopadhyay, Prof. Amol Dighe, Prof. Gobinda Majumder, Dr. Satyanarayana Bheesette and Prof. Satyajit Saha guided me with their experience and knowledge. I like to thank them all.

I would like to thank my father, Jitendra Narayan Datta, mother, Juin Datta and sister, Jayeeta Datta, who always supported my dream and encouraged me to go for it. In this five year long journey, many ups and downs have come along the path. They have supported me through these ups and downs. In this five year I have been stationed at many institutes all around India due to my mixed nature of work. I roamed around here and there and made many friends who supported me when I needed them. My friends from TIFR, Sabir, Subhajit, Uttiya, Anustup, Sounak, Argha, Soumen and Anupam always cheered me up when I felt low. Late night discussions with them on every possible topics enriched and energized me for the next day. My friends at SINP, Sridhar, Prashant, Arpita, Dr. Bankim da, Sayan and Shubham helped me throughout my Ph.D. tenure. A tea with them charged me up whenever I felt tired. Along with them, my school friend Ritabrata was always there to share experiences. I will also like to thank my juniors, Vishal,

Contents

I   Study of alternative gas mixtures of RPC for ICAL at INO   33

4   Resistive Plate Chamber   35

5   Numerical Modelling of RPC   45

List of Figures

List of Tables

List of Abbreviations

ASCII   American Standard Code for Information Interchange

ASIC   Application-Specific Integrated Circuit

CC   Charged Current

CLS   Closed Loop System

FPGA   Field Programmable Gate Array

GTLB   Global Trigger Logic Board

GWP   Global Warming Potential

HMC   Hybrid Micro Circuit

ICAL   Iron Calorimeter

IH   Inverted Hierarchy

IMB   Irvine-Michigan-Brookhaven

INO   India-based Neutrino Observatory

KAMLand   Kamioka Liquid Scintillator Anti-neutrino Detector

LVDS   Low Voltage Differential Signal

MFC   Mass Flow Controller

MINOS   Main Injector Neutrino Oscillation Search

MSW   Mikheyev-Smirnov-Wolfenstein

NC   Neutral Current

NH   Normal Hierarchy

NOνA   NuMI Off-Axis ν_e Appearance

PMNS   Pontecorvo-Maki-Nakagawa-Sakata

PMT   Photo Multiplier Tube

PREM   Preliminary Reference Earth Model

RPC   Resistive Plate Chamber

SK   Super-Kamiokande

SM   Standard Model

SNO   Sudbary Neutrino Observatory

SRB   Signal Router Board

T2K   Tokai to Kamioka

TDC   Time-to-Digital Converter

TLB   Trigger Logic Board

Introduction

Human civilization has come a long way since the discovery of fire. Our indomitable curiosity has driven us from the depth of the sea to the core of the star in search for answers to the unknowns. It has given birth to different disciplines for exploring our mother nature, of which physics is one. Knowing the past, understanding the present and predicting the future of our universe is the soul of physics. After centuries of hard work, now we are at a stage where we can dare to claim that we understand a little of our universe. We have come a long way to perceive the fundamental forces and developed a framework to describe most of the universe. This well accepted framework, namely the Standard Model (SM) [1, 2], says that our universe, no matter how diverse it seems, is built of a few elementary particles as shown in figure 1.1. Depending on their intrinsic property, called spin, these elementary particles can be divided into two classes: fermions and bosons. Quantum Field theory proposes that every particle, whether boson or fermion, should have an anti-particle. According to the SM, the vector bosons mediate the fundamental interactions. For example, the electromagnetic

1

Standard Model of Elementary Particles

	three generations of matter (fermions)			interactions / force carriers (bosons)	
	I	II	III		
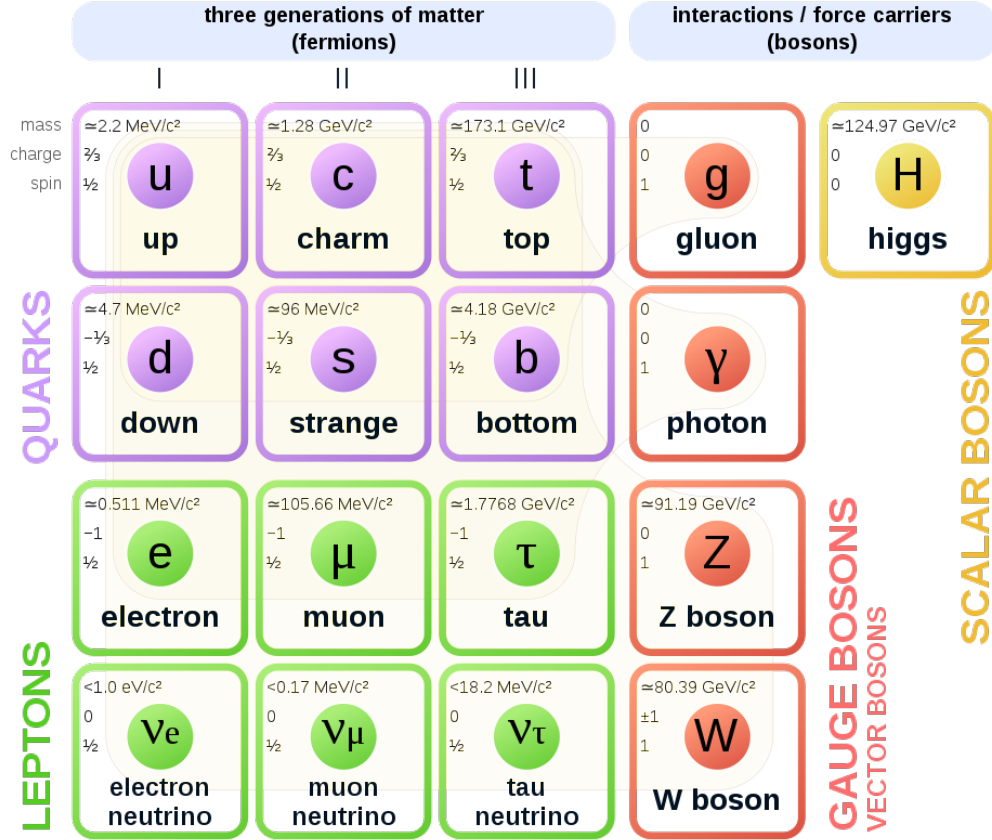
Figure 1.1: A schematic representation of Standard Model [1].

interaction is mediated by photon, the weak interactions by Z°, W^+ and W^- and the strong interactions by gluons [2]. The SM also contains a spin zero boson called the Higgs boson, which is responsible for the mass of all the particles [3]. There are twelve elementary fermions in the Standard model, along with their anti-particles. They can be further divided into two sectors, known as quarks and leptons. It has been experimentally established that each of these sectors consists of three families [4, 5, 6, 7, 8]. For example, the electron, muon and tau families belong to the leptonic sector. Moreover, each of these families consists

of an electrically charged and a neutral member, and the family name is derived following the charged member. The electrically neutral leptons are known as neutrinos, who naturally don't take part in electromagnetic interactions. However, it has been also established that neutrinos take part in weak interactions but remain unresponsive to strong interactions [9]. They are mass-less particles as described by the SM. Following their family name, commonly known as flavor, the neutrinos are labeled as electron neutrino (ν_e), muon neutrino (ν_μ) and tau neutrino (ν_τ).

In the year 1930, Wolfgang Pauli proposed the existence of neutrino, an electrically neutral, mass-less particle to explain the beta-decay spectrum. Initially named as "neutron", it was later called "neutrino" following Enrico Fermi's proposal to distinguish it from the heavier electrically neutral nucleon, known as neutron, discovered by James Chadwick in the year 1932. In the year 1956, Clyde Cowan, Frederick Reines, F. B. Harrison, H. W. Kruse, and A. D. McGuire announced the detection of neutrino [10]. In 1962, discovery of ν_μ proved the existence of more than one species of neutrinos [11]. Later, the Large Electron Positron (LEP) collider measured the invisible decay width of Z° boson and established that there are three light neutrino species [4, 5, 6, 7, 8]. The third species, ν_τ was later discovered in the year 2000 by the DONUT collaboration [12] at Fermilab. Since then, neutrinos have always remained at the forefront of physics and played the role of a probe to the yet undiscovered side of our Universe.

Since neutrinos react only weakly, they form the best probe available to understand stars and other stellar objects. A model was built which predicted that a huge number of neutrinos should be generated as a consequence of the

nuclear reactions going on inside the Sun [13, 14]. To establish the solar model, experiments were designed to measure the neutrino flux emanating from the Sun. The famous Homestake experiment measured the solar neutrino flux and observed only a third of the predicted flux [15]. To explain this discrepancy, different solutions were put forward. Some of these solutions doubted the solar model, some suspected the nuclear reaction models, and others raised the question of non-standard neutrino properties. The latter included propositions of vacuum oscillation of neutrinos [16], precision of neutrino spin in the magnetic field of the Sun [17, 18], neutrino decay [19, 20] and even neutrino oscillation assuming the oscillation length comparable to the Sun to Earth distance [21]. But all these solutions have one important requirement, that the neutrinos must have mass. Later, different experiments, such as Kamiokande II, SAGE, Gallex, SNO, Super-Kamiokande (SK) ruled out most of the solutions [22]. With the production of the first SK data, the Mikheyev-Smirnov-Wolfenstein (MSW) solution [23, 24, 25, 26] of the solar neutrino problem received a wide acceptance [27]. Later in the year 2001, the Sudbury Neutrino Observatory (SNO) established the neutrino oscillation phenomena as well as the MSW solution, which proved the massive nature of neutrinos implicitly [28, 29].

Experimentally, it has been established that only left-handed neutrinos and right-handed anti-neutrinos exist [30]. To explain neutrino mass, two theories were put forward. One of them proposes that neutrinos are Dirac particle, which means that the neutrinos and anti-neutrinos are separate particles and the right-handed neutrinos and left-handed anti-neutrinos don't interact through SM gauge bosons. The other proposition says that they are Majorana particles, implying neutrinos and anti-neutrinos are the same particles. In case of massive

neutrinos, it was proposed that the flavor eigenstates of neutrinos need not be mass eigenstates, but instead are a superposition of the mass eigenstates [16, 31, 32]. Maki, Nakagawa and Sakata formulated the mixing between flavor states and proposed a unitary matrix known as PMNS matrix. Like every unitary matrix, PMNS matrix can be parameterized using nine parameters: three mixing angles and six phases. Out of the six phases, three can be absorbed in the neutrino flavor eigenstates irrespective of the Dirac and Majorana nature of neutrinos. If neutrinos are Dirac particles, two more phases can be absorbed in neutrino mass eigenstates and the sixth one is responsible for CP violation, which is denoted as δ_{CP}. The three mixing angles are denoted as θ_{12}, θ_{23} and θ_{13}. In the course of propagation of a flavor eigenstate, different mass eigenstates pick up different phases due to time evolution. This time evolution phase is dependent on the mass square difference of the mass eigenstates, which can be expressed as $\Delta_{ij} = m_i^2 - m_j^2$, where i, $j = 1, 2, 3$, and $i > j$. This phase is responsible for the neutrino oscillation.

Following the PMNS paradigm, the oscillation probabilities depend on three mixing angles, two mass square differences and one CP violating phase. The mixing angle θ_{12} and the mass square difference Δ_{21} were determined from solar neutrino [33, 34, 35, 36, 37, 38] and KamLAND reactor neutrino data [39, 40, 41]. The CHOOZ reactor neutrino experiment pinned down the value of θ_{13} [42, 43]. The values of Δ_{31} and θ_{23} were measured by long-baseline experiments, like T2K [44], MINOS [45] and atmospheric neutrino experiments, SK [46], IceCube-DeepCore [47]. The CP violating phase was obtained from two separate long-baseline experiments, T2K and NOνA though they disagree about its value. Currently, the value of Δ_{31} is known, but its sign is yet to

be determined. Therefore, it is not yet established whether the mass m_3 is the largest or the smallest. The present time will continue to see many experimental endeavors to explore the unknown sign of, Δ_{31} which is commonly known as the mass hierarchy problem. The case of positive Δ_{31} is labelled normal hierarchy (NH) and that of negative Δ_{31} inverted hierarchy (IH).

Atmospheric neutrinos are the most abundant natural source of neutrinos, with energy varying from hundreds of MeV to a few Tev. They are generated in decay of the short-lived particles, like $\pi^{\pm,\,0}$ and $K^{\pm,\,0}$, created in interactions between cosmic particles and gas molecules present in Earth's atmosphere. Due to their short life span, the pions and kaons decay into muons and muon neutrinos, conserving the electrical and leptonic charge of the reaction. The muons created in these processes can also decay and produce electrons along with electron neutrinos. All these processes can be expressed as follows

$$p + air \rightarrow \pi^{\pm}, \pi^{\circ}, K^{\pm}$$

$$\pi^{+}, K^{+} \rightarrow \mu^{+} + \bar{\nu}_{\mu}, \ \ \pi^{-}, K^{-} \rightarrow \mu^{-} + \nu_{\mu}$$

$$\mu^{+} \rightarrow e^{+} + \nu_{e} + \bar{\nu}_{\mu}, \ \ \mu^{-} \rightarrow e^{-} + \bar{\nu}_{e} + \nu_{\mu}$$

Neutrino flux up to energy of few GeV has negligible contribution of ν_{τ} flux due to lack of energy to produce heavy particles such as τ. Following the neutrino generation processes, it is evident that the total ν_{μ} and $\bar{\nu}_{\mu}$ flux is nearly double of the total ν_{e} and $\bar{\nu}_{e}$ flux [48]. But this ratio is not constant and heavily depends upon the neutrino energy E_{ν} as shown in figure 1.2 [48]. The robust calculations of neutrino flux by different groups predicted up-down symmetry in the flux at high energy in absence of neutrino oscillation. But initial data from IMB [53,
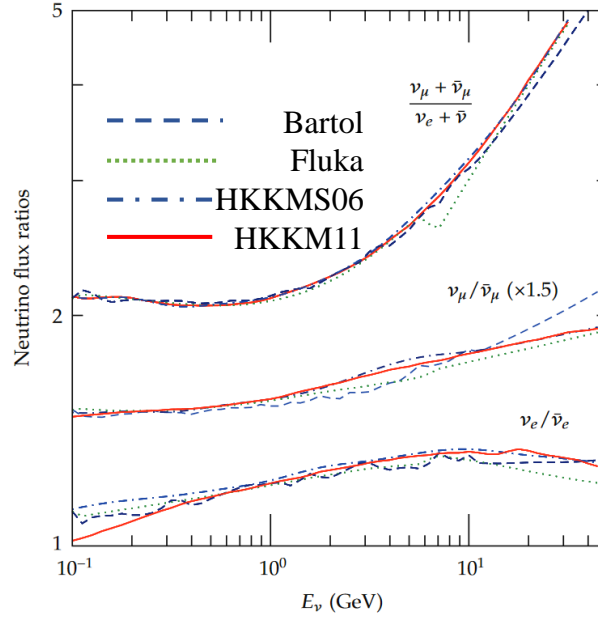
Figure 1.2: Neutrino flux ratio as function of E_ν calculated by Bartol group [49], Fluka Group [50], HKKMS06 [51] and HKKM11 [52] for the Kamioka site, Japan [48].

54] and Kamiokande [55, 56] did not observe such symmetry in atmospheric muon neutrino fluxes. Later, SK [57] measured the zenith angle dependence of atmospheric muon and electron neutrinos and established atmospheric neutrino oscillations. These detectors are placed underground and observe neutrinos coming from all the sides. The neutrinos which are coming from top and going downwards reaches to the detector after traversing the atmospheric height which maximally 20 km. But the neutrinos which are coming from bottom and going upward with respect to the detector traverse the whole Earth and a path of about 12756 km. So, these detectors observed neutrinos which traverse path lengths (L) of few km to thousands of km. This huge L/E_ν spectrum available for atmospheric neutrinos makes them an excellent probe to explore neutrino oscillation. The result from SK [57] established that the atmospheric muon neutrino oscillation is

governed by the parameters Δ_{31} and θ_{23}. The Earth-matter potential modifies the oscillation probabilities of the neutrino and its anti-particle in completely opposite way, depending on the sign of the parameter Δ_{31}. Therefore, the measurement of neutrino and anti-neutrino fluxes traversing through the Earth can give an important lead towards the determination of the sign of Δ_{31}. Moreover, this huge L/E_ν spectrum available for atmospheric neutrinos makes the observed data insensitive to the yet to be measured CP violating phase, which can mimic the Earth matter effect in neutrino oscillation [58]. So, exploring the Earth matter effect on atmospheric neutrino flux can solve the neutrino mass hierarchy problem, which motivated the idea of ICAL at INO.

India-based Neutrino Observatory (INO) [59] is an underground facility proposed to be constructed for augmenting the research on neutrino physics in India. The facility will be built under the West Bodi Hills, situated at Theni district in the state of Tamilnadu. Iron Calorimeter (ICAL) is one of the experiments that will be housed in this upcoming facility with an objective of studying the atmospheric neutrinos, which are the decay product of the particles created in reactions between cosmic particles and atmospheric gas molecules. The atmospheric neutrino energy spectrum spans from hundreds of MeV to a few TeV with the flux peaking at around an order of 1 GeV. After the peak, the neutrino flux falls down following $E_\nu^{-2.7}$, where E_ν is the neutrino energy. ICAL is a calorimeter with tracking capabilities that has been designed to explore the Earth-matter effect on neutrino oscillation by studying the energy and zenith angle dependent flux of the atmospheric muon neutrinos (ν_μ) and muon anti-neutrinos ($\bar{\nu}_\mu$). This study will help in the determination of the sign of the mass squared difference, Δ_{31} ($= m_3^2 - m_1^2$) which is an important observable among several others of this

experiment. The Earth-matter affects the oscillation probabilities of $\nu_\mu/\bar{\nu}_\mu$ in opposite way depending upon the sign of the parameter Δ_{31}. Thus, the measurement of their fluxes has been considered as an important key requirement in the design and operation of ICAL. Eventually, the ICAL has been conceived as a tracking calorimeter with layers of iron slabs as the target material and Resistive Plate Chamber (RPC), interleaved with the iron slabs as the active component for tracking the charged leptons created in the charged current (CC) interactions between the neutrinos and iron nuclei. The charged leptons of opposite electrical charges produced by the CC interaction of ν_μ and $\bar{\nu}_\mu$ will be distinguished by application of a magnetic field across the ICAL. It will not only facilitate observing the Earth-matter effect on neutrino and anti-neutrino separately, but also determination of their energy from the curvature of the track of the charged leptons. The details of the ICAL detector will be discussed in chapter 2 and the simulation methods used to carry out its performance will be described in chapter 3.

The present doctoral work focuses on improvement of several aspects related to the future operation and performance of the ICAL experiment. The topics can be briefly mentioned as follows.

- **Exploration for alternative gas mixtures of the RPCs:-** The RPCs of the ICAL foresee a long-term operation in order to accumulate substantial statistics to achieve the experimental objectives. Alongside, the detectors should perform with spatial resolution of about 1 cm for reliable track reconstruction and time resolution of 1 ns to precisely determine the direction of the neutrinos (upward or downward). The RPC when operated in

avalanche mode with a gas mixture composed of 1,1,1,2-Tetrafluoroethane (R134a) (95.2%), isobutane (i-C_4H_{10}) (4.5%) and sulfur hexafluoride (SF_6) (0.3%) has been found to fulfill the experimental performance requirement. However, the high Global Warming Potential (GWP) of the R134a and the SF_6, which are 1300 and 23900, respectively, along with that of i-C_4H_{10} being 3 makes the effective GWP of the said gas mixture little more than 1300. It is well beyond the permissible limit of 150, set by the Kyoto protocol [60], adopted in 1997 by the United Nations Framework Convention on Climate Change (UNFCCC) in order to limit and reduce greenhouse gas emissions. It certainly calls for an exploration of alternative gas mixtures with sufficiently low GWP for operating the RPCs without compromising the objectives of the ICAL experiment. The first part of the doctoral thesis will discuss how the issue of identifying an alternative eco-friendly gas mixture has been addressed with a numerical model developed for emulating the device dynamics of RPC configured for the ICAL. In this context, the details of the design and working of RPC will be introduced in chapter 4. In chapter 5 the numerical model framed on the basis of hydrodynamic approach to reproduce the RPC performance will be described. Its comparison with available experimental data will also be reported to demonstrate its efficacy. The performance of the model has been verified in case of the RPCs of ICAL by comparing its results to the experimental measurements done with an RPC prototype. The procedure of the prototype fabrication and its test will be furnished in chapter 6. Finally, in chapter 7, an eco-friendly gas mixture proposed in this doctoral work for the avalanche mode operation of the RPC in the ICAL will be evaluated for its credibility using

the validated numerical model.

- **Discrimination of matter effect from vacuum oscillation in atmospheric neutrino oscillation:-** Neutrino oscillations governed by Δ_{31} and $\sin^2\theta_{23}$ are well established by several long baseline and atmospheric neutrino experiments which look at $\nu_\mu/\bar{\nu}_\mu$ disappearance data. In all these experiments, the neutrinos traverse through the Earth-matter. Though the presence of matter in the path of the neutrino modifies the oscillation probability, the data of these experiments, when fitted with the vacuum oscillation hypothesis, returned a good fit. Till now, only the analysis of the SK experimental data was able to discriminate the matter oscillation hypothesis from vacuum oscillation, with only 1.6 σ significance. The $\nu_e/\bar{\nu}_e$ appearance data obtained from long baseline experiments can discriminate the vacuum and matter oscillation hypotheses, but that signal can be mimicked by CP violation. This made the effect of CP violation and matter oscillation hypothesis entangled. To disentangle this degeneracy, different experiments should establish the matter oscillation hypothesis first. The next part of the doctoral thesis has studied the reach of the ICAL in this direction. Chapter 8 will describe the matter and vacuum oscillation hypotheses, followed by the discussion on the work and the results presented in chapter 9.

- **Determination of neutrino oscillation parameters using track and hit information from GEANT4:-** In the analysis methods developed earlier [61, 62] to determine $|\Delta_{31}|$ and $\sin^2\theta_{23}$ considered detector response with smearing instead of using full-fledged GEANT4 reconstruction. A re-

cent work by Rebin et al. [63] used muon information reconstructed by GEANT4 to determine these parameters and also the effect of fluctuation in the data, which have made the analysis method more realistic. In this work, hadron information has been incorporated in addition, which has been found to improve the precision. Chapter 10 will present the details of this work and the relevant results.

The doctoral thesis will end with Chapter 11 which will contain the final remarks about these studies carried out for the ICAL experiment and discuss the future scopes arising out of these endeavors.

Iron Calorimeter Detector

INO is an underground facility that would be built to house different experiments, which will require substantial background suppression. Some notable as experiments would be to study neutrino-less double beta decay, dark matter etc. The natural stone coverage of Bodi West Hills depicted in figure 2.1(a) from all sides would reduce the cosmic ray flux below 10^3 m^{-2}sr^{-1}yr^{-1}, shown in figure 2.1(b) and thus improve the sensitivity of the measurements [59].

ICAL would be a major experimental setup at INO which will primarily be dedicated for determination of neutrino mass hierarchy along with investigations related to other important aspects of neutrino oscillation phenomenon. The key factors that have governed the concept of the ICAL detector are the following.

1. A large target mass is required to achieve significant statistics of neutrino events within a reasonable time period for observation of neutrino oscillation.

2. The energy E_ν and the path-length L need to be accurately measured to detect the oscillation pattern in L/E_ν spectrum, which necessitates good

<center>((a))   ((b))</center>
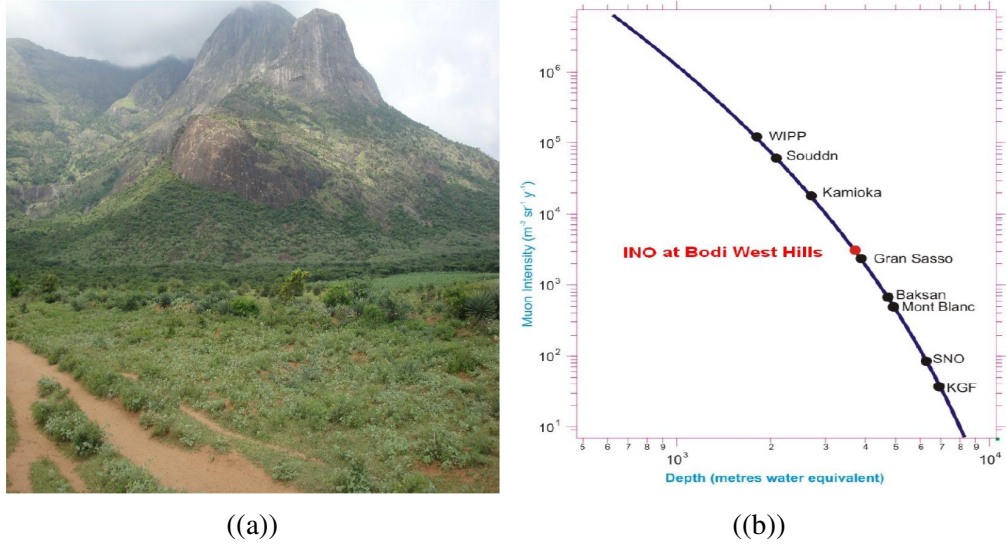
Figure 2.1: (a) INO site at Bodi West Hills [59], (b) Cosmic ray flux as function of water equivalent depth [59].

spatial and timing resolutions.

3. The charged muons should be identified to distinguish between ν_μ and $\bar{\nu}_\mu$ events.

4. The technical capabilities, availability of raw materials, ease of large scale construction should be considered important.

2.1   Iron Calorimeter

The ICAL has been designed in a modular fashion with total cross-section of 48 m $\times$ 16 m. Each of the three modules will have a height of 14.5 m and a cross-sectional area of 16 m $\times$ 16 m. It will consist of 151 with horizontal stacks of iron slabs of 5.6 cm thickness which will act as target material for the atmospheric neutrinos. The plates will be made from commercially available

low-carbon steel ASE1010 or CE10 and interspersed with 4 cm gaps for holding

the RPCs as shown in figure 2.2. RPCs made with float glass will be used for
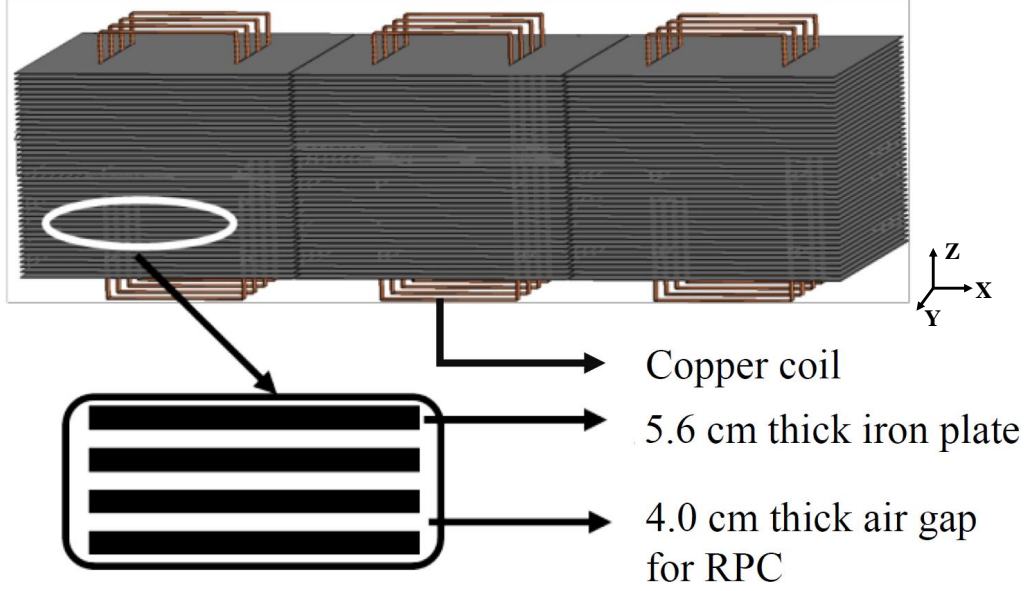
Figure 2.2: Schematic diagram of ICAL [59].

recording the position and timing information of the charged μ^-/μ^+ produced

inside the ICAL due to interaction of $\nu_\mu/\bar{\nu}_\mu$ with the iron nuclei during their flight

across the ICAL. Each RPC will have a dimension of 2 m x 2 m and about 29000

RPCs will be needed to populate the ICAL. A high magnetic field (1.3 T) will

be applied across the ICAL setup for bending the charged muons. Mechanical

support to this huge structure will be provided by placing iron spacers with a

periodicity of 2 m in both X and Y-directions in each of the 151 layers. The

mechanical specifications of the ICAL have been tabulated in table 2.1.

The RPCs will be made from 3 mm thick glass float plates of, separated by

a gas gap of 2 mm. The signals from each RPC will be acquired using two

pickup panels made with copper strips of width 2.8 cm pasted on a honeycomb

structure of G-10 material. A brief detail about the design specifications of

Number of Modules	3
Dimension of each Module	16 m × 16 m × 14.5 m
Dimension of total ICAL detector	48 m × 16 m × 14.5 m
Number of layers per Module	151
Thickness of each Iron plate	5.6 cm
Space between two Iron plates	4.0 cm
Magnetic Field	~1.3 T

Table 2.1: Mechanical specifications of ICAL detector [59].

the RPC can be found in the following table 2.2. Its structure and working

RPC dimensions	195 cm × 184 cm × 2.4 cm
Strip width	2.8 cm
Number of RPCs per layer	192
Total number of RPCs	28800
Total number of read-out channels	3.7×10^6

Table 2.2: Specification of RPCs for ICAL [59].

principle will be discussed in chapter 4. Two pickup panels are placed on either sides of the RPC arranged in orthogonal manner to provide with the X and Y-coordinates of the position information. The Z-coordinate information will be available from the position of the respective layer. Charge identification of the particle is an important requirement for ICAL. As a downward going positively charged particle and an upward going negatively charged particle will bend in the same direction under the action of the applied magnetic field, it is imperative to distinguish between them efficiently to identify their polarity. It can be accomplished with the time-of-flight measurement of the particles, which requires a good time resolution of the RPCs.

As mentioned earlier the physics goals of ICAL requires about 1 cm spatial resolution and about 1 ns time resolution which can be achieved if the

RPCs are operated in avalanche mode [59] with a mixture of R134a(95.2%):i-C_4H_{10}(4.5%):SF_6(0.3%). The ICAL will require a volume of about 216 m^3 of this gas mixture at any instant of time owing to the large number of RPCs present in the setup. Optimizing among detector performance, cost and environmental issues, the whole gas volume will be replaced once in a day. The whole ICAL will be divided into several sectors, each of which will be flushed using a closed loop gas mixing unit [64] also known as closed loop system (CLS). A schematic diagram of the same has been shown in figure 2.3. The gas mixing units will be
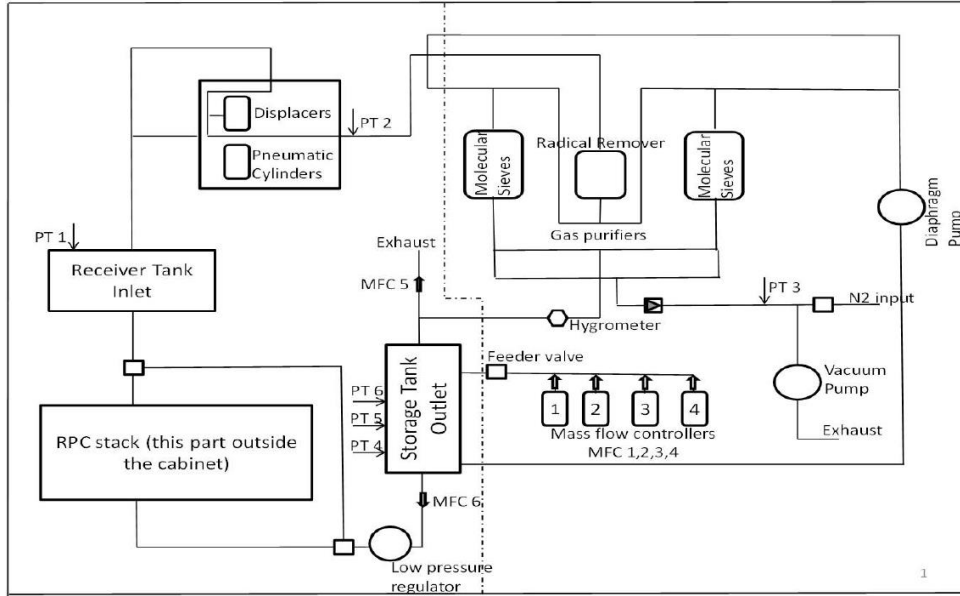
Figure 2.3: Schematic diagram of the closed loop gas mixing unit to be used at ICAL [64].

used to mix the gas components following their volumetric proportion regulated by mass flow controllers (MFCs) and flow it through a group of 12 RPCs and maintains a gas pressure inside the RPCs slightly higher than the atmospheric pressure. The goal of a CLS is to reduce the wastage of the gas mixture and recycle it for future use. During avalanche and streamer discharge inside RPC,

many radicals are created, which can deteriorate the detector health if they are not removed from the system. So, using a pneumatically controlled positive displacement pump, the used gas mixture stored in the receiver tank at RPC outlet, is sucked and sent to the radical removers. There, other than the radicals, excess water vapor is also removed. This process is done maintaining a pressure between 1015 mbar and 1018 mbar in the receiver tank. Less pressure than 1015 mbar will allow to drop the pressure inside the RPC also, which will let atmospheric gas to enter the detector and contaminate it. More than 1018 mbar may damage the detector health due to high pressure. Once the radicals are removed, the purified gas mixture is sent to the storage tank, from which the gas is resupplied to the RPCs. The pressure in the storage tank is maintained at 1650 mbar, and it is kept isolated from the RPCs by an MFC so that the high pressure is not realized by the RPCs. The drop in RPC pressure will open the low-pressure regulator and the gas mixture will be delivered to the RPC stack. Once the pressure in the storage tank falls below 1350 mbar, the MFCs connected to different gas cylinders starts working and let pure gases to enter the storage tank, maintaining the desired volumetric proportion of the component gases. The filling up continues till the pressure reaches 1650 mbar, more than that opens the exhaust and excess gas is released.

2.2   Magnet of ICAL

Depending on the mass hierarchy of the neutrinos, the resonance effect due to Earth-matter occurs either in neutrinos or in anti-neutrinos. In case of Normal Hierarchy (NH), the resonance is present in neutrinos and for Inverted Hierarchy

(IH), it is observed in case of anti-neutrinos. So, measuring the neutrino and anti-neutrino interaction rates individually is the most important goal of the ICAL detector. Here the magnetic field plays a crucial role as it makes the track of the charged muons to bend differently depending on their polarity. Also, the radius of curvature of the track depends on the momentum of the charged muon. As the momentum information of the charged muons is important for the determination of the mass hierarchy, uniformity of the magnetic field is essential to ensure precision in the measurement. Apart from this, several technical issues, like ease of handling and optimization between the magnetic field and power consumption, have governed the design criteria of the electromagnets used in ICAL.

A toroidal design of the electromagnet made of copper coils has been opted for the ICAL. A small cross-section of 1 cm × 1 cm with small width of 20 cm of the coils has ensured the required magnetic field with minimum loss of active volume of the detector. The coils will pass through two rectangular slots in the stack of the iron plates. To produce a magnetic field of 1.3 T, a copper coil of 40000 amp-turns is deployed in each module of the detector. Figure 2.4(a) shows the schematic diagram of the electromagnet of a single module of the ICAL detector. The magnetic field distribution in each layer of the module has been depicted in figure 2.4(b). It has been found that. The magnetic field varies by less than 0.15% over a depth of ± 5 m in Z-direction from the center of the module. Though the variation of magnetic field in X-direction is less than 0.25%, but they fall rapidly outside the coil set (± 4 m) in Y-direction.
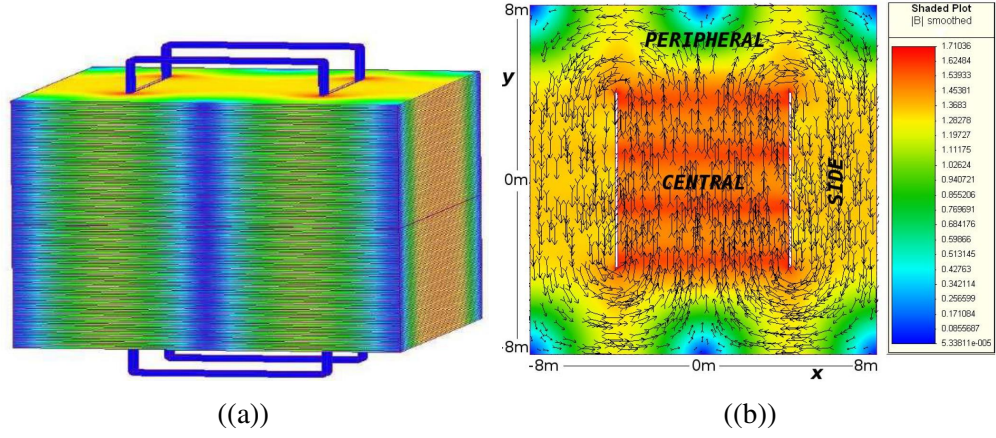
Figure 2.4: (a) Schematic diagram of copper coil in each module of ICAL [65]. (b) Magnetic field map in the central plate of the central module (Z = 0) the magnitude (in T) [59].

Gain of each channel	~ 4 mV/μA
I/p dynamic range	1 - 80 μA
I/p impedance (up to 500 MHz)	< 45 Ω
Propagation delay	< 1 ns
Power consumption per channels	~ 45 mW
LVDS output current	$\pm$ 4 mA

Table 2.3: Specification of ANUSPARSH ASIC [66].

2.3   Readout system

It has been already mentioned in section 2.1 that the basic RPC detector element for ICAL will deliver position information of the passage of a charged muon from the signal induced on the appropriate pickup strips laid along orthogonal directions. RPCs operated in avalanche mode produce very small signals, which needs to be amplified for better discrimination between signal and background electrical noise. For this purpose, a Front-End (FE) ASIC named ANUSPARSH has been developed, which serves the purpose of amplification and discrimination of the RPC signal. Specifications of this chip is given in table 2.3 An FE board
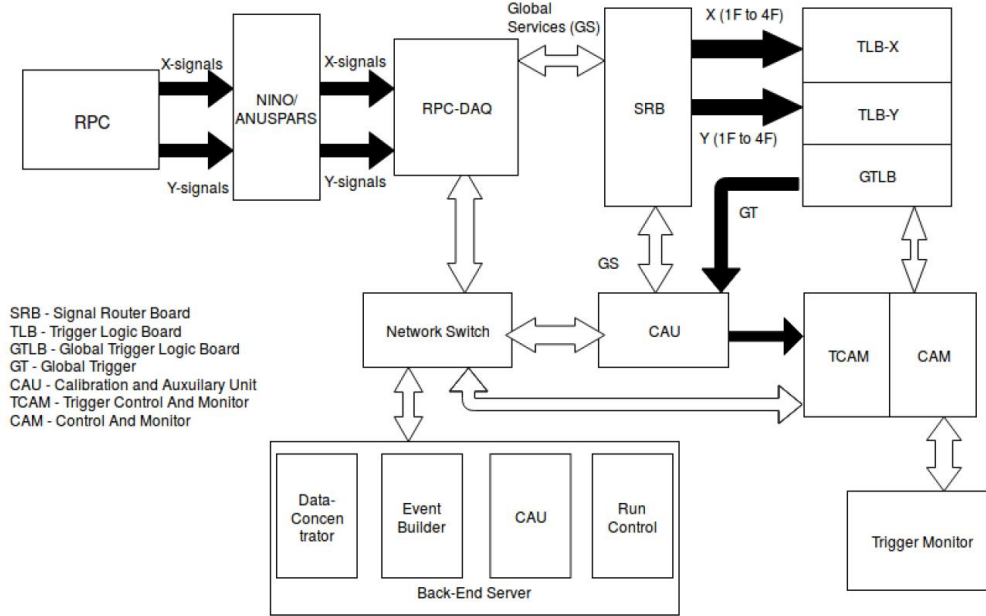
Figure 2.5: Schematic diagram of data flow and storage of ICAL [67].

has been designed to acquire the RPC signal which will have two 4-channel trans-impedance, voltage sensitive pre-amplifier ASIC chips [66] and one 8-channel discriminator chip. The FE boards for the anode side have been designed to receive only negative polarity signal, while that on the cathode side for the positive one. On each side, there would be 64 pickup strips, for which eight FE boards would be required. Following the discrimination, the output will be a Low Voltage Differential Signal (LVDS) which will be sent to a digital backend board named RPCDAQ. It will produce four OR signals, namely 1-fold, 2-fold, 3-fold and 4-fold, using the discriminated RPC signals and send them to trigger system module via Signal Router Board (SRB). The trigger system module consists of two Trigger Logic Boards (TLBs), one for each of the X and Y-side. Each of these TLBs creates a coincidence trigger using a 1-fold signal from four pre-fixed layers of the corresponding side. A global trigger will be generated in the Global

Trigger Logic Board (GTLB) by carrying out OR operation on these two trigger signals from X and Y-side TLBs. It will initiate recording of the data in the RPCDAQ board once the trigger is received. Subsequently, it will be passed on to data concentrator and Event Builder via Network Switch. The output of this step will be stored in a computer for further analysis. The schematic of the readout and data collection is shown in the figure 2.5. Details of these processes can be found in [68, 69, 70].

It can be followed from the discussions made in this chapter that the ICAL has been designed following the requirement to make it sensitive to the energy, direction and sign of the electric charge of the muons that are produced in the CC interaction of the detector material with the atmospheric neutrinos. In the next chapter, the simulated performance of the ICAL will be discussed, which is important to judge the scope of the detector system in achieving the desired objectives of neutrino oscillation experiment.

Simulation Framework of ICAL

The ICAL experiment will explore the Earth matter effect on the neutrino oscillation by studying the dependence of multi GeV atmospheric $\nu/\bar{\nu}$ fluxes on zenith angle and energy [59]. The unique capability of the detector to discriminate neutrinos from anti-neutrinos makes it a contender of solving the long-standing neutrino mass hierarchy problem. The final state particles created in neutrino-nuclei interactions in the detector will be studied to extract information about the parent neutrinos. So, precise measurement of energy and direction of the final state charged particles will be crucial for the experiment. This demands a careful and detailed calibration of the detector beforehand, which can be useful in predicting and interpreting the actual experimental data. In this chapter, a brief discussion will be made about the ICAL simulation framework which is used to carry out a realistic numerical experiment incorporating ICAL geometry and RPC properties to find out the response of ICAL to the atmospheric $\nu/\bar{\nu}$ fluxes. It provides an assessment of the potential of ICAL to measure the dependence of these on zenith angle and energy. A schematic flow-chart of the simulation

framework has been shown in figure 3.1 where all the steps taken to accomplish the simulation in general have been broadly classified into several blocks. In the following sections, each of the blocks will be discussed in reference to the present doctoral work.

3.1   Event Generation

The simulation framework starts with an event generator which creates neutrino events using atmospheric neutrino flux and propagates the neutrinos to let them interact with the detector. The neutrino cross-sections are stored as internal libraries in the generator, and the events are generated for a given number or an exposure time. There are many neutrino generators available, like ANIS [71], FLUKA routines [50], GiBBU [72, 73], GENIE [74], NEUT [75], NUANCE [76], NEGN [77], etc. which are basically Monte-Carlo programs. In this doctoral work, NUANCE has been used as the event generator, which is a FORTRAN based program. It was originally developed by Dave Casper to generate events for the simulation of SK experiment. A simple model of ICAL geometry and the neutrino flux observed at Kamioka site have been subjected to simulate the interaction of the neutrinos with the ICAL. NUANCE has returned information about the parent neutrinos along with their interaction vertex and the momentum and identity of the final products in ASCII format. The ASCII file has been imported to C++ based GEANT4 package [78] for carrying out the next steps of event simulation, digitization and reconstruction. Several interaction mechanisms, such as Quasi Elastic (QE), Resonance (RES), Deep Inelastic Scattering (DIS), coherent nuclear processes on nuclei, neutrino-electron elastic scattering

Event Generation

- Uses detector geometry, atmospheric neutrino flux and neutrino interaction cross-sections to generate events.
- Returns the interaction vertex information, energy, momentum and identity of final state particles.

Event Simulation

- Uses the output information of event generator.
- Propagates the final state particles through the detector geometry and produces the X, Y, Z-coordinates and time stamp of the particle-hits.

Event Digitization

- Uses hit pattern of each particle and incorporates detector properties.
- Returns strip positions corresponding to the particle-hits

Event Reconstruction

- Sifts through the digitized hits and reconstructs the track of each particle.
- Reconstructs energy, electrical charge and direction of the particles and stores with time and event stamps.

Analysis

- Uses the stored output of reconstructed events.
- Analyses stored data using different user-specific methods to estimate ICAL's reach for different phenomena.

Figure 3.1: Schematic of the ICAL simulation framework.

and inverse muon decay [76] are considered. The event generator can also generate an oscillated event spectrum, for which it assumes Earth as a system of 25 concentric shells of constant density. To reduce the computational expense and complexity in calculation, this option has not been exercised in the present simulation. In the following sections, the subsequent steps of the simulation work carried out using the GEANT4 package will be discussed.

3.2   Event Simulation and Digitization

At this stage, the event simulation starts with shooting the final state particles of neutrino interaction with their momentum and energy as provided by the event generator. In this work, the particles produced at different interaction vertices with given momentum and energy as provided by NUANCE have been propagated and the GEANT4 has calculated energy deposition by them in the ICAL setup. To accomplish this, a machine-readable file containing the ICAL detector geometry, interaction cross-sections of different particles and various physics models have been considered. The geometry file of the ICAL contains the relevant details, such as thickness and position of iron slabs, position of copper coils for the magnet, design parameters of the RPCs including their copper pickup strips and gas mixture, and the support structure of each module of the ICAL. The magnetic field distribution in each module has been also incorporated in the detailed information of the ICAL. All the particles have been tracked till they have stopped in the ICAL or left the detector. A minimum cutoff energy has been set to determine the location of their stopping, while the particles that have escaped the detector have been tracked till the boundary. The RPC has been considered

to register a hit if any charged particle deposits more than 30 eV in the detector gas gap. A detector efficiency of 95% also has been incorporated to mimic the realistic detector performance. The corresponding X, Y and Z-coordinates of each hit in the RPC with the time and event stamp have been stored and digitized subsequently.

In the digitization stage, the RPC properties, such as spatial resolution, cross talk between the pickup strips, multiplicity of the detector and its time resolution are required to translate the simulated hit to 3D position information as would be recorded by the detector system. Using these parameters from [79] the precise hit position has been converted to the position of the X and Y pickup strips which have registered the hit. For obtaining the Z-position of each hit, the vertical location of the RPC in the ICAL has been recorded.

3.3 Event Reconstruction

In the next step, the tracks of the particles have been reconstructed using the digitized hits as obtained from different layers of RPC. The event reconstruction part has been done in two steps, which are namely track finding and track fitting. These will be discussed in the following subsections.

3.3.1 Track finding

The hits, generated for all the particles of an event, are stored irrespective of any specific particle or group of particles. In order to reconstruct the track, it is necessary to identify the hits which belong to the track. For this purpose, all the adjacent X and Y hits for an event in a layer are first grouped, and this is done for
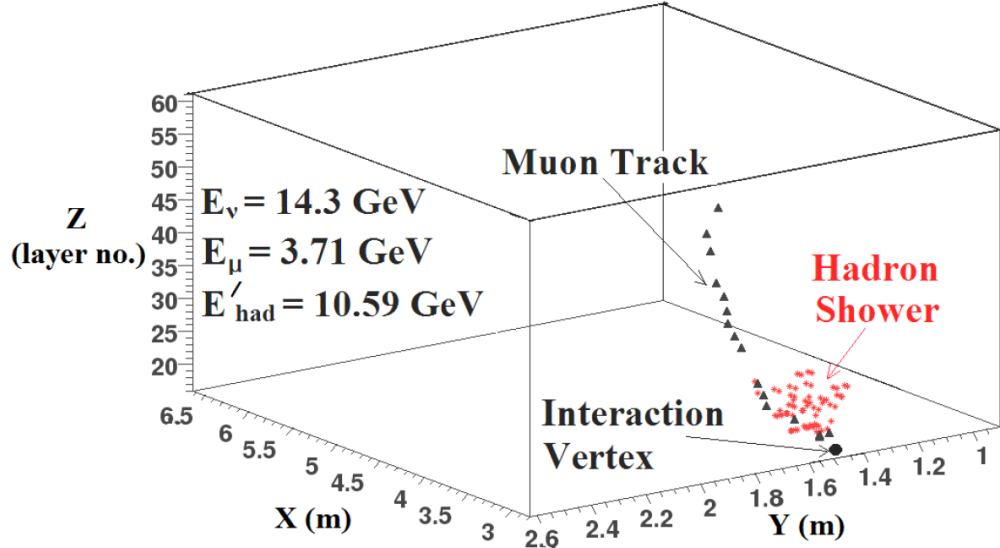
Figure 3.2: An example of simulated ν_μ CC interaction in the detector [81].

all the layers. In the next, the groups of the adjacent layers are then fitted using a curve fitting program to form tracklets which are subsequently joined to form a track. These processes are carried out in an iterative manner to form tracks [80]. To identify the direction of the movement of the particle (upward / downward), time information from each group of different layers are considered. The average time information of all the X and Y hits of each group has been considered as the time stamp of the respective group. Usually a muon track is found clean having one or two hits per layer, while a high energy electron or hadron creates a shower of hits in the detector. Different hadrons create similar kind of showers, and identifying the hadron from the shower is not possible as a result. Only the direction and number of hits for them is stored. A typical case of CC interaction in the detector has been presented in figure 3.2 where the muon track and the hadron shower produced from the interaction vertex have been marked.

3.3.2 Track fitting

Following the determination of tracklets, a track fitting algorithm based on Kalman filter is introduced for the purpose of track finding. It includes the effect of the magnetic field as the tracks of the charged particle bend under its influence. The process starts with a state vector

$$X_0 = \left(X, Y, \frac{dX}{dZ}, \frac{dY}{dZ}, \frac{q}{p}\right)$$

where X, Y and Z are the hits coordinates and $\frac{q}{p}$ is the ratio of charge and inverse momentum of the particle at a specific layer. At the beginning the track is linear and hence the track direction can be found from $\frac{dX}{dZ}$ and $\frac{dY}{dZ}$ of the first two layers. For further propagation, Kalman gain matrix is calculated. The calculation incorporates the local magnetic field and geometry of the detector and uses these to extrapolate the predicted position of the tracklet in the next layer. While predicting the state vector using Kalman algorithm in the next layer, noise due to multiple scattering [82] and energy loss of the particle as described by Bethe formula [83] are incorporated. The error propagation is implemented by calculating the propagator matrix [80]. Improved formulae for atmospheric neutrinos [84] have been used for propagation of states and errors. The extrapolated point is then compared with the actual hit point in that layer if there has been any and the error is estimated. Following its minimization, the track is extrapolated back to compare with the earlier hits and estimate the errors there, which are minimized also. Then again the state vector is propagated for finding the next hit and the same process is repeated. This iteration continues till the best fitted track is found. The condition to stop the iteration, that the value of $\frac{\chi^2}{ndf}$ will be less than 10. Subsequently, the fitted track is extrapolated back to

find the vertex and the momentum at the vertex is considered as the reconstructed momentum of that particle. The magnitude of the momentum is saved as, $\frac{q}{p}$ with its sign determined by the polarity of the charge of the particle. From the value of $\frac{dX}{dZ}$ at the vertex, the direction of the event is determined while the value is saved as zenith angle θ, and from the value of $\frac{dY}{dZ}$ the azimuth angle is calculated and stored as ϕ.

The muons that are produced in the neutrino-nucleus CC interaction in the ICAL, are minimum ionizing particles, and so deposit less energy leaving a long track in the detector. To identify a track produced by muon, a threshold of 5 hits in the track has been implemented. For other particles, if a track is reconstructed, information related to it has been also stored in an array where the longest muon like track is kept as the first entry. To find the hits due to hadron shower, an algorithm named trapezoidal algorithm [85] is used. Events with hadrons as final particles can be classified in two categories: one with a reconstructed track and the other one without any reconstructed track. In case of a reconstructed track, it is extrapolated back up to six layers and absence of real hit in the vicinity of extrapolated hits in two consecutive layers terminates the extrapolation. Around the newly found vertex a trapezoid is formed with its base of 10 cm. All the hits which are not used in track reconstruction and falls in this trapezoid are taken as hadron hits. In case of no reconstructed track, first all the RPCs having the large number of hits (> 100 strips fired) are excluded and then clusters are formed. Details of ICAL muon response can be found in [59] following which the reconstruction of the energy of the particles, its electrical charge and direction are done.

3.4   Analysis Method

With the simulated output, different physics analyses are carried out using ROOT data analysis framework [86]. For brevity the output of the ICAL simulation code is stored in .ROOT format, formatted for an object-oriented data analysis framework, namely ROOT to analyze large amount of data efficiently. The simulated data are stored in .ROOT format consisting a main section and different subsections under it denoted as tree and branch respectively. Depending on the physics topic to be studied, an analysis code is developed which uses the reconstructed information as described above.

While in propagation, the atmospheric neutrinos oscillate, which changes the flux of different neutrino flavors. The following section will describe the procedure followed to incorporate neutrino oscillation in this doctoral work.

3.4.1   Oscillation Probability Calculator

Different phenomenological studies for ICAL need the oscillated neutrino event spectrum. It can be generated using NUANCE as mentioned in section 3.1, however, it will require to follow all the procedures of figure 3.1 for each combination of the oscillation parameters to get the reconstructed event information for any analysis work which reduces the flexibility of the analysis method and need huge computational power. To circumvent it an open source oscillation probability calculator, namely nuCraft [87], developed by the IceCube collaboration, has been used in this work. It is a python based code which calculates the oscillation probability by solving the Schrödinger equation numerically in the interaction picture. The said calculator is capable of calculating oscillation probabilities for

both vacuum and Earth matter. It uses PREM model to calculate the probabilities in presence of matter, where the earth is considered as a structure of 25 concentric shells. To incorporate the effect of the path traversed in atmosphere, it assumes a depth of 20 km of atmosphere. It randomly chooses the height in atmosphere where the neutrino is created. The depth at which the detector is kept can be given as an input to the calculator. It considers fixed values of oscillation parameters, certain directions as cosine of the zenith angle and energy range for which the probabilities are to be calculated. The output of the GEANT4 simulator is saved in a .ROOT file for further analysis. The available code has been modified in the present work so that the oscillation probabilities can be calculated for each generated event, for all the combinations of the oscillation parameters that are required for the work.

The next part is dedicated to the exploration for alternative gas mixtures of the RPCs. The details of RPC structure and its working principle will be described, and a simulation framework will be developed to identify potential alternative gas mixtures of RPCs. The last part will discuss ICAL's capability to discriminate matter effect from vacuum oscillation in atmospheric neutrinos and determination of neutrino oscillation parameters using track and non-track hit information from GEANT4. The output of the ICAL simulator will be used in this part as the simulated data of ICAL.

Resistive Plate Chamber

The overall size of the ICAL and its large active detection area suggests that it should be of low cost, modular in construction with components suitable for mass production in a limited time period to make the ICAL a competitive experiment in the global scenario of neutrino research. Considering all these factors, the Resistive Plate Chamber (RPC) seems to be the most appropriate choice as the active detection element in ICAL. RPC is a member of the parallel plate gas detector family introduced by R. Santonico and Cardarelli in the year 1981 [88]. It has become a very common and useful detector because of its simple design and robust structure that facilitate production of large area coverage without much difficulty. For its good timing and spatial resolution, it is well suited for a fast tracking calorimeter like ICAL. In this chapter, the structure and working principle of the RPC will be discussed.

4.1   Construction

The first member of the parallel plate chamber family is the Spark Chamber, consisting of two metallic electrodes placed across a gas volume. However, the design is not suitable for obtaining position information of an event, as the whole electrode gets induced with the signal of every particle or radiation detected. Moreover, every time a spark occurs the voltage across the electrodes drops and takes time to reset, causing a substantial dead time of the detector. To circumvent these problems, the idea of resistive electrode is introduced. The RPC is made of two resistive plates separated by a few mm. The basic criteria of the resistive material of the electrode is that its bulk resistivity should be of the range $10^7 - 10^{12}$ $\Omega - cm$. It helps the induced charge to stay localized. The higher the resistivity, the smaller the area gets induced. On the other hand, the time constant for the induced charge to get dissipated increases with resistivity, reducing the rate capability of the detector. Typically, the electrodes are made of glass or Bakelite. The gap between the electrodes is governed by the use of the detector and maintained by using suitable spacers glued to both the plates at regular intervals. Additional spacers are used along the boundary of the gap to make it a gas tight chamber. The specific gas mixture required for operation is flown through inlets and outlets that are mounted on the side spacers. Figure 4.1 depicts a cross-sectional schematic view of an RPC where the side spacers, gas nozzles and button spacers have been marked.

Like every parallel plate gaseous detector, RPC makes use of electron avalanche in the gas medium for particle detection. For that, a suitable uniform electric field is required in the gas gap. This is achieved by applying a voltage difference
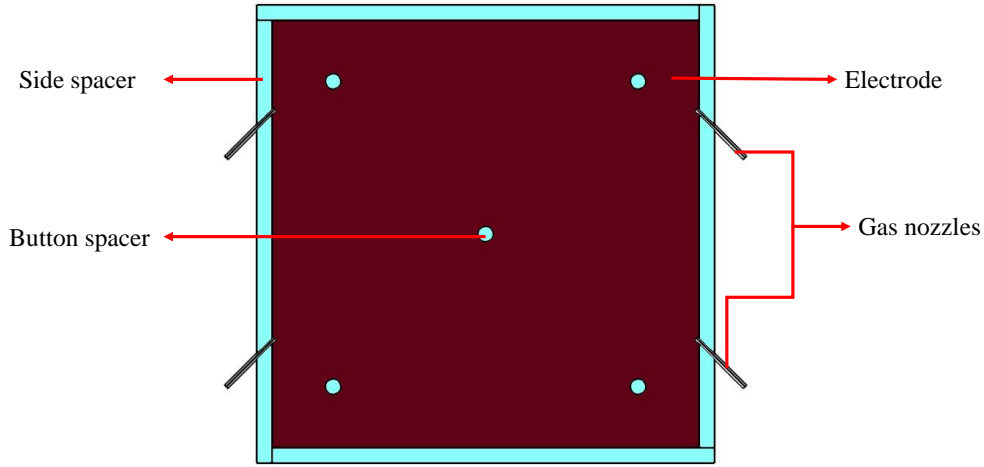
Figure 4.1: Transverse cross-sectional view of RPC.

across the resistive electrodes. Usually, one of the electrodes is supplied with a positive high voltage and the other one negative high voltage with respect to a common ground. But the practice of applying high voltage of either polarity to one electrode and keeping the other one at the ground potential is also popular. For applying the voltage to the resistive electrodes made of glass or Bakelite, a conductive coating is applied on their outer surface and the high voltage supply is connected to this conductive layer. The surface resistance of this conductive layer is important, as this decides the spread of the induced signal on the pickup strips placed outside the electrodes [89]. The higher the surface resistance, the lesser is the spread. A very high value is not desirable as this will hinder the uniform spreading of voltage.

The movement of the charges in the applied electric field induces current on the pickup strips placed outside the RPC, following Ramo's theorem [90]. From the theorem it is obvious that the current induced on the side of higher

or positive potential is of negative polarity and that is positive on the lower or negative potential side. The pickup strips placed in orthogonal manner on either sides of the gas gap facilitate to obtain the two-dimensional position information of the event. The pickup panels are made from copper strips pasted on a G-10 board with small gaps between them to reduce cross talk and achieve the desired granularity. The strip width can vary as per the requirement of the experiment. To insulate the pickup panel from the resistive coating on the electrodes, a Mylar sheet is introduced between them. Figure 4.2 shows a longitudinal cross-sectional view of RPC with all the components.
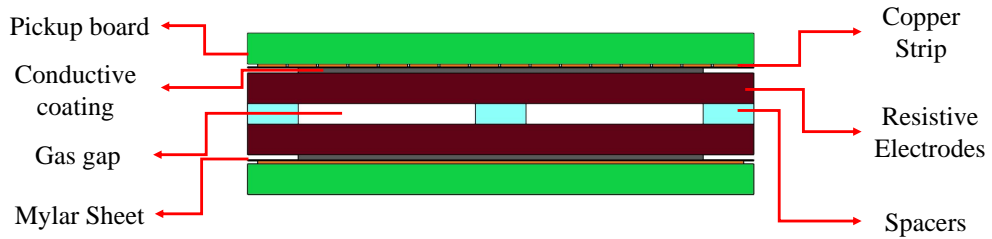
Figure 4.2: Longitudinal cross-sectional view of RPC.

4.2   Working Principle

The basic working principle of the RPC relies on the avalanche breakdown of the filling gas medium. Depending on the applied voltage, it is possible to have avalanche or streamer discharge in RPC. The requirement of a specific experiment

is the guiding factor of operating the detector in avalanche or streamer mode. The name of the mode indicates the discharge process happening for the majority of the events. To initiate the avalanche process in the detector, seed electrons are necessary, which are created due to the ionization of the gas molecules by the incident particle. The number of primary electron ion pairs produced from the ionization process depends upon several factors: the energy of the incident particle, the energy deposited by it in the gas medium, density and minimum ionization potential of the gas medium. In the absence of sufficient primary electron ion pairs, the detector will fail to perform as per the requirement, and this is one of the factor for the choice of the filling gas. In the below, the two different operational modes of RPC will be described.

4.2.1 Avalanche Mode

The seed electrons created in the primary ionization propagate along the direction of the electric field applied in the detector. The accelerated electrons go under elastic and inelastic collisions with neutral molecules, ions and other electrons. The elastic collisions between the electrons and neutral molecules or ions can cause their excitation, which gives rise to emission of photons in the process of de-excitation. These photons may have sufficient energy to initiate secondary avalanches by ionizing gas molecules or ions, which is known as photo-ionization. Two types of inelastic collisions of the primary electrons with the gaseous molecules may happen, leading to either of the absorption of the electrons or ionization of the gaseous molecules. If the applied electric field is such that the amplification of electron number is more than the number of elec-
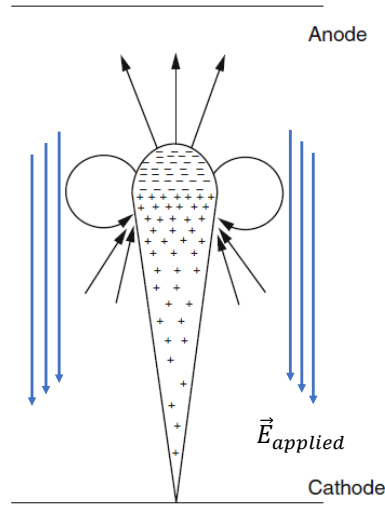
Figure 4.3: Growth of avalanche. The black-arrows depicts the field lines due to the space charge. The blue arrows show the filed lines of the applied electric field.[93]

trons getting absorbed or recombined due to inelastic collisions, a self-sustained breakdown of the gas occurs which is known as avalanche breakdown, and it was first described by Townsend [91]. One of the most fascinating phenomena related to this avalanche breakdown is the space charge effect. Riegler et al. [92] showed in their work that if the space charge effect is not considered, the small amount of induced charge cannot be explained. The space charge effect is negative feed-back to the avalanche growth. When the avalanche starts to grow, the electrons drifts faster than the ions and an additional electric field is created due to these charged species, known as space charge field. This reinforces the electric field at the tip and the back of the avalanche, but opposes the applied electric field inside the avalanche. The situation has been shown by a schematic diagram in figure 4.3. The resultant smaller electric field reduces the amplification, and for electronegative gases it may even cause loss of electrons due to absorption. In this operation mode, the induced charge amount remains less than a few pC. The

avalanche mode of operation has the following advantages and disadvantages.

- In case of small amount, charge is induced. Smaller the amount of charge less the number of induced copper strips. In case of ICAL the charge profile is not available. So, less the number of hit strips, more accurate will be the position determination and better spatial resolution.

- The typical time resolution achieved for this mode is around 1 ns.

- It takes a small amount of time for the little amount of charges to get dissipated, which makes this operation mode capable of handling high event rate.

- The small induced charge requires state of the art electronic system to process the signal. Without a dedicated pre-amplifier, it becomes difficult to identify the signal.

4.2.2 Streamer mode

This mode of operation takes place at higher electric field than the previous one. As the name suggests, in this mode the streamer discharge occurs for most of the events. When the electron avalanche starts growing under its own space charge field rather than the applied one, it is known as streamer discharge. Depending upon the growth mechanism, the streamer discharge can be classified as follows

- Positive Streamer or Cathode Directed Streamer

- Negative Streamer or Anode Directed Streamer.
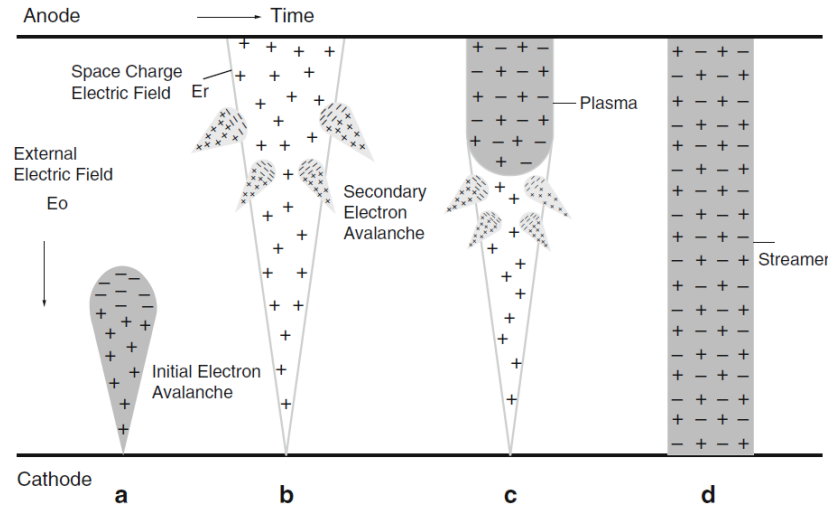
Figure 4.4: Schematic diagram of positive streamer formation [93].

4.2.2.1   Positive Streamer or Cathode Directed Streamer

Streamer discharge starts with an avalanche as shown in figure 4.4 (a) with the
electrons moving faster than the ions. The drift velocity of ions is usually 3
orders of magnitude smaller than that of the electrons. As a result, by the time
the avalanche reaches to the anode and starts losing electrons, the ions can not
reach to the cathode, which is shown in figure 4.4 (b). At this point, the space
charge field of the ions comes into play. If the number of the ions is so large
that the space charge field is equal to that of the applied one, it starts attracting
all the secondary avalanches towards it as shown in figure 4.4 (c). The electrons
of these secondary avalanches upon reaching the zone with high density of ions
recombine with some ions present there, leaving back their ions, which shifts the
high density ion zone towards the cathode. Just behind this zone, a quasi neutral
plasma of electrons and ions is created, as shown in figure 4.4 (c). The shifted
high density ion zone again attracts other secondary avalanches and in the same

way it moves closer to the cathode as shown in figure 4.4 (d). Apparently the process looks like as if the electrons are moving towards the cathodes, however, actually it is the high ion density zone is moving towards the cathode with a quasi neutral plasma following it. This kind of space charge field controlled growth is known as streamer discharge. As the movement takes place towards the cathode, it is called as cathode directed streamer. As the tip of this growth is populated with positive ions, it is named as positive streamer.

4.2.2.2 Negative Streamer or Anode Directed Streamer
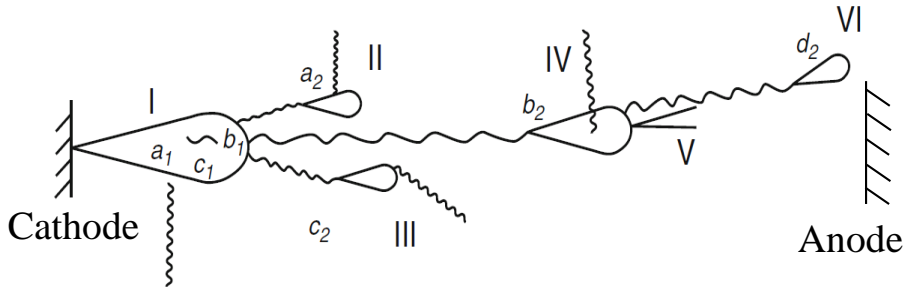
Figure 4.5: Schematic diagram of negative streamer [93].

This kind of streamer discharge requires higher electric field than that required for positive streamer to take place. Like positive streamer, it also starts with an avalanche, as shown in figure 4.5 (I). The wavy lines denote the photons emitted due to de-excitation of the molecules. The positions marked by a_1, b_1, c_1 are the initial positions of the emitted photons and a_2, b_2, c_2 are the positions where those photons have initiated secondary avalanches. The secondary avalanches created by the photo-ionization process are depicted in figure 4.5 (II), (III), (IV), (V) and (VI). Due to very high electric field the growth of the avalanche is very fast and before the avalanche reaches the anode, these photo-induced avalanches merge

into it. The space charge field of the combined avalanches becomes equal to the applied field and keeps on growing towards the anode. In this discharge case, the tip of the avalanche is populated with electrons and so named as negative streamer. As the growth takes place towards the anode, it is known as anode directed streamer.

Like the avalanche mode of operation, the streamer mode has its own merits and demerits, as the following.

- The large amount of induced charges rules out the necessity of pre-amplification.

- The large amount of charges takes a longer time to dissipate and increases the dead time and hence reduces the rate capability.

- The streamer pulse has an avalanche pre-cursor. Moreover, the time gap between the avalanche pre-cursor and the streamer pulse is not fixed, which worsens the time resolution. Sometimes an after pulse can be observed, which also affects the time resolution.

- The large amount of charges gets induced to more number of strips and the spatial information gets diluted.

In the next chapter a numerical method will be introduced which has been devised to emulate the dynamics of the charges taking place in the RPC as described in this chapter.

Numerical Modelling of RPC

In the previous chapter, the structure and working principle of RPC have been described briefly. Owing to its design, an RPC can operate in two modes, avalanche and streamer, depending upon the requirements of the experiments. The flexibility in its design can offer excellent time resolution (few hundreds of picosecond) and very good spatial resolution (few hundreds of micrometer) as well. As a result, the RPC is widely used for both tracking and triggering purposes in high energy physics (HEP) experiments. Such a diverse use of this detector has prompted the HEP community to use numerical simulation as another tool to understand its mechanism in order to predict its performance in various experiments or interpret and analyze the observed data. Many attempts have been made to simulate the avalanche and streamer modes of functioning of RPC. Most of them are based on either Monte Carlo methods [92, 94, 95, 96, 97] or hydrodynamic approach [98, 99, 100]. A review of different simulation methods can be found here [101].

In this chapter, a numerical model will be first described which has been built

on the basis of hydrodynamic model of electronic and ionic transports to simulate the streamer and avalanche modes of RPC. It studies the growth and propagation of the charges in an RPC produced due to incident cosmic muons at different applied voltages. The entire framework has been developed on the platform of a commercial Finite Element Method (FEM) package, COMSOL Multiphysics [102]. It has utilized relevant information of primary ionization produced by a package HEED [103], and electron transport parameters in the gaseous medium produced by another package MAGBOLTZ [104] that are required to carry out the simulation. The procedure to calculate efficiency and streamer probability of the RPC operated with a given gas mixture using this numerical model will be described next. The results will be compared to the experimental data [105, 106, 107] available for several R134a-based gas mixtures in order to validate the numerical model.

In section 5.1 the numerical model will be described. The next section 5.2 will be dedicated to the discussion of the avalanche and streamer discharge simulations using the model. The next section 5.3 present a procedure of calculating a few detector responses, such as the streamer probability and efficiency, using the simulation. Following this, in section 5.4 the simulated efficiency and streamer probabilities will be compared with experimental measurements reported in [105, 106, 107].

5.1   Numerical Modelling

The present numerical model has considered the gas mixture as a charged solution. It assumes the neutral gas molecules as the solvent and all the charge species

(electrons and ions) produced in the medium due to ionization as well as photo-ionization as solutes. In the following section 5.1.1, the geometry of the RPC that has been considered in the simulation will be described. In the next section 5.1.2, the mathematical model following the hydrodynamics adopted to carry out the simulation will be discussed. The conditions to identify the avalanche and streamer modes of operation will be mentioned in the section 5.1.3.

5.1.1   Model Geometry

3D modelling of an RPC would obviously be the best choice for simulating the charge dynamics in the device. However, it has not been attempted in the present study as it involves extensive computational expenses. Both of the 2D Cartesian and axisymmetric modelling approaches have their own advantages and limitations. In the Cartesian modelling, the charge growth is simulated in the 2D transverse cross-section (XZ-plane) of the detector active volume. On the other hand, the axisymmetric model simulates the growth on one side of the Z-axis and imposes rotational symmetry to achieve an approximate 3D representation of the physical processes at lower computational expenditure. In the present work, the 2D Cartesian model has been implemented to achieve the two-dimensional growth of the avalanche.

The RPC model has a gas gap (along Z-direction) of 2 mm, as illustrated in figure 5.1. The electric field has been applied across the gas gap along the positive Z-direction. The length of the RPC has been considered 1 mm only in the X-direction because the maximum radius of avalanche or streamer never exceeds $\frac{1}{\alpha}$ [91], where α is the first Townsend coefficient. It is of the order of 10 mm^{-1} for

the gas mixtures in consideration. The model has assumed geometrical symmetry along the Y-direction up to the length mentioned in the physics modules, which is 1 mm in this case.
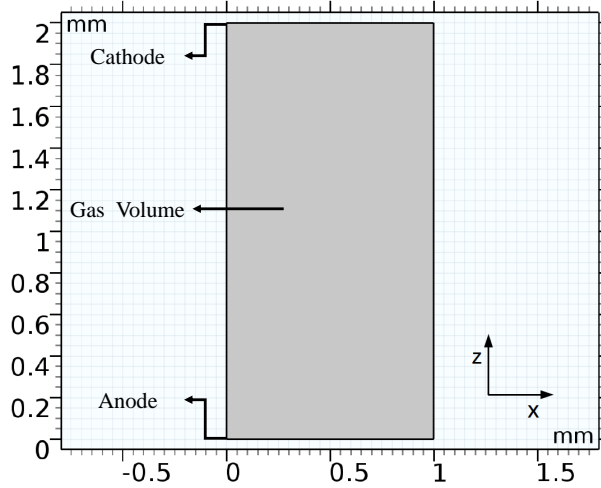
Figure 5.1: Geometry of the model.

5.1.2   Mathematical Model

In gaseous ionization detectors, the filling gas usually comprises two individual gas components. The principal component acts as the medium of Townsend ionization and constitutes the larger portion of the mixture. Whenever a charged particle passes through the detector, it generates primary pairs of electron and ion through ionization alongside excitation of the gaseous molecules. The de-excitation process releases photons which induce additional ionization, namely photo-ionization, along with the Townsend one. So, a second poly-atomic component is included in the gas mixture to serve as a quencher of the photons and thus reduce the contribution of photo-ionization.

Since the concentration of the charges is much less than that of the neutral gas molecules, the transport of the charges has been modeled using the *"Transport of Dilute Species"* module of COMSOL [102]. The following drift-diffusion-reaction expressed by equation 5.1 has been solved to compute the field dependent charge transportation.

$$\frac{\partial n_k}{\partial t} + \vec{\nabla} \cdot (-D_k \vec{\nabla} n_k + \vec{u}_k n_k) = R_k \tag{5.1}$$

$$R_k = S_e + S_{ph} \tag{5.2}$$

$$S_e = (\alpha(\vec{E}) - \eta(\vec{E}))|\vec{u}_e| n_e(\vec{x}, t) \tag{5.3}$$

$$S_{ph} = Q_e \mu_{abs} \psi_0 \tag{5.4}$$

where n_k, $k = i, e$, represents the concentration of the ions and electrons respectively while D_k, $\vec{u}_k$ and R_k are their diffusion, drift velocity and rate of production, respectively. As it is obvious from equation 5.2, R_k is the sum of two source terms, S_e and S_{ph}, of the charges produced through Townsend ionization and photo-ionization mechanisms, respectively. According to equation 5.3, S_e is dependent upon the transport parameters of electrons which are Townsend coefficient, α, attachment coefficient, η, and drift velocity, $\vec{u}_e$. The parameters have been calculated using MAGBOLTZ [104] for the given gas mixture under study. The S_{ph} can be computed using equation 5.4 where Q_e is quantum efficiency of the filling gas for electron generation from photo-ionization, μ_{abs} is photo-absorption coefficient of the quencher, and ψ_0 is the photon flux generated in the detection volume. The μ_{abs} has been calculated considering the corresponding photo-absorption cross-section of the specific gas component obtained from relevant sources. To determine ψ_0, a diffusion like approximation of the photon propagation in the gas medium, as shown in equation 5.5, has been considered

following Capeillère et al. [108]. It has been computed using *"Coefficient Form Partial Differential Equation"* module of COMSOL [102].

$$\vec{\nabla}(-c\vec{\nabla}\psi_0) + a\psi_0 = f \tag{5.5}$$

$$c = \frac{1}{3\mu_{abs}} \tag{5.6}$$

$$a = \mu_{abs} \tag{5.7}$$

$$f = \delta S_e \tag{5.8}$$

Here, δ in equation 5.8 represents the number of excited molecules for each ionized molecule.

It is well known that the slow movement of ions gives rise to subsequent development of space charge in the detector that can distort the applied electric field. So, the electric field, $\vec{E}$, has been calculated at small-time steps taking into account the space charge density, ρ, using the following equations 5.9 and 5.10. The *"Electrostatic"* module of the COMSOL [102] has been used for this purpose.

$$\vec{E} = -\vec{\nabla}V \tag{5.9}$$

$$-\vec{\nabla}d_y(\epsilon_0\vec{\nabla}V - \vec{P}) = \rho \tag{5.10}$$

$$\rho = q_e(n_i - n_e) \tag{5.11}$$

where V is the potential, q_e is the magnitude of the charge of the electron, d_y is the depth in the Y-direction, $\vec{P}$ is the polarization vector, ϵ_0 is the permittivity of the vacuum. This is a three-dimensional problem being solved in two dimensions. So, the electric field is calculated in a plane and COMSOL assumes that there is symmetry in the perpendicular direction of the plane. The term d_y denotes the depth up to which this symmetry is assumed. So, multiplying this depth with

the amount of charge in a plane gives the total amount of charge in the volume with the depth d_y. The change of electric field has been considered in the X and Z-directions, while it has been considered constant in the Y-direction.

The following boundary conditions have been used in the model. The loss of electrons from the gas gap upon reaching the anode has been taken care of by assuming drift of the electrons through the anode. Similar condition has been set about the ions to consider their outflow at the cathode. To incorporate the processes of electrons and ions diffusing and drifting out of the simulated volume, the two boundaries other than the cathode and the anode have been assumed open for them. The photon flux at the electrodes has been taken as zero, as these electrodes are made up of those materials which do not have scintillating property. This condition has been implemented as a Dirichlet boundary condition in the model. The photon propagation out of the simulation volume has been taken into account by considering the two boundaries other than the electrodes open for them.

5.1.3   Conditions for Avalanche and Streamer

The main characteristic of streamer is that the electric field due to space charge equals the applied electric field [93, 91]. On the other hand, in case of avalanche, the number of electrons becomes zero due to their loss upon reaching the anode. These two conditions have been utilized to identify the streamer and avalanche and subsequently stop the simulation. The aforementioned conditions have been implemented in the following way:

- **Avalanche:** All the electrons have been collected in the anode.

- **Streamer:** When the space charge field has become equal to the applied field ($\gamma = 1$) where $\gamma = (E_{total} - E_{applied})/E_{applied}$ is a parameter for comparing the space charge field to the actual applied one.

5.2   Simulated Avalanche and Streamer Discharge

Figure 5.2 and 5.3 are typical examples of avalanche and streamer events, respectively, where the evolution of the electron density with time in the gas gap for both the conditions have been depicted. The color code represents the natural logarithm of the electron density in the gas gap. The boundary for each time slice denotes the boundary of the model geometry. In figure 5.3, the movement of the higher electron density region towards the cathode can be seen, as is observed experimentally in case of positive streamers.
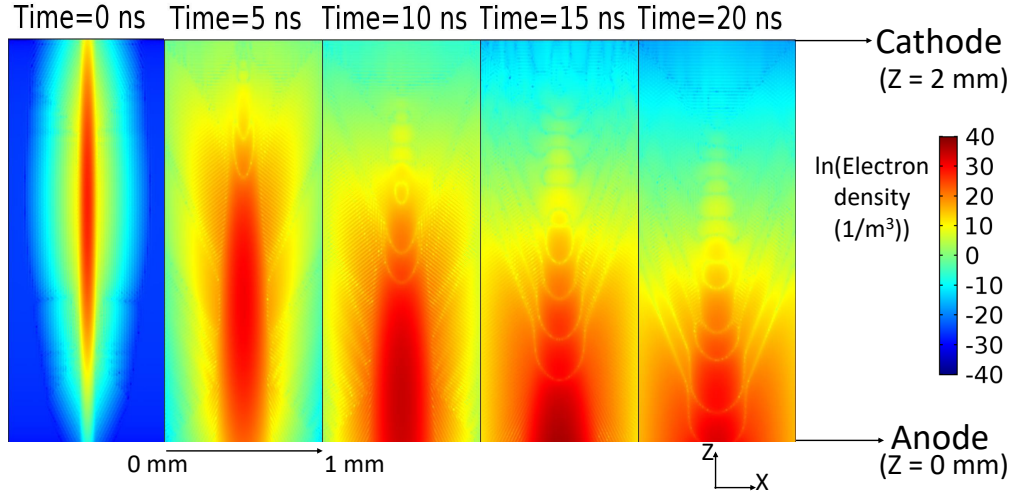
Figure 5.2: Growth of electronic charges in RPC for avalanche at 41 kV/cm for 10 primary electrons with mean Z-position of 1.2 mm

In figure 5.4, time evolution of the electric field and electron density for the streamer condition at applied field 47 kV/cm is shown. The background solid
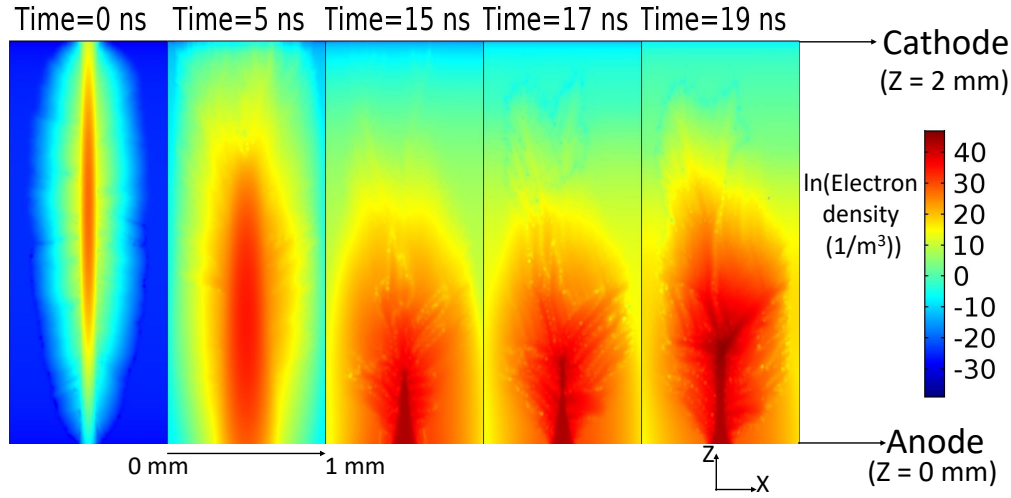
Figure 5.3: Growth of electronic charges in RPC for streamer at 47 kV/cm for 10 electrons with mean Z-position of 1.2 mm

color depicts the natural logarithm of the electron density at the two specific instants mentioned in the figure, and the contours represent the electric field. It is clear from the plot of the second instant (at 19 ns) that at the tip of the streamer, the electric field is double of the applied one. It indicates that the space charge field is of the same magnitude of the applied field, which is one of the characteristics of the streamer condition. Another important characteristic of the streamer event is a precursor which is a comparatively smaller signal occurring before the actual streamer. It has also been observed in the simulation of the induced current. In the simulation, the induced current for each event has been calculated following Ramo's theorem [90] expressed by equation 5.12. The induced current, *i(t)*, at an instant, *t*, depends upon the $\vec{E}_w$ (weighting field), the electric field in the gas gap when the pick-up electrode of interest is raised to potential V_w while all other electrodes are grounded, $\vec{u}_e(t)$, the instantaneous electron drift velocity, and *N(t)*,
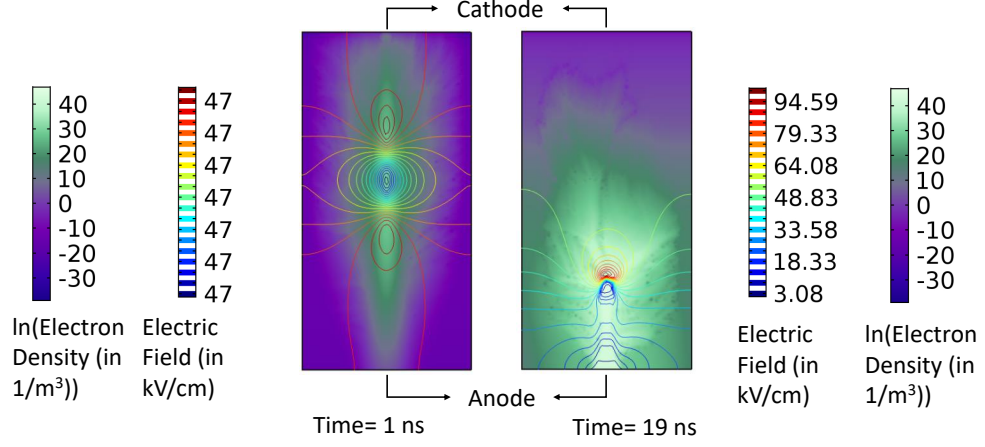
Figure 5.4: Time evolution of electric field and electron density at applied field 47 kV/cm

the number of electrons present at time t multiplied by the electronic charge, q_e.

$$i(t) = -\frac{\vec{E}_w \vec{u}_e(t)}{V_w} q_e N(t) \tag{5.12}$$

$$\frac{E_w}{V_w} = \frac{\epsilon_r}{2b + d\epsilon_r} \tag{5.13}$$

The equation 5.13 presents the magnitude of the weighting electric field for unit weighting potential which is dependent on the relative permittivity of the electrodes, ϵ_r, and the thicknesses of the electrode and gas gap, b and d, respectively. A plot of the induced signal for one such case where a pre-cursor appears before the streamer has been shown in figure 5.5.
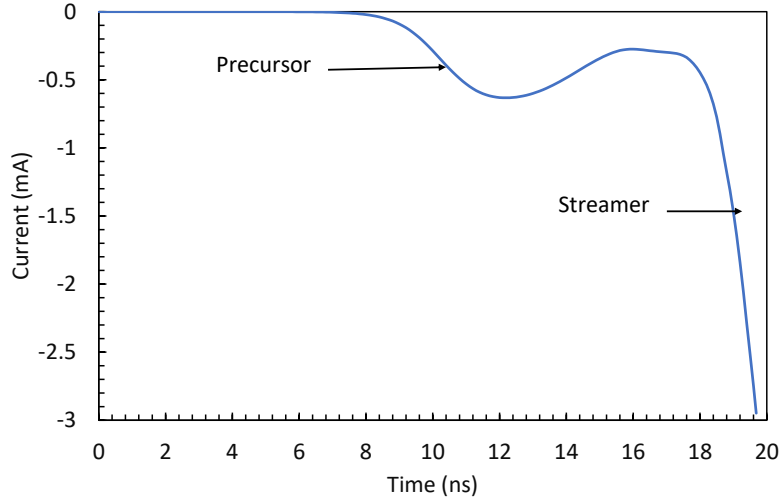
Figure 5.5: Induced current in case of a streamer event at 47 kV/cm

5.3 Calculation of Streamer Probability and Efficiency

A method of calculating the detector responses of streamer probability and the efficiency at different applied voltages, which are considered as figures of merit of RPC operation, for the given gas using the numerical model will be described in this section. For validation of the calculation procedure, the results will be compared with experimental data presented in several references [105, 106, 107]. Two gas mixtures have been considered for the calculation. One of them is a mixture of R134a(95%):n-C_4H_{10}(5%) [105] and the other is the usual one of R134a(95.2%):i-C_4H_{10}(4.5%):SF_6(0.3%) [106, 107] which will be used in the RPCs of the ICAL with same volumetric percentages. In this work, 1 bar pressure

and 293.15 K temperature have been maintained throughout the calculation.

5.3.1   Event Generation

In the simulation, a flux of 10,000 cosmic muons with energy between 1 - 10 GeV have been considered for event generation in the RPC. As the efficiency and streamer probability of the detector are independent of the direction of incidence of the charged particle, for brevity only those muons falling within zenith angle 0° - 13° have been considered. Eventually, the cosmic muon flux given by Tang et al. [109] has been followed and HEED has been used to compute the number of primary electrons generated in the gas gap due to ionization caused by these muon events. For each muon event, it has provided the number of primary clusters, their position and number of electrons lying in each cluster. It has been found that the clusters are distributed throughout the whole gas gap and in most cases contain one electron. Instead of carrying out the simulation of the growth of each cluster produced in a muon event, those have been collectively represented as a single cluster with its Z-position and size (number of electrons in it) calculated from this information of each cluster as provided by the HEED in the following way. The Z-position of the representative cluster for an event has been obtained from the weighted mean of the same of all the primary clusters and its size from the sum of all the primary electrons created in that event. Further, these events with representative seed clusters having similar size and mean Z-positions falling within a specified range have been considered as a group. Eventually, the simulation of charge growth following hydrodynamics has been carried out for a single seed cluster has belonging to the group of events. This approach of
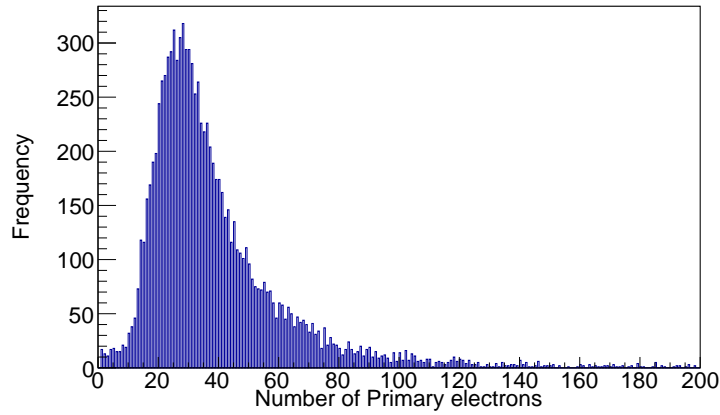
Figure 5.6: Total number of electrons for the gas mixture R134a (95%):n-C_4H_{10}(5%).

simulation has reduced the computation expense significantly. All the cosmic muon events thus have been classified according to their mean Z-position and the total number of primary electrons.

The method can be explained with an example of the gas mixture of R134a(95%): n-C_4H_{10}(5%). In figure 5.6 the histogram of primary electrons produced by the HEED in the said gas mixture for 10,000 muon events is shown. It can be seen that for nearly 90% of the events, the total number of primary electrons lie between 10 and 60. The rest are smaller and bigger clusters, which are very few in frequency. Eventually, these clusters have been ignored for the reason that the events which have fewer electrons than 10 and created very near to the anode will not produce either a streamer or an avalanche large enough to be detected by the electronics available. On the other hand, the events which have higher number of total electrons may be located at any position in the gas gap and lead to formation of avalanche and streamer depending upon their position. A calculation carried out including the events with cluster size larger than 60 and generated away from

the anode has demonstrated an increase in the computational time without affecting the result much. Therefore, to save the computational expenditure at the cost of marginal error, these events have been opted out of the calculation. For the rest 90% of total 10,000 muon events, the seed clusters have been produced for each case and further grouped following a range of 0.1 mm in their mean Z-position and 5 in the cluster size. Figure 5.7 depicts a 2D histogram of the size and mean Z-position of the seed clusters for the 90% muon events considered in the simulation for the gas mixture of R134a (95%):n-C_4H_{10} (5%). It shows the distribution of the seed clusters according to their mean Z-position binned with a bin size of 0.1 mm over a range of 0.1 - 1.9 mm and the number of primary electrons with a bin size of 5 over a range of 10 - 60. The frequency for each 2D cell has been written there, which denotes the number of events having seed clusters with mean Z-position and size falling within the range of the respective cell. For each cell, the hydrodynamic simulation has been carried out considering the minimum mean Z-position and size of the respective cell. Depending upon the charge evolution simulated by the model with the said Z-position and size, all the events belonging to the cell have been classified as avalanche or streamer events. The same 2D histogram for the gas mixture of R134a (95.2%): i-C_4H_{10} (4.5%): SF_6 (0.3%) has been illustrated in figure 5.8 which has been produced following the method described above.

The seed cluster has been represented by a Gaussian distribution [98] with its mean position same as the mean Z-position considered for the respective group of events. As the simulation has considered a 2D model of the RPC in the XZ-plane, a two variable Gaussian distribution has been used. The standard deviation for the Z-variable of the Gaussian has been kept fixed for each seed cluster, with the
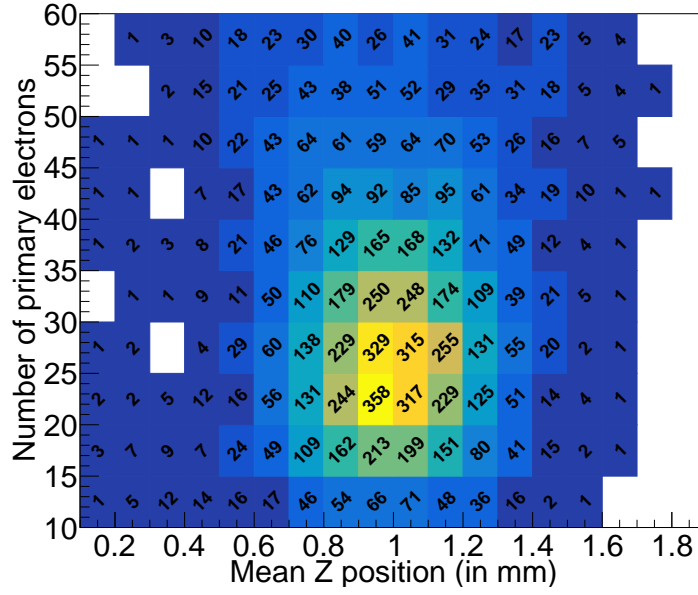
Figure 5.7: 2D histogram of muon events for the gas mixture of R134a (95%):n-C_4H_{10} (5%).

condition that the 5σ of the distribution always remains bound by the electrodes. As mostly vertical muon events have been considered, the mean of the X-variable of the Gaussian has been considered to be 0.5 mm, which is at the middle of the model geometry.

5.3.2   Estimation of Detector Responses

It is obvious from the discussion in section 5.3.1 that for each of the 10,000 muon events, a seed cluster having definite size and mean Z-position could be prepared to initiate the hydrodynamic simulation of detector response for a given voltage configuration. From the numerical study, a correlation of the occurrence of avalanche or streamer at an applied voltage to the size and the position of the seed cluster has been observed. Therefore, the avalanche and streamer modes are viable to be distinguished on the basis of these two parameters. Once the
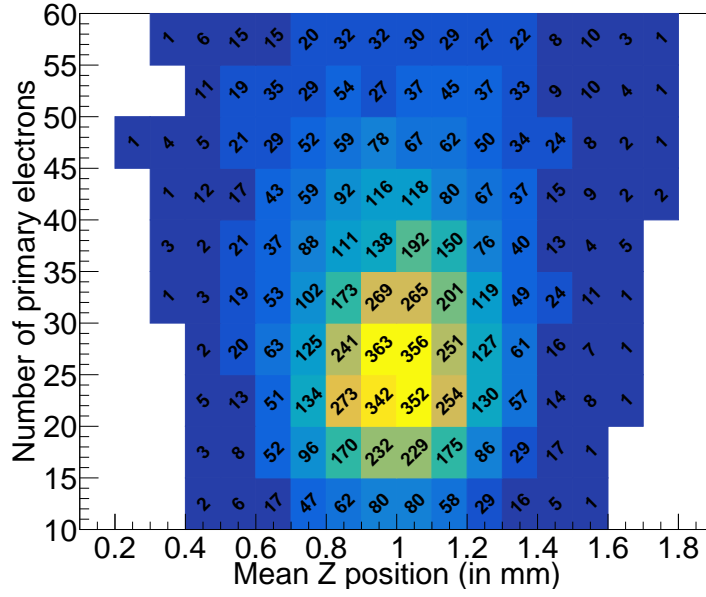
Figure 5.8: 2D histogram of muon events for the gas mixture of R134a (95.2%):i-C_4H_{10} (4.5%):SF_6 (0.3%).

least cluster size to develop into a streamer for a given mean position has been determined, it is obvious that all the larger clusters should lead to streamer. A similar condition could be identified for the mean Z-position for a given cluster size. For example, if it is found that for applied electric field 47 kV/cm, the seed having 10 electrons and the minimum mean Z-position 1 mm grows to a streamer, then all the events with seeds of higher mean Z-position (away from the anode) and number of primary electrons will lead to streamer discharge at the same electric field. Using these observations, the group of events from the 2D histogram leading to either of the avalanche or streamer without carrying out the hydrodynamic simulation for all have been identified. It has facilitated the estimation of the total number of events leading to either of the avalanche or streamer from summing up the frequency of the respective groups. Subsequently, the streamer probability has been calculated, dividing the number of streamer

events by the total number of muon events.

Calculation of the detector efficiency has been done in similar manner. For this purpose, the current signal produced from the growth of the seed cluster has been determined. The procedure to calculate the induced current has been described in section 5.2. Only those events corresponding to the seed clusters that have produced signals crossing a predefined threshold of current, have been considered as valid events. In experiments, a signal in terms of voltage is collected after electronic amplification of the current signal across a load resistance. In the simulation, this has been implemented by calculating the current equivalent to the voltage mentioned as threshold after the electronic gain. The ratio of the valid events with respect to the total number of events has been defined as the detector efficiency.

5.4 Validation of Numerical Model

In this section, the aforementioned procedure of calculating streamer probability and RPC efficiency using the 2D histogram will be validated by comparing the results for different gas mixtures with respective experimental data. For the gas mixture of R134a(95%):n-C_4H_{10}(5%), the comparison of the calculated values of streamer probability and the efficiency will be compared to the experimental observation [105] in section 5.4.1. The following section 5.4.2 will discuss the comparison between experimental data presented in [106, 107] and simulated streamer probability and efficiency for the gas mixture of R134a(95.2%): i-C_4H_{10}(4.5%): SF_6(0.3%).

5.4.1   Comparison for R134a(95%):n-C$_4$H$_{10}$(5%)

For each combination of the size and mean Z-position of the seed cluster, the evolution of the charged fluid has been simulated at different applied voltages. Criteria discussed in section 5.1.3 have been used to determine the nature of the RPC signal as either of avalanche or streamer. In order to compare with the experimental measurements of efficiency and streamer probability reported in [105], the same observable have been estimated using the present simulation model.

A threshold criterion following a similar condition mentioned in [105] has been used in the present calculation to select the valid signals as required to calculate the efficiency. In [105], it has been considered that the amplitude of the signal should be greater than 30 mV which is equivalent to 0.1 mV signal acquired across a 25 Ω resistor with an electronic gain of 300. In the present calculation, the current corresponding to this threshold criteria has been calculated and considered as the threshold to identify the valid events. In figure 5.9, a comparison between the simulation and experimental data for the efficiency has been plotted. The simulation has been carried out for two values of ϵ_r (relative permittivity of the electrode material) as that of the resistive material of the electrode can vary over the given range. The comparison of the calculated streamer probability with the experimental observation of [105] at different voltages has been shown in figure 5.10. It can be noted from the figures 5.9 and 5.10 that the simulation results have followed the experimental trend quite closely, although a quantitative agreement between them has not been achieved. One of the major reasons may be the lack of information on actual experimental conditions, which
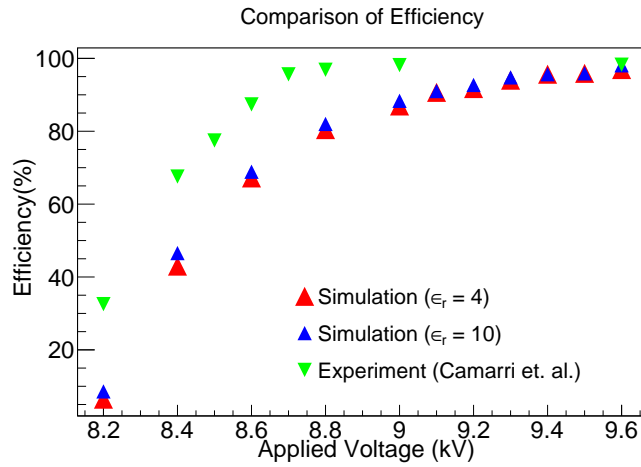
Figure 5.9: Efficiency as a function of applied voltage for R134a(95%):n-C_4H_{10}(5%).
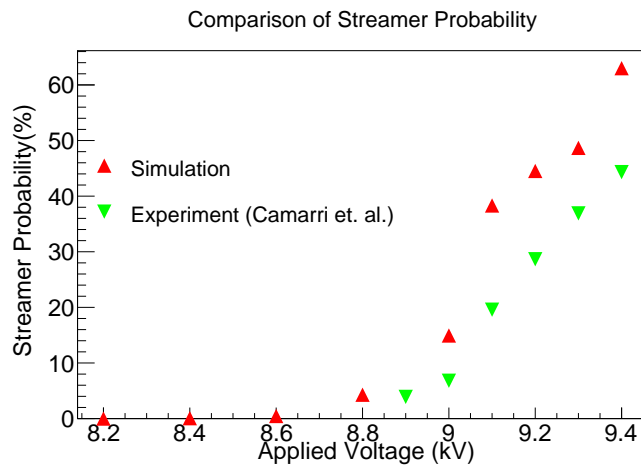
Figure 5.10: Streamer probability as a function of applied voltage for R134a (95%):n-C_4H_{10} (5%).

could not be included in the simulation. On the other hand, the simulation model also needs further investigation to improve its efficacy. The streamer probability as a function of efficiency as calculated and observed in the experiment, which has been depicted in figure 5.11. It shows that the calculated streamer probability has shown a steady rise to 15% as the efficiency has increased from 70% to 90%. In case of experiment, there is no streamer observed till 95% efficiency, and then
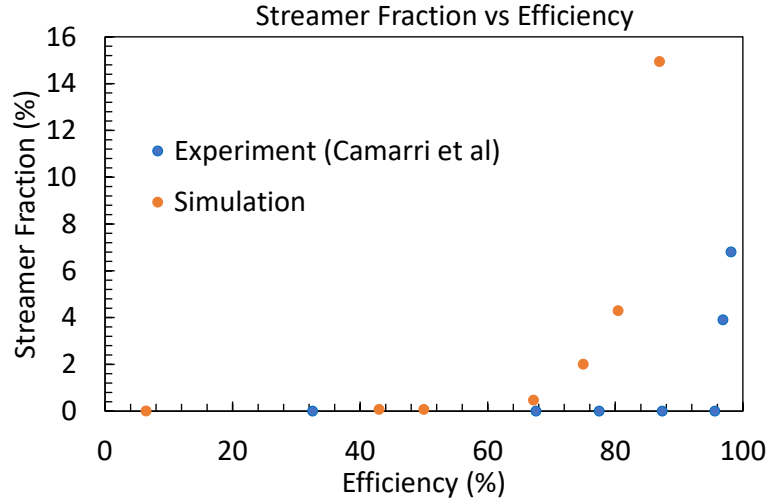
Figure 5.11: Streamer probability as function of efficiency for R134a (95%):n-C$_4$H$_{10}$ (5%).

it has increased sharply to about 7% only.

5.4.2   Comparison for R134a(95.2%):i-C$_4$H$_{10}$ (4.5%):SF$_6$(0.3%)

For this gas mixture, a different geometry of RPC has been considered in the simulation following the design parameters of the RPC used in the experiments. Here, 3 mm thick electrode with relative permittivity 6.25 has been used while calculating the weighting field. The current threshold has been set to 1.25μA which corresponds to a signal of 0.0625 mV for 50Ω termination. This is equivalent to 5 mV after an electronic gain of 80.

The calculated efficiency as a function of high voltage and the calculated streamer probability as a function of the efficiency have been shown in fig-

ure 5.12 and 5.13, respectively, for the standard mixture of R134a(95.2%):i-C$_4$H$_{10}$(4.5%):SF$_6$ (0.3%). Comparison with a few measurements [107, 106] has been depicted, which shows a close agreement between the simulation and the experiments.
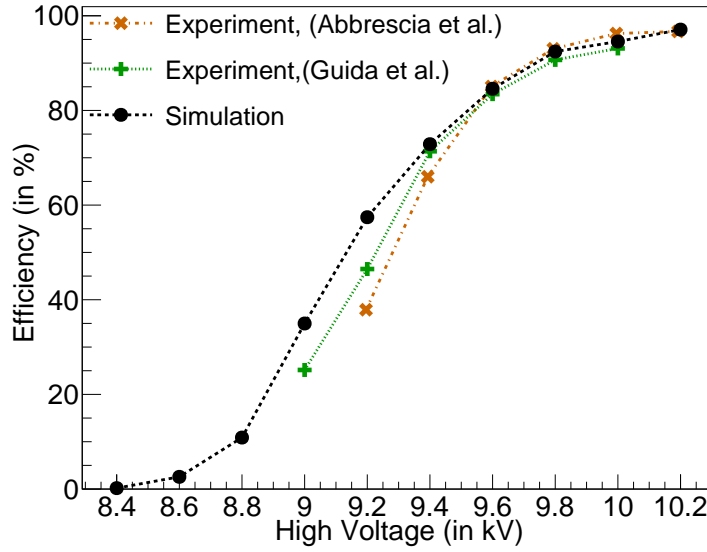
Figure 5.12: Comparison of efficiency as function of high-voltage between simulation (this work) and experiments [106, 107] for the gas mixture of R134a (95.2%):i-C$_4$H$_{10}$ (4.5%):SF$_6$ (0.3%).

It follows from the discussion of this chapter that the numerical model based on hydrodynamics is capable of emulating the RPC dynamics, reproducing the experimental observations reasonably well. In the next chapter, the experimental measurement of the efficiency and streamer probability of a prototype RPC fabricated following the design parameters of the same to be used in ICAL will be described. The experimental data will be compared with the calculated responses obtained by using the numerical model.
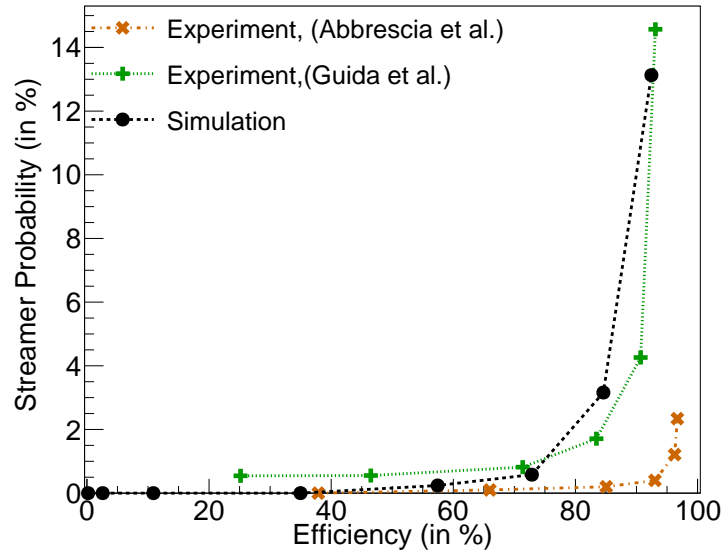
Figure 5.13: Comparison of streamer probability as a function of efficiency between simulation (this work) and experiments [106, 107] for the gas mixture of R134a (95.2%):i-C_4H_{10}(4.5%):SF_6(0.3%).

Experimental Studies

The performance of the RPC configured for the ICAL experiment has been studied by experimental measurements as well as numerical simulation to complement each other in realizing the device dynamics. The study has also provided an opportunity to assess the scope of the numerical model developed on the basis of hydrodynamics in emulating the working of the RPCs of the ICAL.

The chapter has been broadly divided into three sections to discuss the experimental and numerical work and their comparison, respectively. The section 6.1 will discuss the fabrication of a prototype RPC which has been subjected to experimental measurements of its responses. The experimental setup used for the measurement, analysis of experimental data and the results will be described in the following sections. The experimental result will be compared with the numerical results as obtained in the earlier chapter 5.

6.1 RPC Fabrication

The resistive electrodes of RPC can be made from either of a high pressure laminate Bakelite and float glass. Following are the steps typically followed to fabricate an RPC, which is basically a parallel plate chamber as described in chapter 4. In this work, a prototype of glass-based RPC to be used in ICAL has been constructed for carrying out the measurement of its efficiency and streamer probability at different applied voltages when operated with R134a(95.2%):i-C_4H_{10}(4.5%):SF_6(0.3%) gas mixture. Two float glass plates of dimension 30 cm × 30 cm have been machined with chamfered corners. The plates have been cleaned with propan-2-ol and lint free tissues before they have been subjected to painting of a conductive coating of graphite on one of the surfaces. A border of 1 cm width from all the sides has been covered with tape in order to prevent the region get coated with the conductive paint. This procedure has been followed in order to rule out the discharge that can take place between the two plates at the edge when a high voltage is applied.

A special conductive paint from Kansai Nerolac has been mixed with thinner material in appropriate proportion to achieve the required surface resistance of the coating. Using spray gun, a uniform coating has been made on the surface with care and not letting the paint thick enough to drip. Also, the surface resistance depends on the thickness of the coating and painting more than once should be avoided for this reason. The coated electrodes have been left for 24 hours to cure. Improper coating followed by insufficient curing may lead to peeling or cracking of the conductive paint.

For Bakelite electrode, a thin linseed oil coating needs to be applied to reduce

the surface asperity which is common in Bakelite material. The glass electrodes do not require this treatment, as their surface is much smoother. Side spacers of poly-carbonate material with 1 cm width and 2 mm height have been machined and glued to the electrodes using DP-190 (gray) glue [110]. The glue has a working life of 90 minutes and requires 7 days to cure properly. While gluing, care has been taken so that the glue does not touch the conductive coating, as this creates a path for leakage current. Five button spacers of 6 mm diameter and 2 mm thickness have been glued at specific locations of regular interval and cured in the same way. The side spacers and the button spacers have been glued to one of the electrode and left for the glue to cure properly. Once it had cured properly, then glue has been applied on other side of the spacers to fix with the other electrode. For gas circulation through the RPC, two gas nozzles have been fixed through the edge spacers at opposite sides of the RPC. Different stages of fabrication of the glass RPC have been shown in figure 6.1.

After the curing process is complete, the detector has been put under leak test. For this purpose, the outlets of the RPC has been connected to a manometer filled with a liquid of high boiling point. Using the inlet of the RPC, an over pressure has been built up inside it and the inlet has been closed subsequently. The over pressure has caused the liquid level in the manometer to rise in one arm. The change in the reading of the liquid level in both the arms due to the over pressure has been noted. If the RPC can withhold the over pressure which can be noted from the manometer reading, for more than 24 hours, the RPC is approved with gas tightness. For making high voltage connection on the conducting surface of the glass electrodes, a piece of copper tape has been pasted at one corner. A mylar sheet of the same dimension as the RPC has been pasted over the conductive

Spray painting of glass electrode

Spacers and gas nozzles

Surface resistivity measurement

Leak test of RPC

A glass RPC with high voltage connection and pickup panel
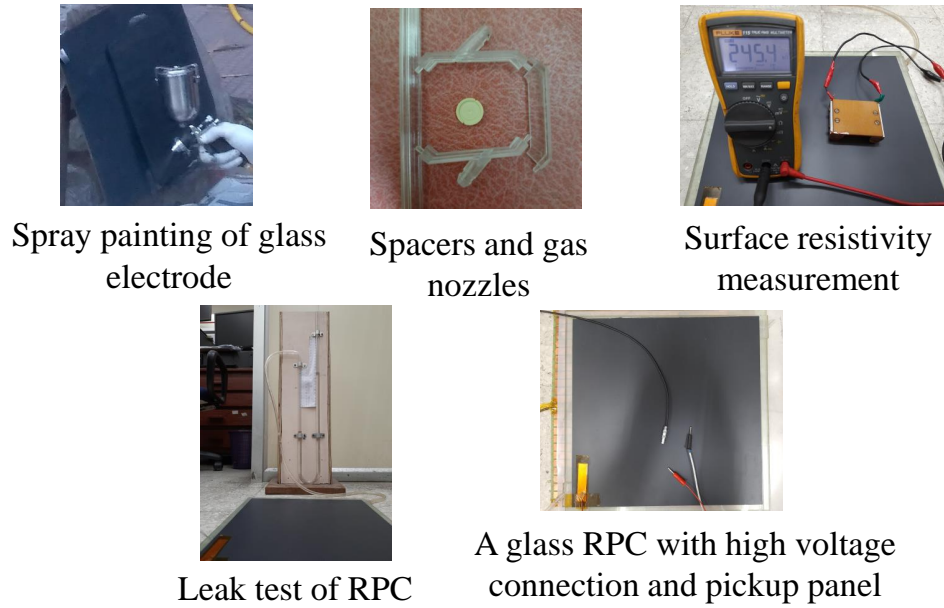
Figure 6.1: Different stages of a glass RPC fabrication.

coating to isolate the electrode from the pickup panel that have been then fixed on the electrodes. These panels have been made of either FR4 boards or honeycomb structure made of G-10 material with copper strips pasted on them. In this case, the pickup panels have been made of the latter. The copper strips are 2.8 cm wide and the gap between them is 0.2 mm. Each of the strips has been grounded through a 50Ω resistance for impedance matching. For collecting signals from the strips, co-axial cables of line impedance 50Ω have been connected with their ground and that of the pickup panels connected to the common ground. For electrical characterization of the RPC, its V-I characteristics has been studied after flowing the gas mixture R134a(95.2%):i-C_4H_{10}(4.5%):SF_6(0.3%) through the RPC.

6.2   Experimental Setup and Data Acquisition

The experimental setup to study the response of the glass RPC in detecting the cosmic muons consists of and three plastic scintillator detectors in addition to the glass RPC as shown in figure 6.2. The scintillators have been used for generating
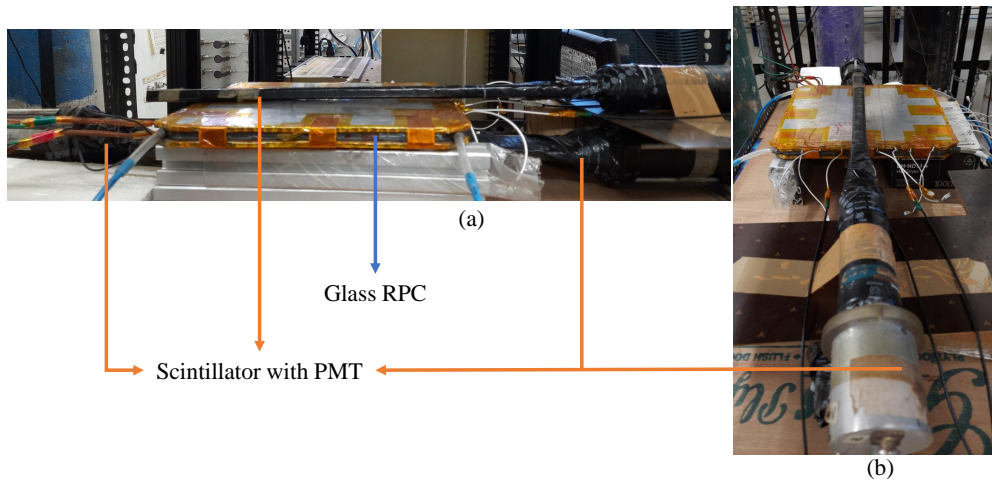
Figure 6.2: Experimental setup a) Side view, b) Front view.

muon triggers from their coincidence to record the data corresponding to cosmic muon from the RPC. These scintillator detectors have been aligned with one of the RPC pickup strips and the data have been acquired from this strip and its two neighboring strips on either sides. The scintillator detectors are of the same width as the RPC strip.

Biasing of the RPC has been done using CAEN A1526 module housed in CAEN SY4527 multichannel power supply system. The power supply system can provide up to 15 kV of voltage with current up to 1 mA. Both the positive and negative polarity of A1526 have been used to provide high voltages to the anode and cathode of the detector. The voltage difference over a range of 4.5 -

6.0 kV has been supplied while carrying out the experiment. The biasing of the
Photo Multiplier Tubes (PMTs), connected to the scintillator detectors, has been
done individually using ORTEC 556 high voltage module which can supply up
to 3 kV of high voltage. To each of the PMT, a high voltage of 1.8 kV has been
supplied. These components are shown in figure 6.3

ORTEC 556 HV	CAEN LTD N844	CAEN A1526 HV	ORTEC CO4020	CAEN SY4527
supply	Discriminator	supply	Logic unit	Multi channel
				HV supply

Figure 6.3: Electronics modules used for experiment.

The RPC signals are very small in amplitude when operated in avalanche
mode and have very sharp rise time, which requires pre-amplification of the
signals. For this purpose, a two-stage Hybrid Micro Circuit (HMC) chip-based
amplification system has been designed with total gain of 80 [111]. The circuit
diagram of the pre-amplifier board is given in figure 6.4 and the details of the
chips are furnished in table 6.1

As shown in the schematic diagram of the experimental setup 6.5, the scintil-
lator signals have been first digitized using CAEN N844, which is an 8-channel
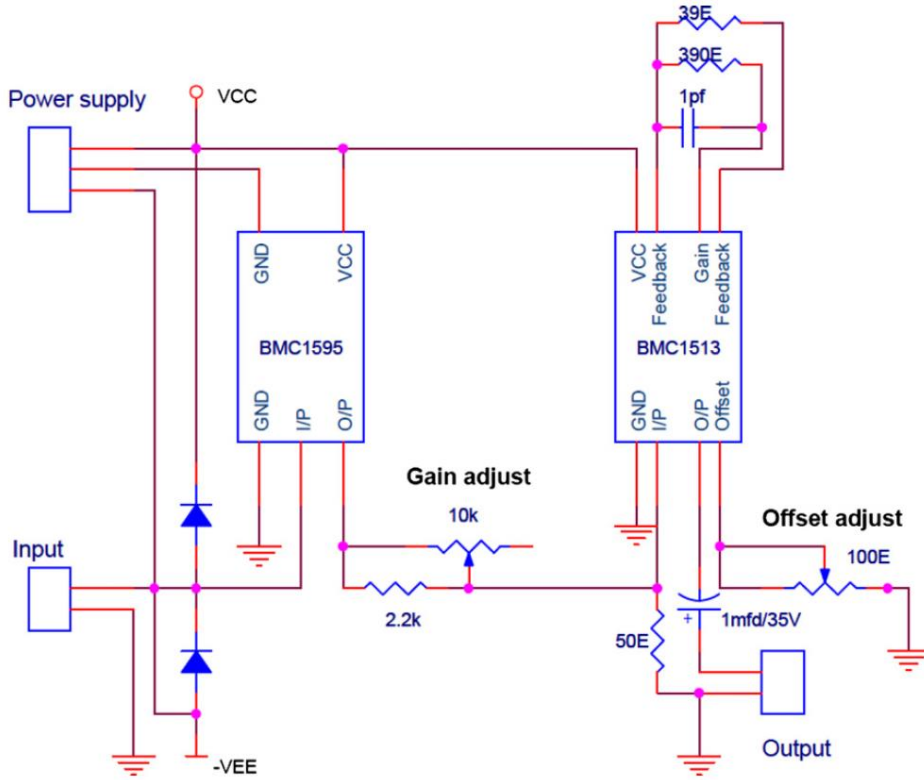
Figure 6.4: Schematic of the HMC based pre-amplifier board [111].

Parameter	First stage HMC	Second stage HMC
Input impedance	50Ω	50Ω
Input dynamic range	100 mV	200 mV
Nominal gain	10	10
Bandwidth	~ 300 MHz	~ 250 MHz
Rise time	~ 1.2 ns	~ 2 ns

Table 6.1: Parameters of HMC based pre-amplifier board. [111].

low-threshold discriminator, and then passed to a logic unit, ORTEC CO4020, which is a quad 4-input logic unit for AND operation to generate the coincidence signal of three scintillator detectors. For data acquisition, a Mixed Signal Oscil-
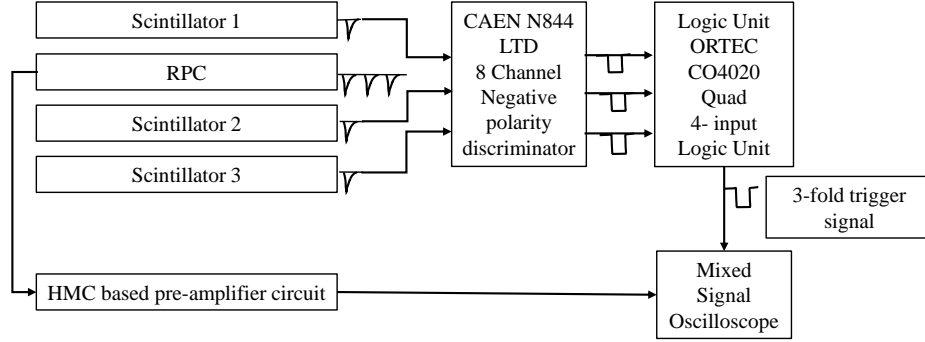
Figure 6.5: Schematic diagram of the experimental setup.

loscope (MSO) has been used where the data have been stored in .csv format at 5 GS/s rate. The data have been later retrieved for analysis.

6.3 Analysis Method

The experimental data have been analyzed by developing and using a C++ based analysis code and ROOT data analysis framework. The oscilloscope has stored the amplitude (in mV) for each small-time steps (width 0.2 ns) in a 400 ns window with time stamp. When the trigger signal reaches the oscilloscope, it has recorded data of a window of 400 ns width starting 200 ns before the trigger. The triggering system has been delayed to make the RPC signal reach 60 ns before the trigger pulse. The raw data have been converted to .ROOT format for storing and further processing. A mean baseline value has been calculated using the post-trigger information for each event, as shown in figure 6.6. This
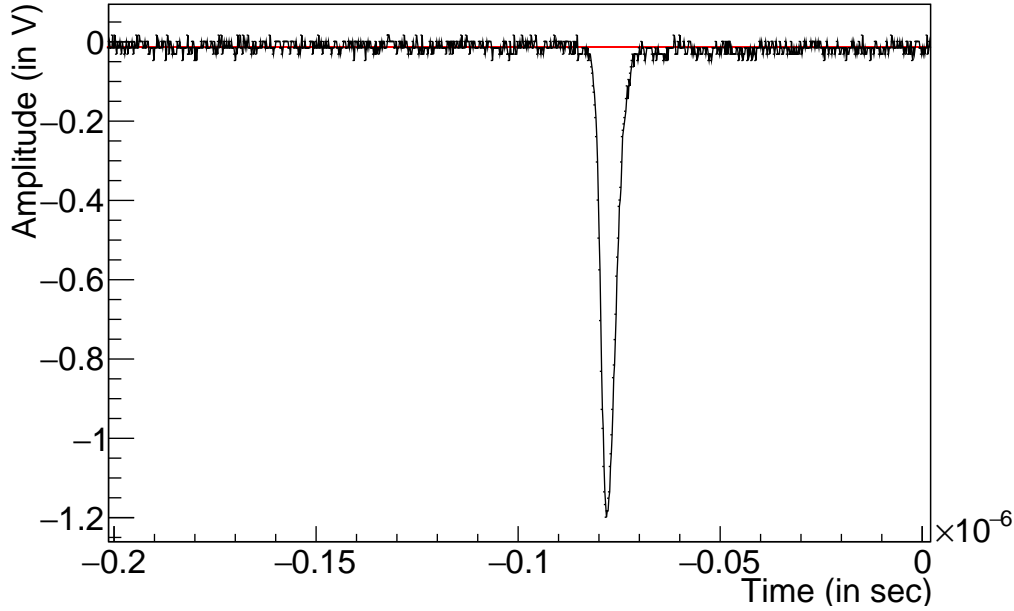
Figure 6.6: RPC signal at 10 kV with baseline calculated using post-trigger information, depicted in red.

mean baseline value has been subtracted from the amplitude of the pre-triggered data. The signal after the subtraction of baseline has been converted to charge by taking into the amplification factor and load resistance of the oscilloscope. The co-axial cable and copper strips of the pickup panels of RPC have an impedance of 50 Ω and hence the load resistance of the oscilloscope has been chosen to be the same. From the correlation between maximum amplitude and total charge in the pre-triggered region, the threshold voltage for a valid signal has been decided.

The efficiency at each voltage has been calculated by dividing the number of valid signals with the total number of 3-fold coincidence triggers generated by the set of scintillator detectors. All the events with total charge $\geq$ 3 pC have been denoted as streamer event and the streamer probability has been calculated by dividing this number by total number of triggers.

6.4   Results

With the experimental setup described before, the test of the RPC, has been carried out for the gas mixture of R134a(95.2%):i-C_4H_{10}(4.5%):SF_6(0.3%). In this section, the results of this experiment will be discussed and compared with the simulation result.

The measured efficiency of the RPC as a function of the applied high-voltage has been shown in figures 6.7. It can be noted from the plot that an efficiency of 90% has been achieved at the high-voltage of 9.6 kV. The error at each point has been calculated assuming Poissonian error in both trigger counting and valid signal counting. and further improves to 93-94% with the increase in applied
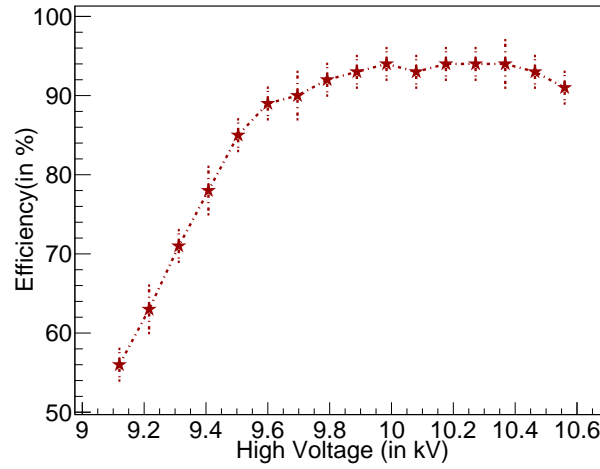
Figure 6.7: Efficiency of a glass RPC as function of high-voltage for the gas mixture of R134a(95.2%):i-C_4H_{10}(4.5%):SF_6(0.3%).

voltage. The efficiency remains the same providing an operating voltage regime of width about 1 kV. The time resolution of the detector has been determined using Constant Fraction Discrimination (CFD) method, where the timing information has been recorded as the arrival of the RPC signal. When the signal has crossed

30% of the maximum amplitude, the corresponding time is noted as the arrival time. This method helps to reduce the error due to amplitude walk of the RPC signal. For a certain voltage, a histogram of the arrival time of all the valid signals has been fitted with a Gaussian function, as shown in figures 6.8(a) and 6.8(b) for two cases of applied voltages. The standard deviation of the Gaussian has
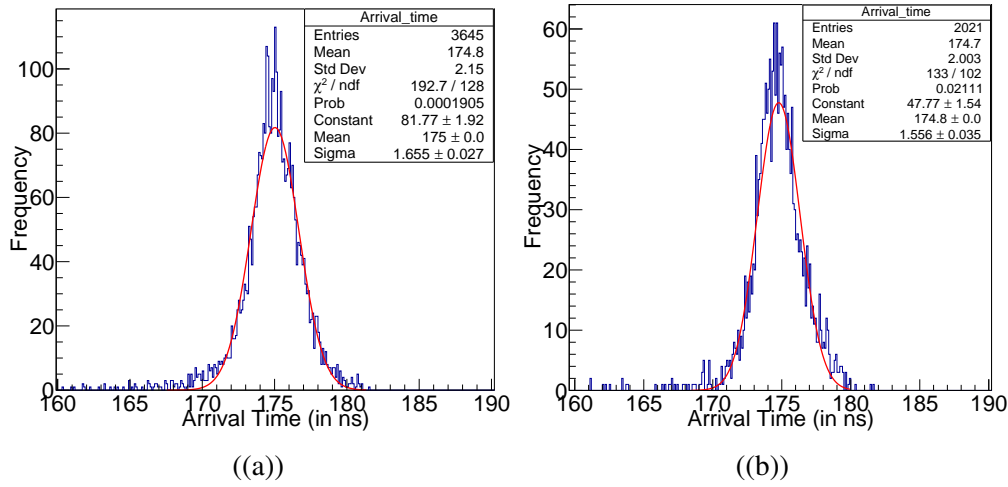
Figure 6.8: Distribution of arrival times for a) 9.2 kV, b) 9.3 kV.

been defined as the time resolution of the detector at the respective voltage. The error of the standard deviation has been taken as the error of the time resolution. A plot of the time resolution over a range of high-voltage from 9 to 10.6 kV has been depicted in figure 6.9 which shows that the resolution has improved with increase in the voltage. For each valid RPC signal, using the threshold decided for that voltage the signal span has been calculated by finding out the time over threshold for the signal as shown in figure 6.10. The voltage has been integrated over this time span and converted to charge using the amplification factor and value of the load resistance. A histogram has been made using the total charge of each valid signal collected for a given applied voltage. The histogram has been
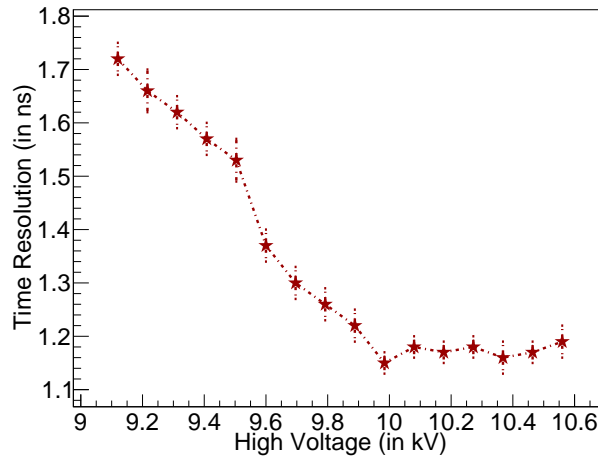
Figure 6.9: Time resolution as function of high-voltage.
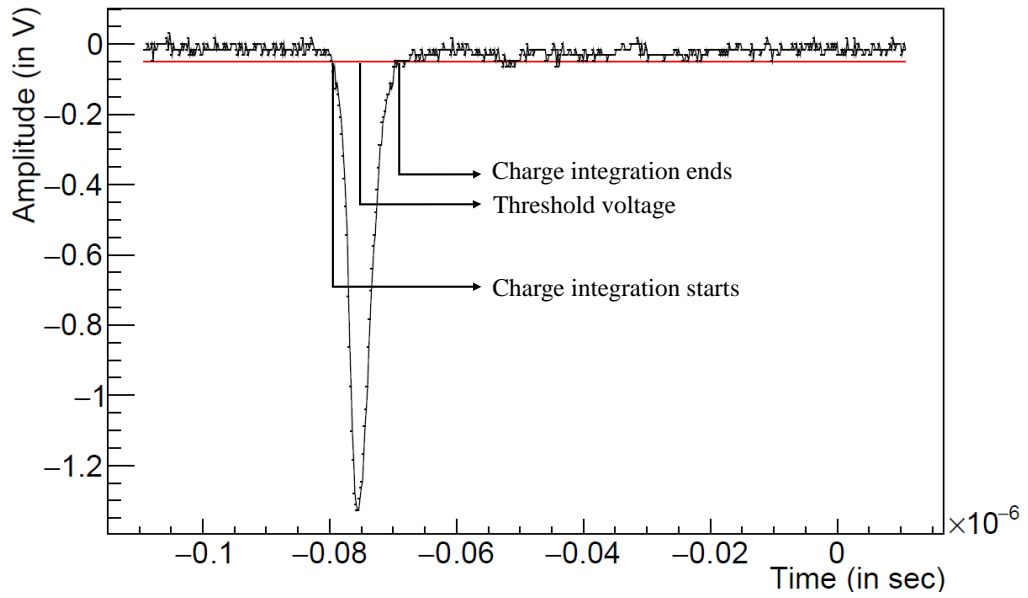
Figure 6.10: Charge integration procedure.

fitted with polya distribution and the mean has been considered as the average
induced charge for the respective voltage as shown in figures 6.11(a) and 6.11(b)
where the fitting has been illustrated with a red line. The error of most probable
value has been taken as the error of the average charge. The average induced
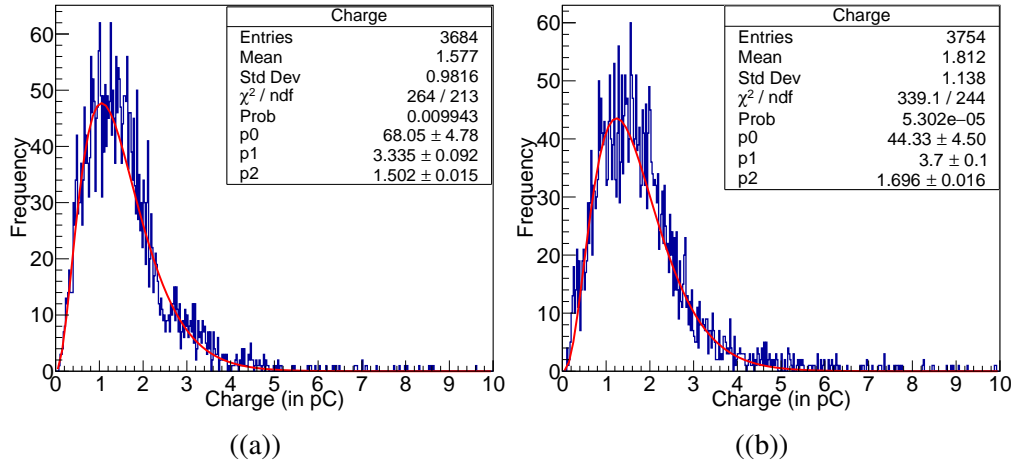
Figure 6.11: Distribution of induced charge for a) 10 kV and b) 10.2 kV.

charge in the RPC as function of high voltage is shown in figure 6.12 where it can be seen that the amount of average charge exceeds beyond 3 pC from 10.5 kV onward. Therefore, the voltage region below 10.5 kV can be safely used for avalanche mode operation of the RPC.
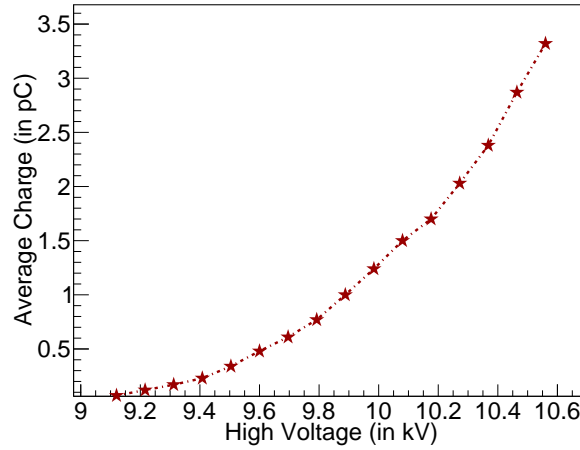
Figure 6.12: Average induced charge as function of high-voltage.

In figure 6.13 The experimental results of the RPC efficiency have been compared with the calculated one obtained from the numerical simulation following

the process described in chapter 5. All the simulations have been carried out
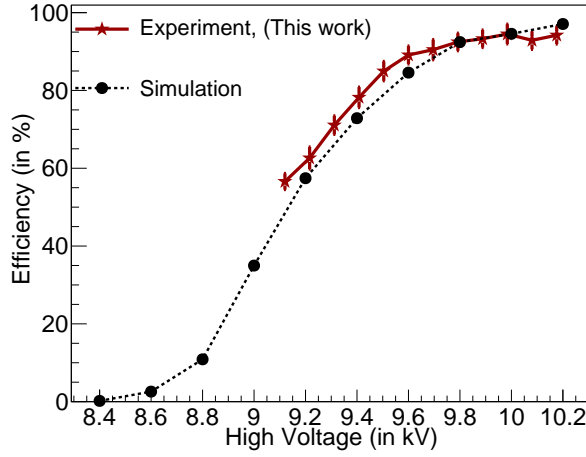
Figure 6.13: Comparison of efficiency between experiment and simulation as function of high-voltage.

assuming 1% relative tolerance while solving the hydrodynamic and electrostatic equations. The error in efficiency measured from experiment is the same as shown in figure 6.7. The plot shows a close agreement between the measurement and simulation for the RPC operation. Figure 6.14 illustrates the streamer probability as function of efficiency as obtained from the experiment and the numerical calculation. The error in experimentally measured streamer probability has been calculated assuming Poissonian error in counting of streamer events and number of triggers. At lower streamer probability, the error is as high as 50% because of very low count of streamer events. But at higher streamer probability, the error is around 2%. It also shows a close agreement between them, with the experimental streamer probability always little less than the calculated one.

In this chapter, the procedure of measuring a few performance parameters of a glass RPC has been described following its fabrication and testing. The measurements have been compared to the values as can be predicted from the
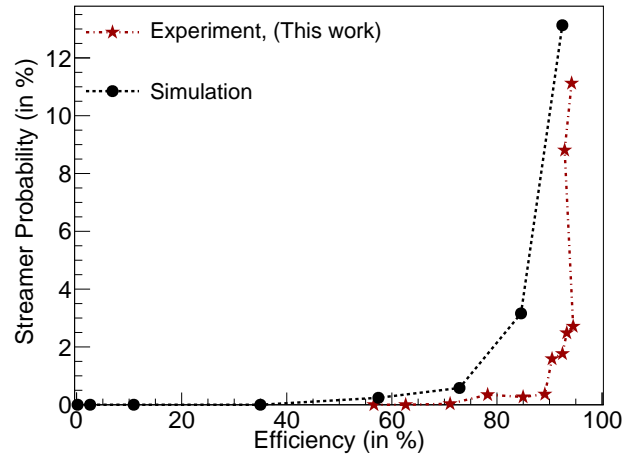
Figure 6.14: Comparison of streamer probability between experiment and simulation as function of high-voltage.

numerical simulation of the RPC dynamics following hydrodynamic approach. A close agreement between the experiment and simulation has implied that the hydrodynamic model devised for the RPC is reasonably successful in emulating its working procedure. The finding has prompted utilization of the numerical model in exploring new gas mixtures and their feasibility for operating the RPCs of the ICAL in avalanche mode in order to address the environmental issues of the present

Numerical Qualification of Eco-Friendly Gas Mixture

The need for eco-friendly RPC operation in INO-ICAL has motivated the investigation for an alternate feasible gas mixture. In this context, the numerical model, described in the chapter 5, has been used to numerically qualify such a mixture. It has been shown in chapters 5 and 6 that the model can emulate the working mode of the RPC at different applied voltages for a given filling gas mixture, from which its efficiency and the streamer probability can be estimated. In this chapter the ability of the numerical model in simulating the charge evolution reliably has been utilized to test an alternative gas mixture which needs to be eco-friendly, non-flammable, economical for operating 28,800 RPCs of ICAL in avalanche mode over a long period of time. It is important to predict their efficiency and the streamer probability as figures of merit to plan and design the experimental accessories. In the following, a brief discussion on the gas studies will be provided first to justify the choice of gas components to propose a new

mixture. Later the simulated performance of the RPC for the proposed mixture
will be presented and compared to the simulated values of the same observable
for a standard mixture of R134a (95.2%):i-C_4H_{10} (4.5%):SF_6 (0.3%) to demon-
strate the merits and demerits of the new mixture. It should be noted that the
simulated RPC responses for the standard R134a-based mixture have shown a
close agreement with the experimental measurements as discussed in chapter
6. The same will be done for other potential eco-friendly Hydro-Fluoro-Olefin
(HFO)-based gas mixtures too.

7.1   Choice of Gas Mixture

Extensive studies on various gases and their properties in order to find suitable
substitutes for operating RPCs in many other high energy physics experiments
[106, 107, 112, 113, 114, 115, 116] have been carried out. According to these
studies, one allotropic form of tetrafluoropropene, $C_3H_2F_4$ (commercially known
as HFO1234ze) which is close to R134a in chemical structure, with very low
GWP (~ 6), can be regarded as a potential replacement. However, the HFO1234ze
shows lower effective Townsend coefficient with respect to that of R134a when
compared at the same electric field. As a consequence, comparatively higher
electric field is required to achieve an efficiency of about 90%. A few promising
mixtures based on HFO1234ze, i-C_4H_{10} and He or CO_2 could be identified with
low GWP (< 150) [112, 116] for efficient operation of RPC, though the high
voltage requirement of some of them [116] might not be compatible to ICAL
high voltage supply system [117]. Moreover, these mixtures have shown presence
of substantially large fraction of streamers [112, 116] at higher efficiency, which

is well above the tolerable limit for safe and long term operation. As a result, inclusion of small amount of electron quencher gas SF_6 ($\sim 1\%$) in the mixtures could not be ruled out for efficient operation of the detectors, which has led the effective GWP sometimes cross the limit of 150 [106, 107, 112, 115]. Other than this, HFO1234ze has one more disadvantage regarding its use in RPC, considering the criticism about its degrading effect on the detector health. It has low GWP, essentially because of its smaller lifetime in the environment. The rate of dissociation of the gas in presence of OH^- radical (produced from dissociation of water molecule) is four times faster than that of R134a [118]. The final products are HF and other corrosive acids, which can destroy the surface of the RPC electrodes. For neutrino experiments which will operate for long time, consistent detector performance and in turn good health of the detector is an important requirement.

In this doctoral study, a gas mixture of Ar, CO_2 and N_2 in volume percentage of 5:60:35 has been proposed as a new alternative for avalanche mode operation of RPCs. It should be noted that all the components other than CO_2 (GWP = 1) are green (GWP = 0) and commercially available economical gases. The argon has been taken as the principal component for ionization. Its high Townsend coefficient at low electric field will help to reduce the operating voltage of RPCs. On the other hand, it will lead to large streamer probability at higher fields. To circumvent the issue of streamer, the partial volume of the Ar has been reduced by introducing N_2 which is highly electronegative and chemically less reactive. As a photon quencher, CO_2 has been preferred over other alternatives as it has less penning transfer coefficient in a mixture with Ar [119] and less GWP [114]. Its non-flammability and cheap cost are the added advantages.

To study the performance of the proposed Ar-based gas mixture, a comparison of its transport parameters to that of the standard R134a-based gas mixture has been made with the help of MAGBOLTZ. The effect of adding a small amount of SF_6 (0.5%), a widely used electron quencher, to the new mixture has been studied as well. The results of the effective Townsend coefficient and drift velocity as a function of the applied electric field for all these gas mixtures have been plotted in figures 7.1 and 7.2. It should be noted that the pressure and temperature have been kept at 1 bar and 293.15 K, respectively, throughout the numerical work, same to that of the standard R134a-based gas mixture. For simulations of the Ar-based gas mixtures, the penning transfer coefficient has been included following [120, 121]. It is obvious from the plot shown in figure 7.1 that the proposed Ar-based gas mixture has closely followed the standard R-134-based one in the case of effective Townsend coefficient, which indicates similar Townsend multiplication of electrons in both the mixtures. The comparison of drift velocity, as depicted in figure 7.2, shows that the proposed Ar-based mixture is faster by a factor of 2 than the standard R134a-based one. However, the mean primary cluster size is smaller in it by a factor of 3 in comparison to that of the standard R134a-based mixture as calculated from HEED and shown in figure 7.3. According to Ramo's theorem [90], the induced current at an instant *t* on the RPC readout can be determined following the equation 5.12. It follows from the expression that the higher drift velocity of the new mixture has compensated the lack of primary electrons which determines the total number of electrons, n_e, for a given Townsend multiplication. It implies that the current signal produced with the proposed Ar-based mixture should be comparable with that obtained using the standard R134a-based mixture. It should also be noted that the addition of SF_6
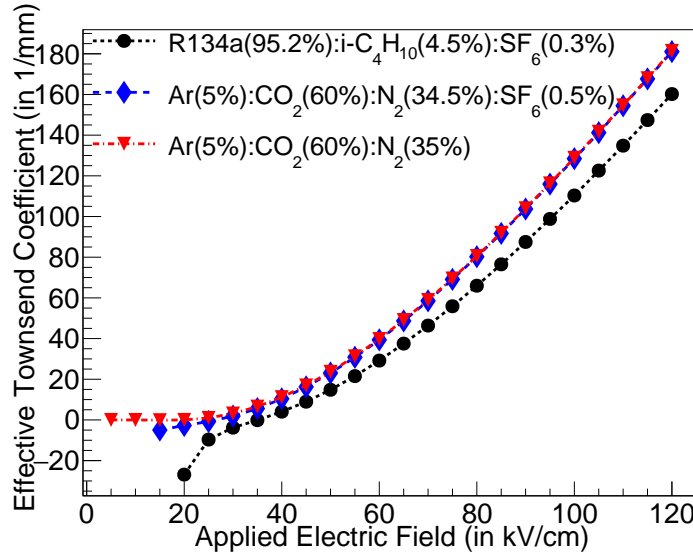
Figure 7.1: Comparison of effective Townsend coefficient as a function of applied voltage of proposed Ar (5%):CO$_2$ (60%):N$_2$ (35%) and Ar (5%):CO$_2$ (60%):N$_2$ (34.5%):SF$_6$ (0.5%) mixture to that of R134a (95.2%):i-C$_4$H$_{10}$ (4.5%):SF$_6$ (0.3%) as obtained from MAGBOLTZ [104].

to the proposed gas does not alter the transport properties significantly.

7.2 Qualification of Ar(5%):CO$_2$(60%):N$_2$(35%)

To qualify the proposed Ar(5%):CO$_2$:(60%):N$_2$(35%) mixture, the efficiency and streamer probability as the figures of merit have been estimated from the numerical simulation data. In this section, the results will be discussed along with their comparison to the standard R134a-based gas mixture. Next, the same results will be compared to the experimental data of other potential HFO1234ze-based gas mixtures [116, 112].

The 2D histogram of the primary clusters for the gas mixture Ar(5%):CO$_2$ (60%):N$_2$(35%) has been shown in figure 7.4 as produced from the HEED data. In this case, it has been observed that for 90% events, the cluster size has varied
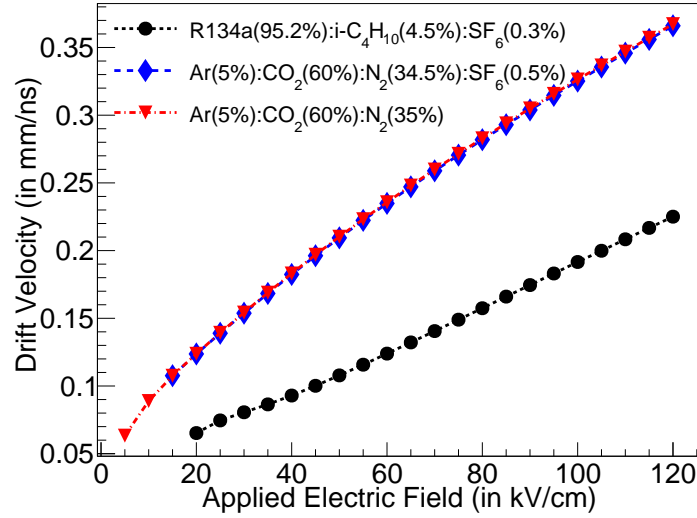
Figure 7.2: Comparison of drift velocity as a function of applied voltage of proposed Ar (5%):CO_2 (60%):N_2 (35%) and Ar (5%):CO_2 (60%):N_2 (34.5%):SF_6 (0.5%) mixture to that of R134a (95.2%):i-C_4H_{10} (4.5%):SF_6 (0.3%) as obtained from MAGBOLTZ [104].

between 2 and 25 and so a smaller bin size of 1 has been used in the histogram for the cluster size while keeping the bin size for mean Z-position same as the standard R134a-based gas mixture shown in chapter 5. Following the convention described in chapter 5, the number in each bin denotes the number of events falling in that group.

7.2.1   Comparison with R134a-based Mixture

Efficiency and streamer probability of the proposed Ar-based mixture with variation of applied voltage have been depicted in figure 7.5. It has been observed that the streamer probability has shot up much beyond 20% when the efficiency has hardly reached 85%. It has been noted that this problem can be alleviated in two ways. The first option is to reduce the streamer probability by addition of very
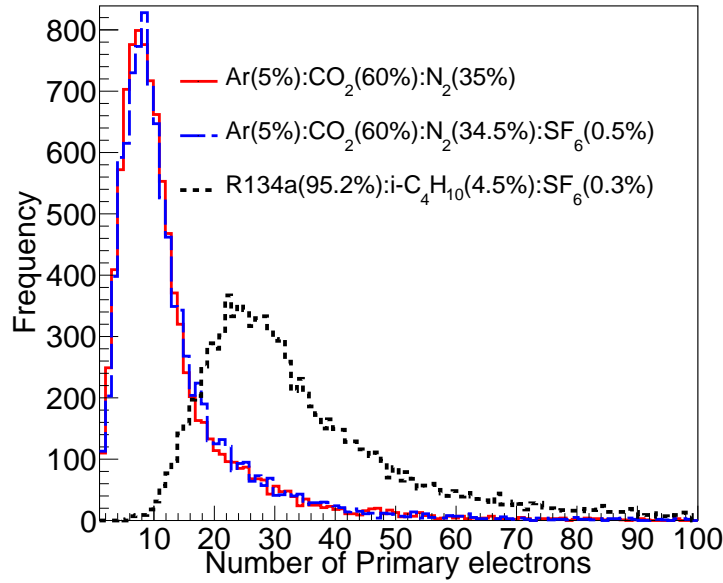
Figure 7.3: Comparison of primary electron number of proposed Ar (5%):CO$_2$ (60%):N$_2$ (35%) and Ar (5%):CO$_2$ (60%):N$_2$ (34.5%):SF$_6$ (0.5%) mixture to that of R134a (95.2%):i-C$_4$H$_{10}$ (4.5%):SF$_6$ (0.3%) as obtained from HEED [103]. The values have been calculated assuming the gas temperature is 293.15K and pressure 1 bar.

small amount of electronegative SF$_6$ as practiced in case of the standard R134a-based mixture. Nevertheless, this option should not be very much effective, as implied by the plot shown in figure 7.1. The GWP of the Ar-based mixture will be within the limit of 150 if SF$_6$ is added by a percentage of less than 0.5%. The other option is to reduce the threshold for valid event to increase the ratio of the avalanche events to the streamer one, which will obviously allow some noise eventually. Both the options have been studied, and the expected improvement has been observed in both the cases. The effect of adding 0.5% of SF$_6$ in the mixture has been depicted in figure 7.6(a) where the efficiency of the mixture with and without the SF$_6$ component has been compared to that of the standard mixture. It can be noted from the figure that the operation in avalanche mode with
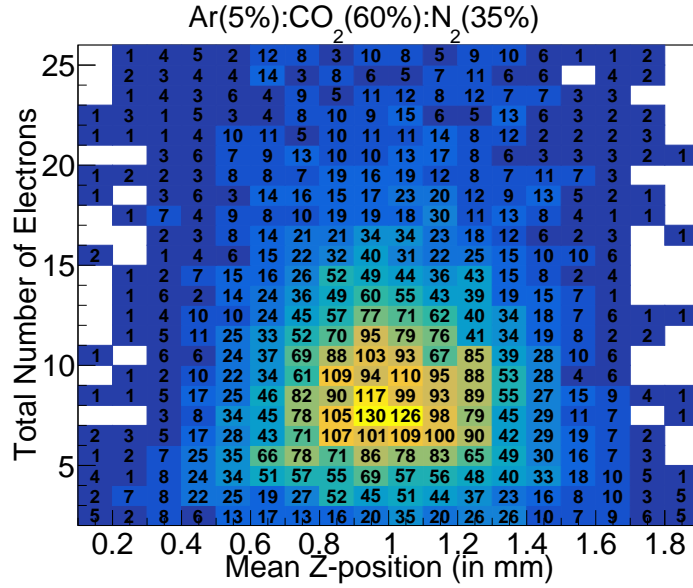
Figure 7.4: 2D histogram of muon events for the gas mixture of Ar(5%):CO_2 (60%):N_2(35%).

the Ar-based mixture is not practically feasible beyond 80-85% efficiency. The addition of SF_6 component in the mixture has reduced the streamer probability by 40% at this efficiency range, although it is still higher in comparison to the standard R134a-based mixture. The results of reducing the threshold from 5 mV to 1 mV have been depicted in figure 7.6(b) where an overall reduction in the streamer probability of the Ar-based mixture is visible. This approach can lead to an acceptable streamer probability (< 10%) around 85% efficiency, which is comparable to that of the standard R134a-based mixture. It can be noted that by reducing the threshold, the present Ar-based mixture can operate efficiently with low streamer probability even without the SF_6 component.
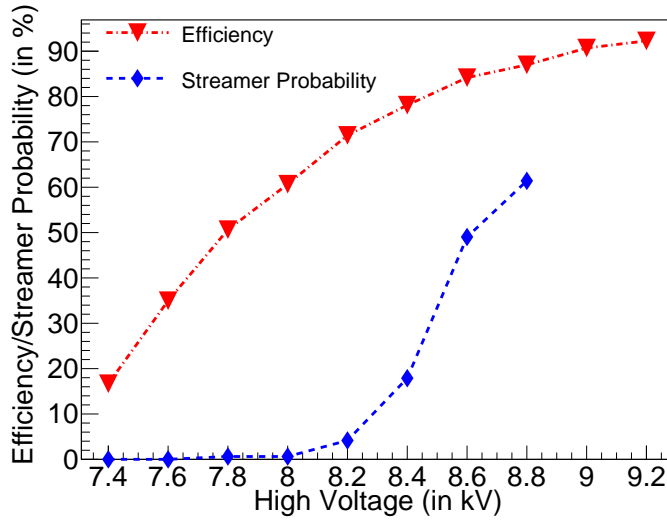
Figure 7.5: Simulated streamer probability and efficiency as functions of the applied high-voltage for Ar (5%):CO$_2$ (60%):N$_2$ (35%) with threshold of 5 mV.

| ((a)) | ((b)) |
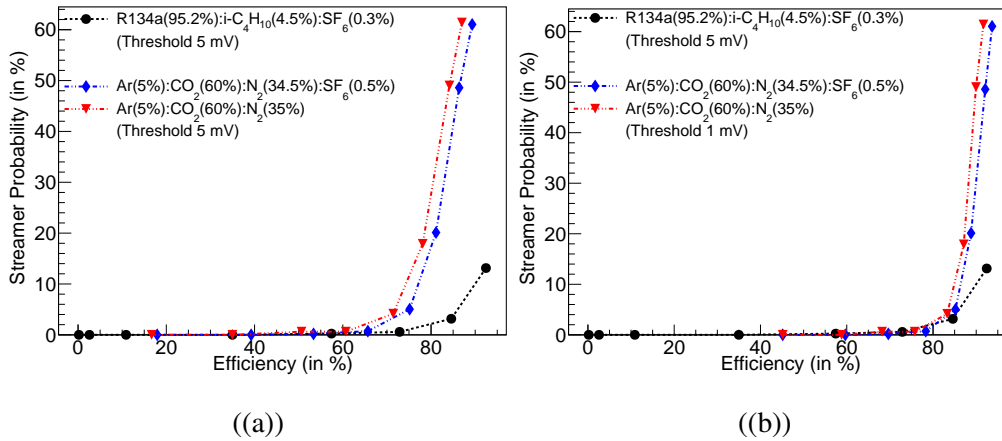
Figure 7.6: Comparison of streamer probability as function of efficiency among R134a (95.2%):i-C$_4$H$_1$0 (4.5%):SF$_6$ (0.3%), Ar (5%):CO$_2$ (60%):N$_2$ (35%) and Ar (5%):CO$_2$ (60%):N$_2$ (34.5%):SF$_6$ (0.5%) mixtures (a) for 5 mV threshold (b) for 1 mV threshold.

7.2.2 Comparison with HFO1234ze-based Mixtures

The proposed Ar-based gas mixture has been compared for its performance with other potential eco-friendly mixtures proposed earlier by others [112, 116] in

figure 7.7. The gas mixtures used for the comparison are given in the following

table 7.1. In figures 7.7(a) and 7.7(b), the simulated streamer probability as a

Simulation/Experiment	Gas Mixture	Denoted as
Simulation	Ar (5%):CO_2 (60%):N_2 (35%)	Gas Mixture I
(This work)	Ar (5%):CO_2 (60%):N_2 (34.5%):SF_6(0.5%)	Gas Mixture II
Experiment	HFO1234ze(55%):CO_2(45%)	Gas Mixture III
by Bianchi et al. [116]	HFO1234ze(%50):CO_2(49%):SF_6(1%)	Gas Mixture IV
Experiment	HFO1234ze(55%):i-C_4H_{10}(5%):He(40%)	Gas Mixture V
by Abbrescia et al. [112]	HFO1234ze(54%):i-C_4H_{10}(3.7%) :He(41%):SF_6(1.3%)	Gas Mixture VI

Table 7.1: Different eco-friendly gas mixtures compared in this work based on their efficiency and streamer probability.

function of efficiency for the proposed Ar-based gas mixtures (with and without SF_6) for two threshold values of 5 mV and 1 mV, respectively, has been compared to the measured data for other mixtures based on HFO1234ze, CO_2 and SF_6 as the third component [116]. It can be seen from figure 7.7(a) that the proposed Ar(5%):CO_2(60%):N_2(34.5%) mixture with SF_6(0.5%) has shown streamer probability of about 20% around 80-85% efficiency which is comparable to that of the HFO1234ze(55%):CO_2(45%). However, the HFO1234ze-based mixture with 1% of SF_6 has shown better performance as the streamer probability remains below 10% when the efficiency is around 85-90%. It can be found from the plot shown in figure 7.7(b) that the proposed Ar-based mixture (even without SF_6 component) can produce similar performance when the threshold is reduced to 1 mV.

The proposed Ar-based mixture has also been compared for its performance with another promising mixture which is composed of HFO1234ze, He, i-C_4H_{10} and SF_6 as the optional component [112]. The simulated streamer probability of

the Ar-based mixtures as a function of the efficiency has been plotted with the measured values for the said HFO1234ze-based mixtures in figures 7.7(c) and 7.7(d). It can be followed from the plots that the reduction in the threshold has improved the performance of the present Ar-based gas mixture (even without the SF$_6$) significantly with respect to the HFO1234ze-based mixture when considered without the SF$_6$ component around the efficiency of 80-85%. The additional advantage of using the proposed Ar-based mixture is that the operating voltage for the proposed mixture is quite low with respect to that of the HFO1234ze-based mixtures, as shown in 7.8(a) and 7.8(b). Following the discussion, it should be noted that the proposed gas mixture of Ar(5%):CO$_2$(60%):N$_2$(35%) has been found to be a potential substitute of the standard R134a(95.2%):i-C$_4$H$_{10}$(4.5%):SF$_6$(0.3%) from the view point of its non-hazardous character and also the detector operation at lower voltages.
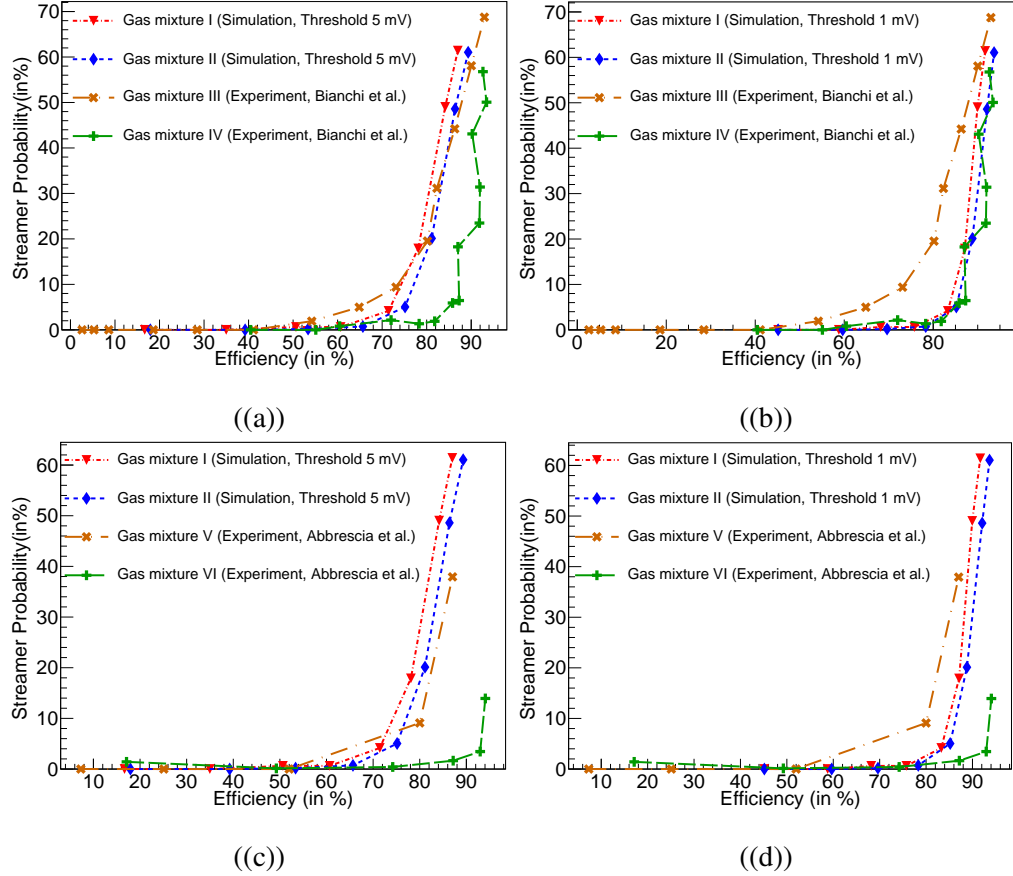
Figure 7.7: Comparison of efficiency versus streamer probability of the proposed gas mixtures to other alternative gas mixtures. The top panel shows comparison with experimental data from Bianchi et al. [116]. The bottom panel shows comparison with the alternative gas proposed in Abbrescia et al. [112]. The left panel is comparison when the threshold in simulation has been set to 5 mV. The right panel shows comparison when the threshold is reduced to 1 mV.
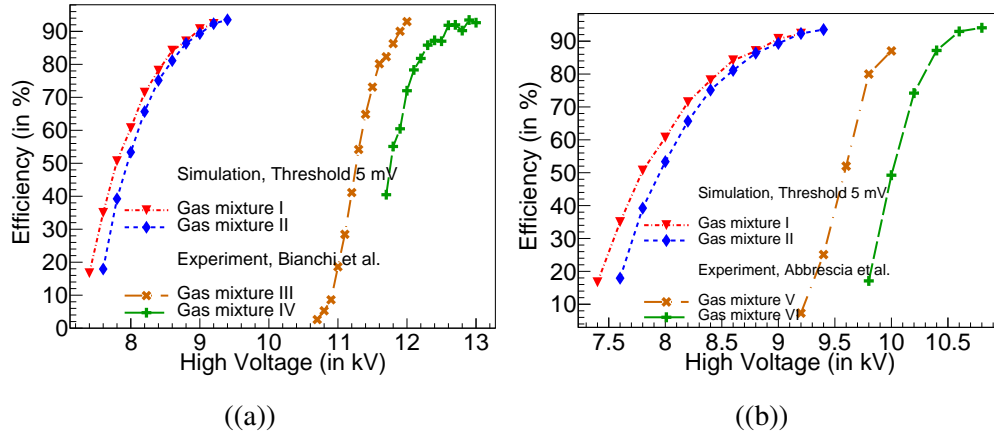
Figure 7.8: Comparison of efficiency as function of high-voltage among the proposed gas mixtures in this work with other alternative gas mixtures [112, 116]. The gas mixtures are denoted as described in table 7.1.

Neutrino Oscillations in Vacuum

and in Matter

The signature of non-zero mass of neutrino was established with the discovery of the neutrino oscillation phenomena. The SM neutrinos have zero mass, so these phenomena is a direct proof of the physics beyond SM. This chapter will describe these phenomena and discuss the implications of different results. With the LEP experiment, it was established that the number of light neutrino family is exactly three. So it was evident that the all these three families interact through weak interaction. Each of the families is called a flavor, and the states are called flavor states. Following the $K^\circ \leftrightarrow \bar{K}^\circ$ oscillation, Pontecorvo first proposed the $\nu \leftrightarrow \bar{\nu}$ oscillation. At that time, only the existence of ν_e was established. Later, Maki-Nakagawa-Sakata proposed an oscillation framework where the weak interaction flavor states are linear superposition of the mass eigenstates. The basic idea of this framework is that the neutrinos have mass and the flavor states do not overlap with mass eigenstates. Following this idea, many contributed to formalize the

neutrino oscillation picture. At that time the ν_τ was yet to be discovered, and in the absence of ν_τ initially the oscillation framework was built for two flavors, ν_e, ν_μ.

8.1 Neutrino oscillation in vacuum

8.1.1 Two Flavor Oscillation

In this formalism it is assumed that there are two mass eigenstates namely ν_1, ν_2 with mass m_1 and m_2 respectively. The flavor states are ν_e and ν_μ. The relation between flavor and mass eigenstates can be expressed with the following equation

$$\begin{bmatrix} \nu_e \\ \nu_\mu \end{bmatrix} = \begin{bmatrix} \cos\theta & \sin\theta \\ -\sin\theta & \cos\theta \end{bmatrix} \begin{bmatrix} \nu_1 \\ \nu_2 \end{bmatrix} \tag{8.1}$$

Now let's assume in an interaction the created neutrino is ν_e. So at time t = 0, the neutrino state $|\nu\rangle$ can be expressed as

$$|\nu(0)\rangle = |\nu_e\rangle = \cos\theta\,|\nu_1(0)\rangle + \sin\theta\,|\nu_2(0)\rangle \tag{8.2}$$

The time evolved neutrino state at t = t can be expressed using the following equation,

$$|\nu(t)\rangle = \cos\theta\,|\nu_1(0)\rangle\,e^{-iE_1 t} + \sin\theta\,|\nu_2(0)\rangle\,e^{-iE_2 t} \tag{8.3}$$

where E_1 and E_2 are the energy of the mass eigenstates. So the projection of the time evolved state on $|\nu_e\rangle$ can be expressed as

$$\langle\nu_e|\nu(t)\rangle = \cos\theta\,\langle\nu_e|\nu_1(0)\rangle\,e^{-iE_1 t} + \sin\theta\,\langle\nu_e|\nu_2(0)\rangle\,e^{-iE_2 t}$$
$$= \cos^2\theta e^{-iE_1 t} + \sin^2\theta e^{-iE_2 t} \tag{8.4}$$

and the same on ν_μ can be expressed as

$$\langle \nu_\mu | \nu(t) \rangle = \cos\theta \, \langle \nu_\mu | \nu_1(0) \rangle \, e^{-iE_1 t} + \sin\theta \, \langle \nu_\mu | \nu_2(0) \rangle \, e^{-iE_2 t}$$

$$= \cos\theta \sin\theta (e^{-iE_2 t} - e^{-iE_1 t}) \tag{8.5}$$

So the probability of observing ν_μ after time t is

$$= |\langle \nu_\mu | \nu(t) \rangle|^2$$

$$= \sin^2 2\theta \sin^2 \left(\frac{(E_2 - E_1)t}{2} \right) \tag{8.6}$$

Now the energy of the mass eigenstates are $E_i = \sqrt{p_i^2 + m_i^2}$, p_i and m_i is momentum and mass of the ith eigenstate. The neutrinos are ultra relativistic and their mass is negligible. So the energy of the mass eigenstates can be approximated as $E_i = p_i + \frac{m_i^2}{2p_i}$. The two mass eigenstate in principal can have different momenta, but it can be shown that approximating the momentum of the two states to be equal leaves the expression of the probability to be qualitatively the same. So one can approximate that the momentum of the neutrino, $p = p_1 = p_2$. We can neglect the mass of neutrino with respect to the momentum, which implies that $E = p$. With this, one can write $(E_2 - E_1) = \frac{m_2^2 - m_1^2}{2E} = \frac{\Delta}{2E}$. As the neutrinos are ultra relativistic we can write $t = \frac{L}{c} \sim L$, where 'L' is the distance between the source and the detector and 'c' is the velocity of the neutrinos which is nearly equal to the velocity of light in vacuum. So the probability of observing ν_μ after time t when the initial state has been ν_e can be expressed as

$$P_{e\mu} = \sin^2 2\theta \sin^2 \left(\frac{\Delta L}{4E} \right) \tag{8.7}$$

From the conservation of probability one can write the probability of observing the neutrino as ν_e is

$$P_{ee} = 1 - \sin^2 2\theta \sin^2 \left(\frac{\Delta L}{4E} \right) \tag{8.8}$$

From the equation 8.7 it can be said that to observe the neutrino oscillation the mass of the different mass eigenstates cannot be the same, and the angle θ has to be non-zero. The period of this oscillation is dependent on the factor $\frac{\Delta}{2E}$, which is related to the oscillation length $L_{osc} = 4\pi E/\Delta$

8.1.2   Three Flavor Oscillation

After the discovery of ν_τ the three flavor, oscillation became important. The three flavor oscillation is nothing but an extension of the two flavor oscillation formalism. In this scenario, the number of flavor and mass eigenstates are both three. Which leads to a 3×3 unitary matrix to express the linear super position between these two eigenbasis. The three mass eigenstates, ν_1, ν_2 and ν_3 have masses m_1, m_2 and m_3 respectively. The 3×3 unitary matrix denoted as 'U' is known as PMNS matrix and the relation between these states can be expressed as the following

$$
\begin{bmatrix} \nu_e \\ \nu_\mu \\ \nu_\tau \end{bmatrix} = U \begin{bmatrix} \nu_1 \\ \nu_2 \\ \nu_3 \end{bmatrix}
$$
$$
= \begin{bmatrix} U_{e1} & U_{e2} & U_{e3} \\ U_{\mu1} & U_{\mu2} & U_{\mu3} \\ U_{\tau1} & U_{\tau2} & U_{\tau3} \end{bmatrix} \begin{bmatrix} \nu_1 \\ \nu_2 \\ \nu_3 \end{bmatrix},
$$

(8.9)

with the matrix U parameterized in the following way

$$U(\theta_{13},\ \theta_{23},\ \theta_{12},\ \delta_{CP}) = O_{23}(\theta_{23})U_{13}(\theta_{13},\delta_{CP})O_{12}(\theta_{12})$$

$$= \begin{bmatrix} 1 & 0 & 0 \\ 0 & \cos\theta_{23} & \sin\theta_{23} \\ 0 & -\sin\theta_{23} & \cos\theta_{23} \end{bmatrix} \begin{bmatrix} \cos\theta_{13} & 0 & \sin\theta_{13}e^{-i\delta_{CP}} \\ 0 & 1 & 0 \\ -\sin\theta_{13}e^{i\delta_{CP}} & 0 & \cos\theta_{13} \end{bmatrix} \begin{bmatrix} \cos\theta_{12} & \sin\theta_{12} & 0 \\ -\sin\theta_{12} & \cos\theta_{12} & 0 \\ 0 & 0 & 1 \end{bmatrix}.$$

$$(8.10)$$

In equation 8.10, the parameter δ_{CP} denotes the CP violating phase.

A 2×2 unitary matrix needs 4 parameters to parameterize. Out of which one is the mixing angle and the other three are the phases. But the phases can be pulled out and absorbed in the definition of the neutrino fields. This leaves only one mixing angle to parameterize the unitary matrix in case of two flavor oscillation. In case of a 3×3 unitary matrix, 9 parameters are needed for parameterization. Out of the nine parameters, there are three mixing angles,θ_{ij} as shown in 8.10. The rest six are phases. Out of the six phases, five phases can be pulled out, and the sixth one is the phase denoted by δ_{CP}. Out of the five phases, three can be pulled out and absorbed in the in neutrino flavor eigenstates and the rest two can be absorbed in the mass eigenstates. If neutrinos are Dirac particles, only δ_{CP} can be measured through experiments. But in case when neutrinos are Majorana particle, the phases absorbed in the mass eigenstates are also observable.

The calculation of oscillation probabilities is similar to that of the 2 flavor oscillation. Following the same procedure, the oscillation probability from ν_α to

ν_β can be written as

$$P(\nu_\alpha \to \nu_\beta) = P_{\alpha\beta} = \delta_{\alpha\beta} - 4 \sum_{i>j} Re\left(U_{\alpha i}^* U_{\beta i} U_{\alpha j} U_{\beta j}^*\right) \sin^2\left(\frac{\Delta_{ij}L}{4E}\right)$$
$$+ 2 \sum_{i>j} Im\left(U_{\alpha i}^* U_{\beta i} U_{\alpha j} U_{\beta j}^*\right) \sin^2\left(\frac{\Delta_{ij}L}{2E}\right). \quad (8.11)$$

If $\alpha = \beta$, $P_{\alpha\beta}$ denotes the survival probability otherwise it stands for oscillation probability. The oscillation probability for the anti-neutrinos can be expressed using the following formula,

$$P(\bar{\nu}_\alpha \to \bar{\nu}_\beta) = P_{\bar{\alpha}\bar{\beta}} = \delta_{\alpha\beta} - 4 \sum_{i>j} Re\left(U_{\alpha i}^* U_{\beta i} U_{\alpha j} U_{\beta j}^*\right) \sin^2\left(\frac{\Delta_{ij}L}{4E}\right)$$
$$- 2 \sum_{i>j} Im\left(U_{\alpha i}^* U_{\beta i} U_{\alpha j} U_{\beta j}^*\right) \sin^2\left(\frac{\Delta_{ij}L}{2E}\right). \quad (8.12)$$

With these one can find the oscillation and survival probability of the neutrinos given the energy and the path length it traverses after production. But these are valid only when the neutrinos are traversing through vacuum. The presence of matter modifies these expressions. This will be discussed in the following sections.

8.2   Neutrino oscillation in matter

The mediator bosons for weak interaction are of three kinds: $W^\pm$ and Z°. The interactions mediated by the bosons $W^\pm$ are known as charge current (CC) interaction and the interactions mediated by Z° are known as neutral current (NC) interactions. All the three flavors of neutrinos participate in both these interactions. These interactions lead to a potential for the neutrinos, which changes the dispersion relation for the neutrinos to $E = \sqrt{p^2 + m^2} + V$. In the earlier

sections, it has been established that neutrino propagation is dependent on the differing propagation properties of the neutrino mass eigenstates. This makes it evident that the presence of this potential will modify the neutrino oscillation probabilities.

8.2.1 Effective matter potential

The CC interactions of the neutrinos and the anti-neutrinos in matter are as following

$$\nu_e + n \rightarrow p + e^-, \quad \bar{\nu}_e + p \rightarrow n + e^+$$

$$\nu_\mu + n \rightarrow p + \mu^-, \quad \bar{\nu}_\mu + p \rightarrow n + \mu^+$$

$$\nu_\tau + n \rightarrow p + \tau^-, \quad \bar{\nu}_\tau + p \rightarrow n + \tau^+,$$

and the NC interactions of the neutrinos and anti-neutrinos in matter are following

$$\nu_e + e^- \rightarrow \nu_e + e^-, \quad \bar{\nu}_e + e^- \rightarrow \bar{\nu}_e + e^-$$

$$\nu_\mu + e^- \rightarrow \nu_\mu + e^-, \quad \bar{\nu}_\mu + e^- \rightarrow \bar{\nu}_\mu + e^-$$

$$\nu_\tau + e^- \rightarrow \nu_\tau + e^-, \quad \bar{\nu}_\tau + e^- \rightarrow \bar{\nu}_\tau + e^-$$

Along with these interactions, ν_e goes under forward coherent scattering with the electrons present in the material, mediated by W^+ bosons. This interaction incorporates an extra potential for the electron neutrinos. So, for two flavor scenarios, the potential in flavor basis can be written as following

$$V = \begin{bmatrix} V_{CC} + V_{NC} & 0 \\ 0 & V_{NC} \end{bmatrix}$$

$$= V_{NC} I + \begin{bmatrix} V_{CC} & 0 \\ 0 & 0 \end{bmatrix}, \tag{8.13}$$

where I is a 2×2 identity matrix. As the NC interaction for ν_e and ν_μ is same, the potential term V_{NC} is same for both the flavors and proportional to identity matrix. So, this term will be proportional to the identity matrix even in the mass eigenbasis, and will not come up in oscillation probability expressions. This leaves us with an effective potential, and we can drop the first term of the equation 8.13.

8.2.2 Two flavor neutrino oscillation in matter

In vacuum, the propagation equation for two flavor scenario is

$$
i\frac{d}{dt}\begin{bmatrix} \nu_1 \\ \nu_2 \end{bmatrix} = \left(p + \frac{m_1^2 + m_2^2}{4E} \right) I + \frac{1}{4E}\begin{bmatrix} -\Delta & 0 \\ 0 & \Delta \end{bmatrix}\begin{bmatrix} \nu_1 \\ \nu_2 \end{bmatrix} \tag{8.14}
$$

where $\Delta = m_2^2 - m_1^2$. As mass eigenstates of neutrinos do not take part in weak interaction, so, to add the potential term to this equation we have to change to flavor eigenbasis. Following the equation 8.1

$$
i\frac{d}{dt}\begin{bmatrix} \cos\theta & -\sin\theta \\ \sin\theta & \cos\theta \end{bmatrix}\begin{bmatrix} \nu_e \\ \nu_\mu \end{bmatrix} = \frac{1}{4E}\begin{bmatrix} -\Delta & 0 \\ 0 & \Delta \end{bmatrix}\begin{bmatrix} \cos\theta & -\sin\theta \\ \sin\theta & \cos\theta \end{bmatrix}\begin{bmatrix} \nu_e \\ \nu_\mu \end{bmatrix}
$$

$$
i\frac{d}{dt}\begin{bmatrix} \nu_e \\ \nu_\mu \end{bmatrix} = \frac{1}{4E}\begin{bmatrix} -\Delta\cos 2\theta & \Delta\sin 2\theta \\ \Delta\sin 2\theta & \Delta\cos 2\theta \end{bmatrix}\begin{bmatrix} \nu_e \\ \nu_\mu \end{bmatrix}
$$

$$
\tag{8.15}
$$

where in the last step we have dropped the terms proportional to the identity matrix, I, as it will not contribute to the oscillation probability expressions. Now

adding the potential term $\begin{bmatrix} V_{CC} & 0 \\ 0 & 0 \end{bmatrix}$ to the equation 8.10 we get

$$i\frac{d}{dt}\begin{bmatrix} \nu_e \\ \nu_\mu \end{bmatrix} = \frac{1}{4E}\begin{bmatrix} -\Delta\cos 2\theta + A & \Delta\sin 2\theta \\ \Delta\sin 2\theta & \Delta\cos 2\theta - A \end{bmatrix}\begin{bmatrix} \nu_e \\ \nu_\mu \end{bmatrix} \tag{8.16}$$

where $A = 2EV_{CC}$ is called Wolfenstein matter term. From electroweak model, this term becomes

$$A = 2\sqrt{2}G_F N_e E \tag{8.17}$$

with G_F is Fermi constant of weak interaction and N_e is the electron density in matter. Substituting the values of the constants we get

$$A = 0.76 \times 10^{-4}\rho(in\ g/cc)E(in\ GeV)$$

To diagonalize the effective mass-square matrix represented in mass eigenbasis 8.16

$$M^2 = \begin{bmatrix} -\Delta\cos 2\theta + A & \Delta\sin 2\theta \\ \Delta\sin 2\theta & \Delta\cos 2\theta - A \end{bmatrix} \tag{8.18}$$

we need an orthogonal matrix

$$O_m = \begin{bmatrix} \cos\theta^m & \sin\theta^m \\ -\sin\theta^m & \cos\theta^m \end{bmatrix} \tag{8.19}$$

where θ^m is the modified mixing angle. As $O_m^T M^2 O_m$ is orthogonal, we get that

$$\tan 2\theta^m = \frac{\Delta\sin 2\theta}{\Delta\cos 2\theta - A} \tag{8.20}$$

$$O_m^T M^2 O_m = \frac{1}{4E}\begin{bmatrix} -\Delta^m & 0 \\ 0 & \Delta^m \end{bmatrix} \tag{8.21}$$

$$\Delta^m = \sqrt{(\Delta\cos 2\theta - A)^2 + (\Delta\sin 2\theta)^2} \tag{8.22}$$

. Using these values and following the earlier method, the oscillation and survival probabilities are

$$P_{e\mu}^m = \sin^2 2\theta^m \sin^2 \left(\frac{\Delta^m L}{2E} \right) \tag{8.23}$$

$$P_{ee}^m = 1 - \sin^2 2\theta^m \sin^2 \left(\frac{\Delta^m L}{2E} \right) \tag{8.24}$$

The above equations 8.23,8.24 shows that the matter modified oscillation probabilities can be derived by replacing the mass square difference and the mixing angle with matter modified mass square difference and mixing angle in equation 8.7 and 8.8 respectively. These expressions are valid only in case of constant matter density, If the matter density changes from point to point one needs to take into account this variation in the density.

8.2.3 Three flavor neutrino oscillation in matter

In this section, we will discuss the matter effect on neutrino oscillation in three flavor paradigms. For three flavor, the Hamiltonian in mass eigenbasis is

$$H_{vacuum}^{mass} = \frac{1}{2E} \begin{bmatrix} m_1^2 & 0 & 0 \\ 0 & m_2^2 & 0 \\ 0 & 0 & m_3^2 \end{bmatrix} \tag{8.25}$$

where m_1, m_2 and m_3 denotes the mass of the three mass eigenstates, v_1, v_2 and v_3, respectively. The momentum part has been dropped in this expression following

the argument discussed in the earlier section. In flavor basis, the Hamiltonian is

$$H_{vacuum}^{flavor} = UH_{vacuum}^{mass}U^\dagger$$

$$= U\frac{1}{2E}\begin{bmatrix} m_1^2 & 0 & 0 \\ 0 & m_2^2 & 0 \\ 0 & 0 & m_3^2 \end{bmatrix}U^\dagger$$

$$= U\frac{1}{2E}\begin{bmatrix} 0 & 0 & 0 \\ 0 & \Delta_{21} & 0 \\ 0 & 0 & \Delta_{31} \end{bmatrix}U^\dagger$$

$$= UM^2U^\dagger$$

(8.26)

where Δ_{21} and Δ_{31} are the two independent mass square differences, $(m_2^2 - m_1^2)$ and $(m_3^2 - m_1^2)$ respectively. As shown in the earlier section, while propagation through matter, neutrinos pick up a phase. So the Hamiltonian in presence of matter is

$$H_{matter}^{flavor} = H_{vacuum}^{flavor} + V_{matter}^{flavor}$$

$$= \frac{1}{2E}(UM^2U^\dagger + \mathbf{A})$$

(8.27)

where

$$\mathbf{A} = \begin{bmatrix} A & 0 & 0 \\ 0 & 0 & 0 \\ 0 & 0 & 0 \end{bmatrix}$$

(8.28)

with $A = 2\sqrt{2}G_F N_e E$ as discussed in the earlier section. Following equation 8.10 the matrix U can be written in the following way

$$U(\theta_{13},\ \theta_{23},\ \theta_{12},\ \delta_{CP}) = O_{23}(\theta_{23})U_{13}(\theta_{13},\delta_{CP})O_{12}(\theta_{12})$$

$$= O_{23}(\theta_{23})U_{\delta_{CP}}(\delta_{CP})O_{13}(\theta_{13})U_{\delta_{CP}}^\dagger(\delta_{CP})O_{12}(\theta_{12})$$

(8.29)

where

$$
U_{\delta CP} = \begin{bmatrix} \exp^{i\delta_{CP}/2} & 0 & 0 \\ 0 & 1 & 0 \\ 0 & 0 & \exp^{-i\delta_{CP}/2} \end{bmatrix}
$$

. Form equation 8.28, we see that the 2-3 submatrix of $\mathbf{A}$ is null. So, we can write $\mathbf{A} = O_{23}(\theta_{23})U_{\delta CP}(\delta_{CP})\mathbf{A}U_{\delta CP}^{\dagger}(\delta_{CP})O_{23}^{T}(\theta_{23})$. So, the Hamiltonian H_{matter}^{flavor} can be written as

$$
H_{matter}^{flavor} = \frac{1}{2E}\left[U_1\left(U_2 M^2 U_2^{\dagger}\right)U_1^{\dagger}\right] \tag{8.30}
$$

where $U_1 = O_{23}(\theta_{23})U_{\delta CP}(\delta_{CP})$ and $U_2 = O_{13}(\theta_{13})U_{\delta CP}^{\dagger}(\delta_{CP})O_{12}(\theta_{12})$. Defining $M_{matter}^2 = U_2 M^2 U_2^{\dagger} + \mathbf{A}$, we get

$$
\begin{aligned}
M_{matter}^2 &= U_2 M^2 U_2^{\dagger} + \mathbf{A} \\
&= U_2 \begin{bmatrix} 0 & 0 & 0 \\ 0 & \Delta_{21} & 0 \\ 0 & 0 & \Delta_{31} \end{bmatrix} U_2^{\dagger} + \begin{bmatrix} A & 0 & 0 \\ 0 & 0 & 0 \\ 0 & 0 & 0 \end{bmatrix} \\
&= \left(U_2 \begin{bmatrix} 0 & 0 & 0 \\ 0 & \Delta_{21} & 0 \\ 0 & 0 & 0 \end{bmatrix} U_2^{\dagger} + \begin{bmatrix} A & 0 & 0 \\ 0 & 0 & 0 \\ 0 & 0 & 0 \end{bmatrix}\right) + U_2 \begin{bmatrix} 0 & 0 & 0 \\ 0 & 0 & 0 \\ 0 & 0 & \Delta_{31} \end{bmatrix} U_2^{\dagger} \\
&= M_1 + M_2
\end{aligned} \tag{8.31}
$$

In one-mass-square-dominance (OMSD) scenario, we can assume that $\Delta_{21} \ll \Delta_{31}$. If we put $\Delta_{21} = 0$ in the equation 8.31, we get

$$
M_{matter}^2 = \begin{bmatrix} \Delta_{31}\sin^2\theta_{13} + A & 0 & \Delta_{31}\sin\theta_{13}\cos\theta_{13} \\ 0 & 0 & 0 \\ \Delta_{31}\sin\theta_{13}\cos\theta_{13} & 0 & \Delta_{31}\sin^2\theta_{13} \end{bmatrix} \tag{8.32}
$$

and the matter modified PMNS matrix in OMSD approximation is

$$U^{OMSD} = \begin{bmatrix} \cos\theta_{13}^m & 0 & \sin\theta_{13}^m \\ -\sin\theta_{23}\sin\theta_{13}^m \exp^{i\delta_{CP}} & \cos\theta_{23} & \sin\theta_{23}\cos\theta_{13}^m \exp^{i\delta_{CP}} \\ -\cos\theta_{23}\sin\theta_{13}^m \exp^{i\delta_{CP}} & -\sin\theta_{23} & \cos\theta_{23}\cos\theta_{13}^m \exp^{i\delta_{CP}} \end{bmatrix}$$
(8.33)

where

$$\tan 2\theta_{13}^m = \frac{\Delta_{31}\sin 2\theta_{13}}{\Delta_{31}\cos 2\theta_{13} - A}$$
(8.34)

The oscillation probabilities then become

$$P_{ee}^m = 1 - \sin^2 2\theta_{13}^m \sin^2\left(\frac{1.27\Delta_{31}^m L}{E}\right)$$
(8.35)

$$P_{\mu e}^m = \sin^2\theta_{23}\sin^2 2\theta_{13}^m \sin^2\left(\frac{1.27\Delta_{31}^m L}{E}\right)$$
(8.36)

$$P_{\mu\mu} = 1 - \cos^2\theta_{13}^m \sin^2 2\theta_{23}\sin^2\left(\frac{1.27(\Delta_{31}^m + A + \Delta_{31})L}{E}\right)$$
$$- \sin^2\theta_{13}^m \sin^2 2\theta_{23}\sin^2\left(\frac{1.27(\Delta_{31} + A - \Delta_{31}^m)L}{E}\right)$$
$$- \sin^4\theta_{23}\sin^2 2\theta_{13}^m \sin^2\left(\frac{1.27\Delta_{31}^m L}{E}\right) \quad (8.37)$$

where

$$\Delta_{31}^m = \sqrt{(\Delta_{31}\cos 2\theta_{13} - A)^2 + (\Delta_{31}\sin 2\theta_{13})^2}$$
(8.38)

According to definition if $m_3 > m_1$ it is known as Normal Hierarchy (NH), but in case of $m_1 > m_3$ it is called Inverted Hierarchy (IH). Reactor neutrino experiments have established that the value of $\theta_{13} < 45°$, which makes $\cos 2\theta_{13}$ always positive. According to the definition of matter potential in case of neutrinos $A > 0$ but for anti-neutrinos $A < 0$. Putting all this information in equation 8.34 we see that if NH is true, for neutrinos a resonance is possible making the mixing

angle θ_{13} larger than its value in vacuum, and if IH is true for anti-neutrinos a resonance is possible making the mixing angle θ_{13} larger than its value in vacuum. But if NH is true then no resonance is present for anti-neutrinos and similarly for neutrinos, in case of IH no resonance is present. These dissimilarities motivated the design of INO. In presence of earth matter, the flux of neutrinos will get modified if NH is true, and will be left unaltered for IH. But the opposite will be observed in case of anti-neutrinos.

Matter vs Vacuum Oscillation in Atmospheric Neutrinos

The pioneering water Cerenkov detectors, IMB [53, 54] and Kamiokande [55, 56], observed the up down asymmetry of atmospheric muon neutrinos and established atmospheric neutrino anomaly. The next generation experiment, Super-Kamiokande [57], measured the zenith angle dependence of atmospheric muon and electron neutrinos and established atmospheric neutrino oscillations. The initial analysis of Super-Kamiokande data was done using the hypothesis of two flavor vacuum oscillations, which provided a good fit to the data. It also has determined the magnitude of the corresponding mass-squared difference $|\Delta_{atm}| \simeq 3 \times 10^{-3}$ eV^2 (but not its sign) and the mixing angle $\sin^2 2\theta_{atm} \simeq 1$. This determination played an important role in the design of the long-baseline accelerator neutrino experiments T2K [122] and NOνA [123].

Evidence for neutrino oscillations also came from solar neutrino experiments [33, 34, 35, 36, 37, 38]. Analysis of the solar neutrino data yielded the result

$\Delta_{sol} \sim 10^{-4}$ eV^2 and $\sin^2 \theta_{sol} \sim 0.3$. The three known light neutrino flavor states [124] can mix to form three mass eigenstates with masses m_1, m_2 and m_3. From these, we can define two *independent* mass-square differences, $\Delta_{21} = m_2^2 - m_1^2$ and $\Delta_{31} = m_3^2 - m_1^2$. Without loss of generality, we can identify $\Delta_{sol} = \Delta_{21}$ and $\Delta_{atm} = \Delta_{31} \approx \Delta_{32}$. The unitary mixing matrix, connecting the flavor eigenstates to the mass eigenstates, is called the PMNS matrix [31, 32]. In a manner similar to the quark mixing matrix [125, 126], it is parameterized in terms of three mixing angles, θ_{12}, θ_{13} and θ_{23}, and a CP violating phase δ_{CP}. The data from the CHOOZ reactor neutrino experiment leads to the strong constraint $\theta_{13} \leq 10°$ [42, 43]. The smallness of this mixing angle implies that the solar and the atmospheric neutrino anomalies can be analyzed as independent problems within the three flavor oscillation framework [43]. It also leads to the identification $\theta_{sol} \simeq \theta_{12}$ and $\theta_{atm} \simeq \theta_{23}$.

The solar neutrinos, produced at the core of the sun, undergo forward elastic scattering as they travel through the solar matter. This scattering leads to matter effect [26, 127, 24], which modifies the solar electron neutrino survival probability (P_{ee}). Super-Kamiokande [37] and SNO [38] have measured P_{ee} as a function of neutrino energy for $E > 5$ MeV and found it to be of a constant value ≈ 0.3. SNO has also measured [38] the neutral current interaction rate of solar neutrinos to be consistent with predictions of the standard solar model [13]. These results, together with CHOOZ bound on θ_{13}, provide a $5\,\sigma$ evidence for the matter effects in solar neutrinos [128]. The measurements of the ^{71}Ga experiments [34, 35, 36] imply that $P_{ee} > 0.5$ for neutrino energies $E < 0.5$ MeV. This increase in P_{ee} at lower energies can be explained only if Δ_{21} is *positive*.

The up going atmospheric neutrinos travel thousands of kilometers through

earth, during which they undergo forward elastic scattering with earth matter. They also experience the matter effect [26, 127] which modifies their of survival and oscillation probabilities. As in the case of the solar neutrinos, this modification depends on the sign of the mass-square difference, which, in this case, is Δ_{31}. Given the different magnitudes of

- Δ_{21} and Δ_{31},

- the energies of solar and atmospheric neutrinos and

- the solar and earth matter densities,

the matter modification of atmospheric neutrino probabilities are of a different mathematical form compared to their solar neutrino counterparts [129, 130]. An observation of these matter modifications can establish the sign of Δ_{31}. A number of studies [131, 58, 132, 133] considered matter modified oscillations and explored the sensitivity of future atmospheric neutrino detectors to determine whether hierarchy is NH or IH. Recently, SK experiment analyzed their data using the hypothesis of matter modified oscillations. Their results indicate that the vacuum oscillations are disfavored at $1.6\,\sigma$ only [134]. They prefer NH and disfavor IH at $1.7\,\sigma$.

At present, the most precise determination of $|\Delta_{31}|$ and $\sin^2 2\theta_{23}$ comes from the muon neutrino disappearance data of the accelerator neutrino experiments, such as MINOS [135], T2K [136] and NOνA [137]. For baselines less than 1000 km, the matter effects lead to negligibly small changes in $\nu_\mu/\bar{\nu}_\mu$ survival probabilities [138, 139]. Thus, the $\nu_\mu/\bar{\nu}_\mu$ disappearance data of accelerator neutrino experiments lead to essentially the same values of $|\Delta_{31}|$ and $\sin^2 2\theta_{23}$

for the three cases: (a) vacuum oscillations, (b) matter oscillations with NH and
(c) matter oscillations with IH. It is important to develop methods to make a
distinction between these three hypotheses. Without such a distinction, it will
be impossible to measure the CP violating phase δ_{CP} in neutrino oscillations
because matter effects mimic CP violation [140, 141]. In the present work, we
explore how this distinction can be made with future atmospheric neutrino data.
Disentangling the changes induced in the oscillation probabilities by the matter
effects and by δ_{CP} is non-trivial in general. In an atmospheric neutrino detector,
the interaction rate of ν_μ ($\bar{\nu}_\mu$) depends on both the survival probability $P_{\mu\mu}$ ($P_{\bar{\mu}\bar{\mu}}$)
and the oscillation probability $P_{e\mu}$ ($P_{\bar{e}\bar{\mu}}$). However, it has been shown that the
sensitivity of this rate to matter effects does not depend on the value of δ_{CP}
[58]. Hence, this data can lead to a distinction between the three hypotheses,
independent of the value of δ_{CP}.

The $\nu_e/\bar{\nu}_e$ appearance data in long-baseline accelerator neutrino experiments
is sensitive to matter effects [142, 143]. A precise measurement of the oscillation
probabilities, $P_{\mu e}$ and $P_{\bar{\mu}\bar{e}}$, in principle, can make a distinction among the three
possibilities. However, this data is also sensitive to δ_{CP} which at present is poorly
determined. Given measured values of $P_{\mu e}$ and $P_{\bar{\mu}\bar{e}}$ can have three solutions [144,
145]:

- vacuum oscillations with δ_{CP}^1,

- NH matter oscillations with δ_{CP}^2 and

- IH matter oscillations with δ_{CP}^3.

For each type of oscillating hypothesis, the value of δ_{CP} determined turns out

to be different. Since the determination of δ_{CP} is one of the important goals of future long-baseline accelerator neutrino experiments, making a distinction between the three hypotheses through independent data is crucial.

At present, the data of T2K and NOνA are analyzed using the matter modified oscillation hypothesis with both NH and IH. T2K prefers NH and disfavors IH at 2 σ [146]. It prefers δ_{CP} close to $-\pi/2$ for both NH and IH [147]. NOνA also prefers NH, but it disfavors IH only at 1 σ [148]. In the case of NH, NOνA allows the full range of δ_{CP} within 1 σ, though it prefers $-\pi/2$ for IH. Very recently, NOνA updated its results on hierarchy and δ_{CP} [149]. It still prefers NH with a wide allowed range of δ_{CP} but also has a large 1 σ allowed region for IH around $\delta_{CP} \simeq -\pi/2$. A combined analysis of the latest data of T2K and NOνA [150] mildly prefers IH over NH (with a $\Delta\chi^2 = 1.8$) whereas the combined analysis of T2K and NOνA data along with that of Super-Kamiokande shows a mild preference for NH over IH (with a $\Delta\chi^2 = 2.2$). The combined data of T2K and NOνA **do not show** any discrimination between vacuum and matter modified oscillations with NH [151].

9.1 Vacuum vs. Matter Modified Oscillations

The mixing between the neutrino flavor eigenstates and the mass eigenstates is given by

$$\begin{bmatrix} \nu_e \\ \nu_\mu \\ \nu_\tau \end{bmatrix} = U \begin{bmatrix} \nu_1 \\ \nu_2 \\ \nu_3 \end{bmatrix}, \tag{9.1}$$

where U is a 3×3 unitary PMNS matrix. It is parameterized as

$$U = \begin{bmatrix} 1 & 0 & 0 \\ 0 & c_{23} & s_{23} \\ 0 & -s_{23} & c_{23} \end{bmatrix} \begin{bmatrix} c_{13} & 0 & s_{13}e^{-i\delta_{CP}} \\ 0 & 1 & 0 \\ -s_{13}e^{i\delta_{CP}} & 0 & c_{13} \end{bmatrix} \begin{bmatrix} c_{12} & s_{12} & 0 \\ -s_{12} & c_{12} & 0 \\ 0 & 0 & 1 \end{bmatrix}. \quad (9.2)$$

For neutrino propagation in vacuum, the oscillation probabilities depend on the six parameters: the two mass-squared differences, $\Delta_{21} = m_2^2 - m_1^2$ and $\Delta_{31} = m_3^2 - m_1^2$, the three mixing angles and δ_{CP}. At present, Δ_{21}, $|\Delta_{31}|$, θ_{12} and θ_{13} are measured quite precisely. In case of the third mixing angle, $\sin^2 2\theta_{23}$ is measured to be close to 1 but $\sin^2 \theta_{23}$ has a rather large range of $(0.4 - 0.64)$. As mentioned in the introduction, the sign of Δ_{31} is not known at present.

The effect of neutrino propagation in matter is parameterized by the Wolfenstein matter term $A = 0.76 \times 10^{-4} \rho$ *(in gm/cc)* E *(in GeV)* [26, 127]. Inclusion of this matter term in neutrino evolution induces a change in the mass-square differences and the mixing angles, and hence in the probabilities. In this work, it has been studied how this change can be utilized to make a distinction between vacuum and matter modified oscillations. This change depends on not only the matter term but also on the sign of Δ_{31}. Hence, both positive and negative values of Δ_{31} have been considered.

First the difference between matter and vacuum oscillation probabilities for two representative path-lengths for atmospheric neutrinos, $L = 5000$ km and $L = 8000$ km have been studied. Figure 9.1 shows the plots of neutrino and anti-neutrino oscillation probabilities $P_{e\mu}$ and $P_{\bar{e}\bar{\mu}}$ and survival probabilities $P_{\mu\mu}$ and $P_{\bar{\mu}\bar{\mu}}$ for vacuum oscillations as well as for matter modified oscillations with NH. The matter modified probabilities have been calculated numerically using the code **nuCraft** [87], which uses the earth density profile of the PREM model

[152]. From the expressions for the oscillation probabilities, it can be shown that the probabilities for IH can be obtained via the relations $P_{\mu\mu}(IH) = P_{\bar{\mu}\bar{\mu}}(NH)$, $P_{\bar{\mu}\bar{\mu}}(IH) = P_{\mu\mu}(NH)$, $P_{\mu e}(IH) = P_{\bar{\mu}\bar{e}}(NH)$ and $P_{\bar{e}\bar{\mu}}(IH) = P_{e\mu}(NH)$ [139]. From figure 9.1, it has been observed that, the matter effects increase the peak value of $P_{\mu e}$ from 0.05 to 0.2 (0.5) for L = 5000 (8000) km and these peak values occur at nearly the same energy were $P_{\mu\mu}$ also peaks. Conservation of probability implies that either $P_{\mu\mu}$ or $P_{\mu\tau}$ should decrease significantly. The maximum of $P_{\mu\mu}$ generally coincide with the minimum of $P_{\mu\tau}$ and it can be shown that the change in the value of $P_{\mu\tau}$ near its minimum is very small [139, 153]. Hence, most of the reduction in the probability occurs in $P_{\mu\mu}$. Thus, $P_{\mu\mu}$ for matter, oscillations with NH is lower than $P_{\mu\mu}$ for vacuum oscillations over a wide range of energies and path-lengths. But $P_{\bar{\mu}\bar{\mu}}$ is essentially the same for both the cases. In the case of IH, the situation is reversed. Therefore, to study the difference of vacuum oscillations from matter modified oscillations of either sign, it is important to measure neutrino and anti-neutrino event rates separately. In this work, the sensitivity of Iron Calorimeter (ICAL) at the India-based Neutrino Observatory (INO) to make a distinction between vacuum and matter modified oscillations using atmospheric neutrino data has been studied. The charge identification capability of ICAL leads to a very good sensitivity for this distinction [59].

9.2 Methodology

The atmospheric neutrinos consist of ν_μ, $\bar{\nu}_\mu$, ν_e and $\bar{\nu}_e$. The ICAL at INO is a 50 kt magnetized iron calorimeter whose iron plates are interspersed with the
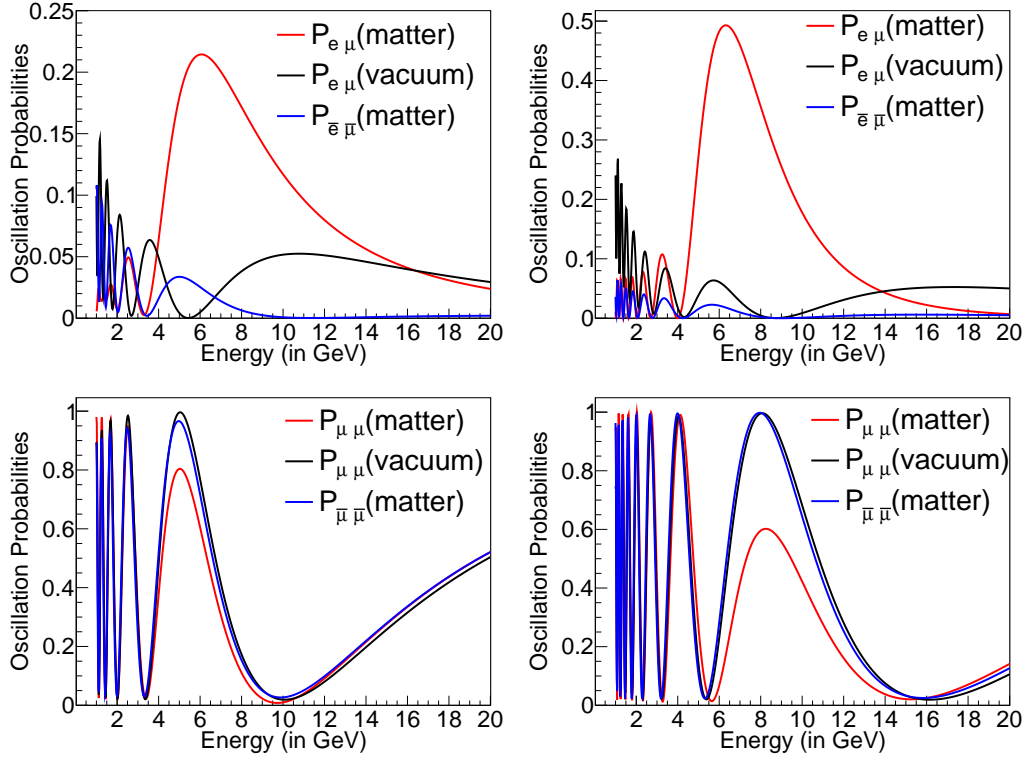
Figure 9.1: Probability vs Energy plots for the case of NH. The top row shows the oscillation probabilities $P_{e\mu}$ and $P_{\bar{e}\bar{\mu}}$ for L = 5000 km (left panel) and L = 8000 km (right panel). The bottom row shows the survival probabilities $P_{\mu\mu}$ and $P_{\bar{\mu}\bar{\mu}}$ for L = 5000 km (left panel) and L = 8000 km (right panel). The neutrino parameters used for generating these plots, $\sin^2\theta_{12} = 0.310$, $\sin^2\theta_{13} = 0.02240$, $\sin^2\theta_{23} = 0.582$, $\Delta_{21} = 7.39 \times 10^{-5}$ eV^2 and $\Delta_{31} = 2.525 \times 10^{-3}$ eV^2, are the global best-fit values [154]. The CP violating phase δ_{CP} is taken to 0.

active detector elements, Resistive Plate Chambers (RPCs). The charge current (CC) interactions of the neutrinos in the detector produce μ^- or μ^+ or e^- or, e^+ depending on the flavor of the initial neutrino.

NUANCE event generator [76] has been used to simulate the atmospheric neutrino events used in this study. It generates neutrino events using atmospheric neutrino fluxes and the relevant cross-sections. For a generated event, NUANCE gives the information on the particle ID and the momenta of all interacting particles. The information of the final state particles is given as an input to

a GEANT4 simulator of ICAL. This simulator mimics the response of ICAL and generates the electronic signals of the detector in the form of a hit bank information as the output. A reconstruction program sifts through the hit bank information of each event and tries to reconstruct a track. Electrons and positrons in the final state produce a shower and quickly lose their energy. Identifying such particles and reconstructing their energy is an extremely difficult problem. Muons, being minimum ionizing particles, pass through many layers of iron, leaving behind localized hits in the RPCs. Using this hit information, the track of the muon can be reconstructed. Because of the magnetic field, this track will be curved and the bending of the track is opposite for negative and positive muons. Thus, ICAL can distinguish between the CC interactions of ν_μ and $\bar{\nu}_\mu$. If a track is reconstructed, the event is considered to be a CC interaction of $\nu_\mu/\bar{\nu}_\mu$. The charge, the momentum and the initial direction ($\cos\theta_{track}$), of a reconstructed track, are also calculated from the track properties [84].

Un-oscillated atmospheric neutrino events for 500 years of exposure have been generated using NUANCE. In generating these events, the neutrino fluxes at Kamioka has been used as input along with ICAL geometry. The $\nu_\mu/\bar{\nu}_\mu$ CC events are given as input to GEANT4 and the GEANT4 output is processed by the reconstruction code. Events for which one or more tracks are reconstructed are stored along with the charge, the momentum and the initial direction of the track with the largest momentum. These track variables will be used later in the analysis to bin the events. In the case of $\nu_e/\bar{\nu}_e$ CC events, the electron/positron are redefined to be μ^-/μ^+ and the events are processed through GEANT4 and the reconstruction code. Once again the charge, the momentum and the initial direction of the track with the largest momentum are stored. This redefinition

of $\nu_e/\bar{\nu}_e$ CC events is done so that the events which undergo $\nu_e(\bar{\nu}_e) \rightarrow \nu_\mu(\bar{\nu}_\mu)$ oscillation are properly taken into account in the analysis.

The vacuum oscillation probabilities, $P_{\mu\mu}$, $P_{\bar{\mu}\bar{\mu}}$, $P_{e\mu}$ and $P_{\bar{e}\bar{\mu}}$, have been calculated for three flavor oscillations. Using these probabilities, accept/reject method has been applied on the un-oscillated sample to obtain the oscillated event sample. The corresponding matter modified probabilities, for both signs of Δ_{31}, have been calculated numerically using the code **nuCraft** [87]. The accept/reject method has been applied to $\nu_\mu(\bar{\nu}_\mu)$ CC events using $P_{\mu\mu}(P_{\bar{\mu}\bar{\mu}})$ to obtain the muon events due to the survival of $\nu_\mu/\bar{\nu}_\mu$. The same method has been applied to $\nu_e(\bar{\nu}_e)$ CC events using $P_{e\mu}(P_{\bar{e}\bar{\mu}})$ to obtain the muon events due to the oscillation of $\nu_e/\bar{\nu}_e$. The track information for each of the selected events has been taken from the simulation described in the previous paragraph.

9.3 Results

Using the procedure described in the previous section, the muon event sample for matter modified oscillations has been generated with Δ_{31} positive. In calculating the oscillation probabilities for this case, the following values of neutrino parameters have been used as inputs [154]: $\sin^2 \theta_{12} = 0.310$, $\sin^2 \theta_{13} = 0.02240$, $\sin^2 \theta_{23} = 0.582$, $\Delta_{31} = 2.525 \times 10^{-3}$ eV^2 and $\Delta_{21} = 7.39 \times 10^{-5}$ eV^2. Initially, the calculation has been done with the input value $\delta_{CP} = 0$. Later, it has been shown that our sensitivity to matter effects does not depend on the input value of δ_{CP}. The generated sample has been divided into μ^- and μ^+ samples and further subdivided into 17 track momentum bins and 90 track direction bins. The momentum bins are $(1, 2), (2, 2.2), (2.2, 2.4), (2.4, 2.6), (2.6, 2.8), (2.8, 3.0), (3.0, 3.5), (3.5, 4.0),$

$(4.0, 4.5)$, $(4.5, 5.0)$, $(5.0, 6.0)$, $(6.0, 7.5)$, $(7.5, 9.0)$, $(9.0, 11.0)$, $(11.0, 14.0)$, $(14.0, 20.0)$, $(20.0, 100.0)$. Only those events with track momentum greater than 1 GeV have been considered because such events lead to good track reconstruction. The signature of oscillations is very small for the down going events, and it is almost impossible to reconstruct tracks of muons moving in horizontal direction. Therefore, only the up going events with $\cos\theta_{track}$ in the range $(0.1, 1)$ have been considered. Since ICAL can reconstruct the muon direction very accurately, the above range have been subdivided into bins of equal width 0.01. Using this procedure, two binned event samples, N_{ij}^{data,μ^-} and N_{ij}^{data,μ^+} have been generated, and treated as data. Here i refers to the track momentum bin and varies from 1 to 17 and j refers to $\cos\theta_{track}$ bin and varies from 1 to 90.

The vacuum oscillation has been considered as a hypothesis to be tested against the data samples described above. Using the vacuum oscillation hypothesis, two other event samples, N_{ij}^{vac,μ^-} and N_{ij}^{vac,μ^+}, have been generated using the same procedure described in the previous paragraph. In calculating the vacuum oscillation probabilities the five inputs, $\sin^2\theta_{12} = 0.310$, $\sin^2\theta_{13} = 0.02240$, $\Delta_{31} = 2.525\times10^{-3}$ eV^2, $\Delta_{21} = 7.39\times10^{-5}$ eV^2 and $\delta_{CP} = 0$, have been held fixed. The test values of $\sin^2\theta_{23}$ have been varied in the range $(0.4, 0.64)$. To quantify the difference between matter and vacuum oscillations, $\Delta N_{ij}^{\mu^-} = N_{ij}^{vac,\mu^-} - N_{ij}^{data,\mu^-}$ and $\Delta N_{ij}^{\mu^+} = N_{ij}^{vac,\mu^+} - N_{ij}^{data,\mu^+}$ have been defined. In figure 9.2, $\Delta N_i^{\mu^-} = \Sigma_j \Delta N_{ij}^{\mu^-}$ and $\Delta N_i^{\mu^+} = \Sigma_j \Delta N_{ij}^{\mu^+}$ as a function of track momentum have been plotted. Figure 9.3 gives the plots of $\Delta N_j^{\mu^-} = \Sigma_i \Delta N_{ij}^{\mu^-}$ and $\Delta N_j^{\mu^+} = \Sigma_i \Delta N_{ij}^{\mu^+}$ as a function of track direction. It has been observed that $\Delta N_i^{\mu^\mp}$, in general, are positive because the matter effects suppress the peak values of $P_{\mu\mu}$ and the magnitude of $\Delta N_i^{\mu^-}$ is larger than that of $\Delta N_i^{\mu^+}$ for Δ_{31} positive. The situation is reversed when Δ_{31}

is negative. This, of course, is a reflection of the fact that the matter effects are more pronounced in $P_{\mu\mu}$ for positive value of Δ_{31} and in $P_{\bar{\mu}\bar{\mu}}$ for negative values of Δ_{31}. A similar pattern has been observed in $\Delta N_j^{\mu^{\mp}}$, for the same reasons.
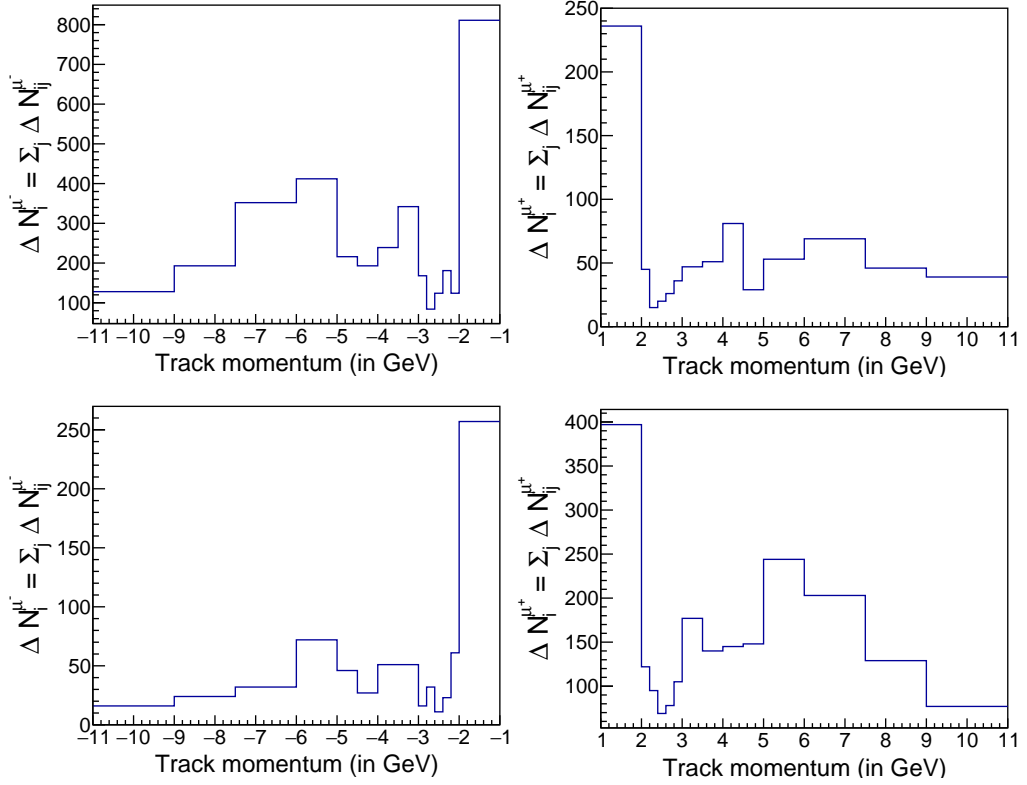
Figure 9.2: The difference between the number of muon events for matter vs. vacuum oscillations ($\Delta N_i^{\mu^{\mp}}$) as a function of track momentum. The plots in the left (right) panels are for μ^- (μ^+) events. The plots in the top (bottom) panels are for Δ_{31} positive (negative).

The test event samples N_{ij}^{test,μ^-} and N_{ij}^{test,μ^+} have been calculated as

$$N_{ij}^{test,\mu^-/\mu^+} = N_{ij}^{vac,\mu^-/\mu^+}[1 + \pi_{ij}^k \xi_k], \tag{9.3}$$

where three systematic errors π_{ij}^k ($k = 1, 2, 3$), each with its pull parameter, ξ_k have been introduced. The first of these is the systematic error in flux normalization, which is independent of track momentum and track direction. The second
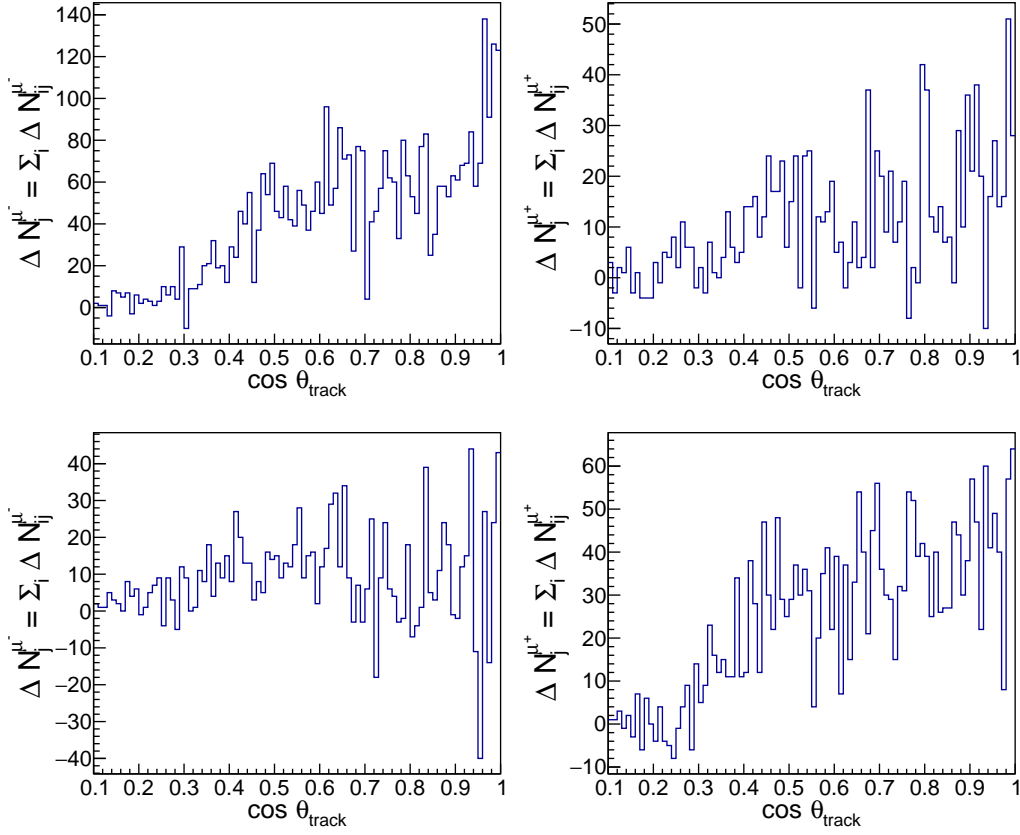
Figure 9.3: The difference between the number of muon events for matter vs. vacuum oscillations ($\Delta N_j^{\mu^{\mp}}$) as a function of $\cos\theta_{track}$. The plots in the left (right) panels are for μ^- (μ^+) events. The plots in the top (bottom) panels are for Δ_{31} positive (negative).

systematic error depends on the track momentum, and the third one depends on track direction. The method of calculation of the last two systematic errors is described in the appendix. The χ^2 between the data and the test event samples has been calculated by

$$\chi^2 = \chi^2(\mu^-) + \chi^2(\mu^+) + \xi_k^2, \tag{9.4}$$

where

$$\chi^2(\mu^-) = \Sigma_{i=1}^{17}\Sigma_{j=1}^{90} 2\left[\left(N_{ij}^{test,\mu^-} - N_{ij}^{data,\mu^-}\right) - N_{ij}^{data,\mu^-}\ln\left(\frac{N_{ij}^{test,\mu^-}}{N_{ij}^{data,\mu^-}}\right)\right], \quad (9.5)$$

$$\chi^2(\mu^+) = \Sigma_{i=1}^{17}\Sigma_{j=1}^{90} 2\left[\left(N_{ij}^{test,\mu^+} - N_{ij}^{data,\mu^+}\right) - N_{ij}^{data,\mu^+}\ln\left(\frac{N_{ij}^{test,\mu^+}}{N_{ij}^{data,\mu^+}}\right)\right], \quad (9.6)$$

and priors on the pull parameters ξ_k^2 are added. For each test value of $\sin^2\theta_{23}$, the minimum value of χ^2 has been computed by varying the pull parameters ξ_k in the range $(-3, 3)$ in steps of 0.1. The χ^2 for a ten-year exposure has been obtained by dividing the minimum χ^2 by 50. This χ^2 is a measure of ICAL sensitivity to distinguish vacuum oscillations from matter oscillations with Δ_{31} positive.

In calculating the vacuum oscillation probabilities, $\Delta_{21}, \Delta_{31}, \theta_{12}, \theta_{13}$ and δ_{CP} has been held fixed. However, each of these parameters has an associated uncertainty. Varying Δ_{21} and θ_{12} has very little effect on the atmospheric neutrino oscillation probabilities. So these parameters have been kept fixed for the whole calculation. The variation in the two parameters, Δ_{31} and $\sin^2\theta_{13}$, can lead to a noticeable change in the probabilities and hence in the event rates. Therefore, these two parameters have been varied and marginalized over them. The vacuum probabilities have been calculated for various different test values of $\sin^2\theta_{13}$ and Δ_{31}. These test values have been chosen within the $\pm 2\ \sigma$ ranges of the central values of the respective parameters. The χ^2 has been computed with the addition

of the following priors

$$\chi^2_{prior}(\theta_{13}) = \left(\frac{\sin^2\theta_{13}^{test} - 0.0224}{\sigma_{\sin^2\theta_{13}}}\right)^2, \tag{9.7}$$

$$\chi^2_{prior}(\Delta_{31}) = \left(\frac{\Delta_{31}^{test} - 2.525 \times 10^{-3}}{\sigma_{\Delta_{31}}}\right)^2, \tag{9.8}$$

where $\sigma_{\sin^2\theta_{13}} = 0.00066$ and $\sigma_{\Delta_{31}} = 0.033 \times 10^{-3}$ eV^2 [154]. It has been found that the minimum χ^2 occurred when the values of $\sin^2\theta_{13}$ and Δ_{31} in the vacuum probability are the same as the central values.
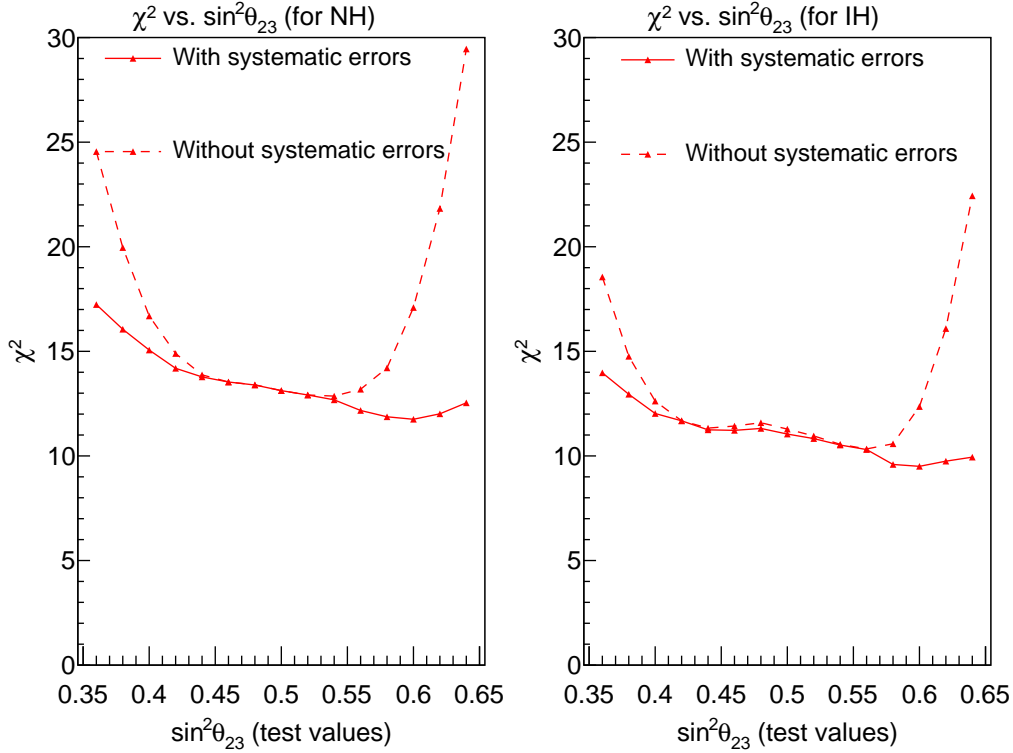
Figure 9.4: Sensitivity of ICAL to matter vs. vacuum oscillations as a function of $\sin^2\theta_{23}$(test). The CP violating phase δ_{CP} is set equal to 0 for both matter and vacuum oscillations.

After calculating ICAL sensitivity to distinguish vacuum oscillations from matter oscillations with Δ_{31} positive, this calculation has been repeated for the

case where Δ_{31} is negative. Our results are shown in figure 9.4 where the left panel is for Δ_{31} positive and the right panel is for Δ_{31} negative. Each panel shows the variation of χ^2 as a function of the test values of $\sin^2\theta_{23}$, without and with the systematic errors. It has been observed that the χ^2 without systematic errors is relatively flat for $\sin^2\theta_{23}$(test) in the range, $(0.4, 0.6)$ but rises sharply outside this range. This behavior can be explained by close examination of the difference between the values of $P_{\mu\mu}$ near its minimum for the two cases of matter modified oscillations and vacuum oscillations, as shown in figure 9.5. From this figure, it can be noted that, values of $P_{\mu\mu}$ near the low energy minimum are very close for matter modified oscillations with NH and for vacuum oscillations with test values of $\sin^2\theta_{23}$ varying in the range $(0.4, 0.6)$. But, for test value of $\sin^2\theta_{23}$ away from this range, these differences become bigger. And the contribution from all these energy values leads to a significant rise in the χ^2. The uncertainty in flux normalization, which is common to all the bins, is fairly large. Due to the systematic error in the flux normalization, the χ^2 occurring due to the differences near the $P_{\mu\mu}$ minima regions is drastically reduced, whereas the χ^2 occurring due to the large difference near the $P_{\mu\mu}$ maxima regions is relatively unaffected. Hence, the χ^2 with systematic errors is relatively flat with respect to all the test values of $\sin^2\theta_{23}$.

It has been observed that $\chi^2_{min} = 11.8$ for Δ_{31} positive and is 9.5 for Δ_{31} negative. Hence, ICAL can rule out vacuum oscillations at better than 3 σ confidence level, if the matter effects, as prescribed by Wolfenstein [26, 127], are present. This sensitivity is there for both the signs of Δ_{31}. The sensitivity obtained is for the input values of $\sin^2\theta_{23} = 0.582$ and $\sin^2 2\theta_{13} \approx 0.09$, which are the current best-fit values from the analysis of global data [154]. This sensitivity
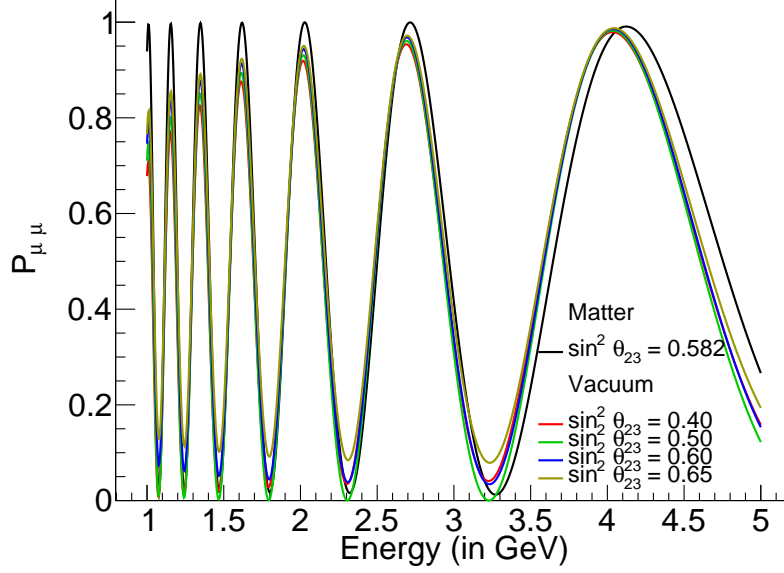
Figure 9.5: $P_{\mu\mu}$ plots for the energy range $E = (1.0, 5.0)$ GeV. Shown are the matter modified probability for $\sin^2 \theta_{23} = 0.582$ and vacuum probabilities for the test values of $\sin^2 \theta_{23} = 0.4, 0.5, 0.6$ and 0.65.

is slightly larger than that obtained for hierarchy discrimination for ICAL in previous studies. For example, fig 5.7 of ref. [59], gives the hierarchy sensitivity of ICAL for different input values of mixing angles and exposures. The ten-year hierarchy sensitivity, for $\sin^2 \theta_{23} = 0.6$ and $\sin^2 2\theta_{13} = 0.1$, is shown to be 11.5, independent of whether the true hierarchy is normal or inverted.

It should, however, be noted that the method of analysis used here is very different from that used in previous studies. The kinematic variables used here are track momentum and track direction which are obtained from the reconstruction of the GEANT simulation of atmospheric neutrino events [84], whereas in the previous studies the kinematic variables are the NUANCE output information on muon, smeared with resolution functions. A detailed comparison of the results from the old method and from the new method is beyond the scope of this paper.

The results presented in figure 9.4 assumed δ_{CP} to be zero for both matter and vacuum oscillations. However, the sensitivity should be checked if the test value of δ_{CP} is varied over its full range $(0, 360°)$. To perform this calculation, we have kept the true value of $\delta_{CP} = 0$ for matter oscillation probabilities and considered the four test values $\delta_{CP} = 0, 90°, 180°, 270°$ for vacuum oscillations. The minimum χ^2, as a function of test, δ_{CP} has been shown in figure 9.6. It was observed that this marginalization over δ_{CP} has essentially no effect on the minimum χ^2. The χ^2_{min} values are 11.7 for positive Δ_{31} and 9.5 for negative Δ_{31}. Recent global fits to neutrino oscillation data yield the best fit value of $\delta_{CP} \approx 270°$ for both signs of Δ_{31} [154]. The calculations have been redone with $\delta_{CP} = 270°$ as our input value in matter oscillation probabilities and marginalized over the full range of the test values of δ_{CP}. The minimum χ^2 has occurred for the test value $180°$. The values of minimum χ^2 are 11.8 for Δ_{31} positive and 9.3 for Δ_{31} negative.

It is worth exploring the role of charge identification capability of ICAL in the discrimination sensitivity. To do this, the μ^- and μ^+ event samples have been combined into a single sample and computed the χ^2 between the matter and vacuum oscillated distributions, including the systematic uncertainties and marginalization over the oscillation parameters. The results have been shown in figure 9.7, which show that the sensitivity reduces a factor of 2 if the charge identification is not there.

Recently, Super-Kamiokande collaboration performed an analysis of atmospheric neutrino oscillation data along with external constraints [134]. They also searched for evidence of matter effects in this data. They parameterized the matter term in the form α **∗ the standard matter effect** and varied α in the range
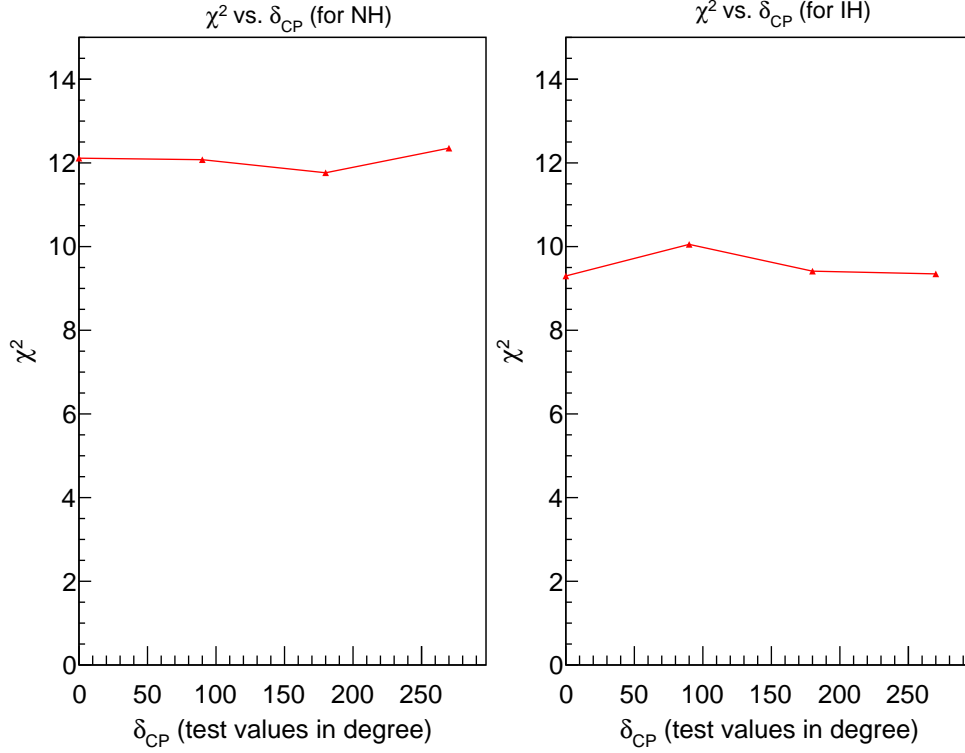
Figure 9.6:   Sensitivity of ICAL to matter vs. vacuum oscillations as a function of test values of δ_{CP}. This phase is set equal to 0 for matter oscillations and is varied over four test values for vacuum oscillations.

$(0, 2)$. Vacuum oscillations correspond to $\alpha = 0$ and standard matter oscillations correspond to $\alpha = 1$. The best fit point occurred for Δ_{31} positive and $\alpha = 1$. Vacuum oscillations were disfavored with $\Delta \chi^2 = 5$. Negative Δ_{31}, for all values of α, was disfavored with $\Delta \chi^2$ in the range $(5 - 6)$. Similar analysis has been carried out for ICAL also. Matter modified oscillation events have been generated for both NH and IH and tested this "data" against the hypothesis of *partial matter effect* oscillations, as parameterized by Super-Kamiokande. The results are presented in the figure 9.8, which confirms that the vacuum oscillations, given by $\alpha = 0$, are ruled out with $\chi^2 = 11.5$ for NH (left panel) and with $\chi^2 = 9.5$ for IH (right panel). It has also been found that ICAL is very effective in ruling out
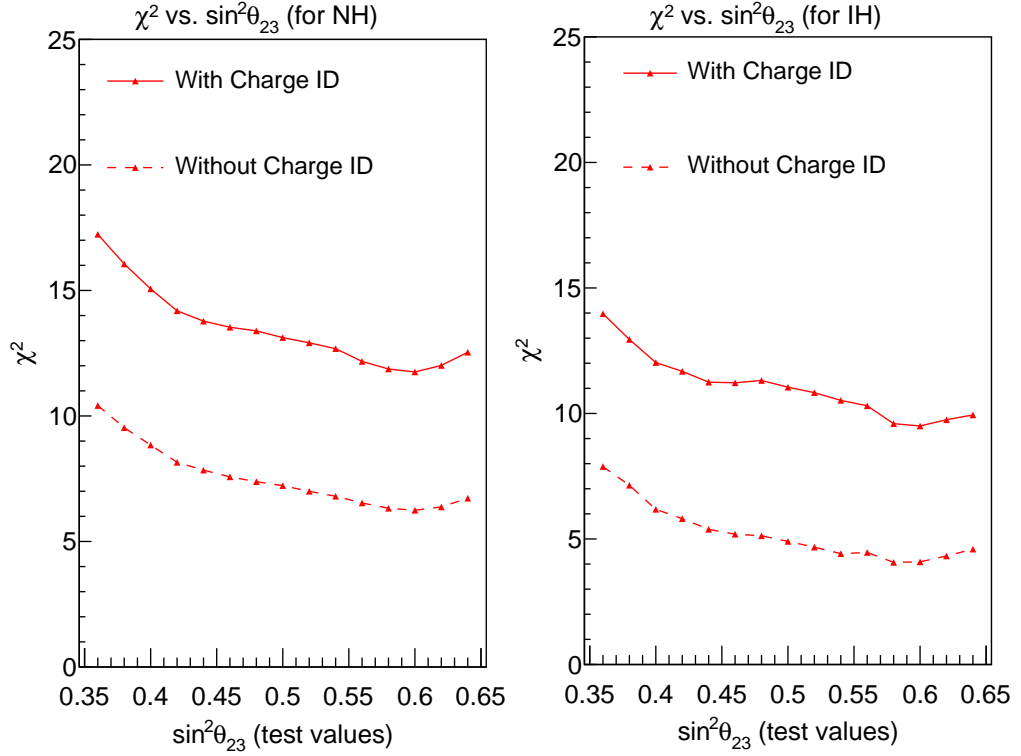
Figure 9.7: Sensitivity of ICAL to matter vs. vacuum oscillations, as a function of test values of $\sin^2 \theta_{23}$ **with and without charge identification**.

the wrong hierarchy for all values of α.

Both atmospheric neutrino data and accelerator neutrino data give a consistent picture of neutrino oscillations driven by a mass-squared difference of about 2.5×10^{-3} eV^2 and a nearly maximal mixing angle. However, the present data can not effectively distinguish between vacuum oscillations and matter modified oscillations. It is important to make this distinction because our ability to determine the CP violating phase δ_{CP} depends on it. In this paper, the sensitivity of ICAL at INO has been considered to make a distinction between these two types of oscillations. It has been found that a ten-year exposure leads to a better than $3\,\sigma$ distinction, whether Δ_{31} is positive or negative. The difference between the
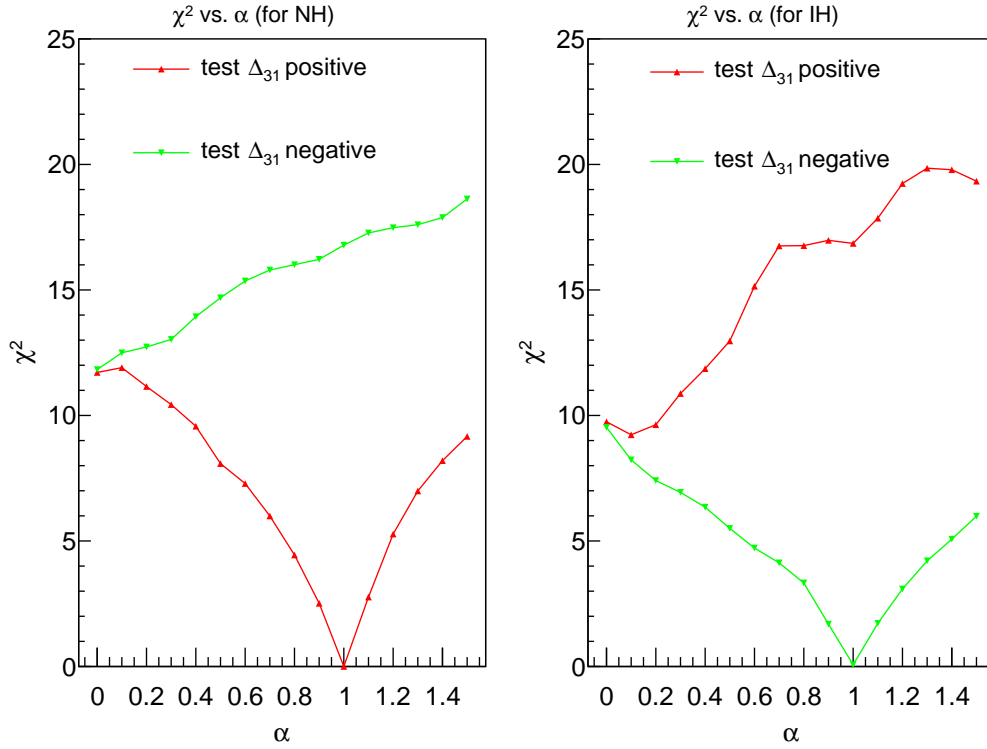
Figure 9.8: Sensitivity of ICAL to fractional matter effects for NH (left panel) and IH (right panel).

matter and vacuum oscillations is significant for neutrinos if Δ_{31} is positive and for anti-neutrinos if Δ_{31} is negative. Hence, the charge identification capability of ICAL has an important role in giving rise to such good distinguishing ability. This ability is independent of the true value of δ_{CP}. With no charge identification, the discrimination ability is reduced by half.

Neutrino Oscillation Parameter Determination Using GEANT4 Reconstructed Event Information

One of the important physics goals of ICAL is to measure the oscillation parameters of atmospheric neutrinos with improved precision. The ability of ICAL to reconstruct the muon momentum and direction with good accuracy plays an important role in achieving the above goal. The first analysis [61], which estimated the precision in neutrino oscillation parameters possible at ICAL, used the NU-ANCE output information of muon energy and direction. The detector resolution was incorporated by means of smearing the energy and direction distributions with the corresponding spreads. A later analysis [62] followed the same procedure but used the hadron energy, defined to be the difference between neutrino and muon energies given by NUANCE, as a third variable. It was shown that the addition of a third variable led to a significant improvement in the precision of the

135

neutrino oscillation parameters. However, the detector effects, especially ICAL's ability to reconstruct muon momentum and direction, were not included. A realistic estimate of ICAL's capability towards parameter precision must include its reconstruction ability. The first step along this direction was taken in the work of Rebin et al. [63], where atmospheric neutrino events were simulated in the detector through GEANT4 simulator and the reconstruction program was used to determine the two kinematical variables, track momentum and track direction. The neutrino oscillation parameters were estimated using these two reconstructed variables. The results of [63] are summarized in table 10.1.

Parameter	Input Value	Reconstructed Best Fit Point	2 σ Range	3 σ Range
$|\Delta_{31}|(10^{-3}\ \mathrm{eV}^2)$	2.32	2.32	2.03	4.07
$\sin^2\theta_{23}$	0.5	0.496	0.38	0.48

Table 10.1: Result obtained in ref. [63] for 5 year exposure.

In this section, the analysis has been extended by including a third variable, which represents the hadron energy of an atmospheric neutrino event. It has been found that the inclusion of this third variable leads to a noticeable improvement in the precision of the mass squared difference, but the precision of the mixing angle shows little improvement.

10.1 Methodology

10.1.1 Data and Theory sample

The analysis has started with 500 years of un-oscillated events generated by NUANCE, with Kamiokande fluxes as input. From this, a 5-year event sample

has been isolated. The oscillated event sample has been generated by using accept/reject method on the above sample. The oscillation probabilities, $P_{\mu\mu}$ and $P_{\bar{\mu}\bar{\mu}}$, have been calculated using the three flavor oscillation code **nuCraft** [87]. The following values of neutrino oscillation parameters have been used as inputs: $\sin^2\theta_{12} = 0.310$, $\sin^2\theta_{13} = 0.02240$, $\sin^2\theta_{23} = 0.5$, $\Delta_{31} = 2.32 \times 10^{-3}$ eV^2, $\Delta_{21} = 7.39 \times 10^{-5}$ eV^2 and $\delta_{CP} = 0$. The accept/reject method is applied to $\nu_\mu(\bar{\nu}_\mu)$ CC events using $P_{\mu\mu}(P_{\bar{\mu}\bar{\mu}})$ to obtain the muon events due to the survival of $\nu_\mu/\bar{\nu}_\mu$. The muon CC events occurring due to the oscillation of $\nu_e(\bar{\nu}_e)$ are negligibly small because $\sin^2\theta_{13} \ll 1$. Hence, they are not included in this analysis. This 5 year event sample is labeled **data**.

To calculate the corresponding theoretical event sample, with test values of neutrino oscillation parameters, the following method has been followed. A test value of $|\Delta_{31}|$ from the range $(1, 5) \times 10^{-3} eV^2$ and a test value of the $\sin^2\theta_{23}$ in the range $(0, 1)$ have been chosen. The test values of $|\Delta_{31}|$ have been varied systematically in steps of 0.2×10^{-3} eV^2 in the range $(1, 5) \times 10^{-3}$ eV^2 and $\sin^2\theta_{23}$ in steps of 0.02 in the range $(0, 1)$. The other neutrino oscillation parameters have been kept fixed at the input values which were used to generate the data event sample. The three flavor muon neutrino survival probabilities, $P_{\mu\mu}$ and $P_{\bar{\mu}\bar{\mu}}$, have been calculated using the code nuCraft [87]. The rest 495 year un-oscillated muon event sample has been converted into an oscillated event sample through accept-reject method using the above probabilities.

10.1.2 Variables for Analysis

Muons, being minimum ionizing particles, pass through many layers of iron, leaving behind localized hits in the RPCs. Using this hit information, the track of the muon can be reconstructed. Because of the magnetic field, this track will be curved and the bending of the track is opposite for negative and positive muons. Thus ICAL can distinguish between the CC interactions of ν_μ and $\bar{\nu}_\mu$. If a track has been reconstructed, the event has been considered to be a CC interaction of $\nu_\mu/\bar{\nu}_\mu$. The charge, the momentum and the initial direction ($\cos\theta_{track}$), of a reconstructed track, are also calculated from the track properties [84]. Electrons, positrons and photons lose their energy very quickly and leave no track. Pions pass through a few layers, and it is difficult to construct a track for them unless they are of very high energy. Baryons have very low kinetic energy and can pass through one or two layers. Therefore, the hadrons produced in these reactions leave a few ($0 - 10$) scattered hits [81, 155]. Thus, the GEANT4 simulation of a typical $\nu_\mu/\bar{\nu}_\mu$ CC event consists of a track and a few hadron hits.

Events for which one or more tracks have been reconstructed are stored along with the charge, the momentum and the initial direction of the track with the largest momentum. The leftover hits, that is the hits which are not used for track reconstruction, have been labelled hadron hits. In dealing with the hadron hits, the problem of ghost hits needs to be considered. If the actual hits occurred at (x_1, y_2), (x_2, y_1) and (x_3, y_1) the simulation only tells us that the x-strips x_1, x_2, x_3 and the y-strips y_1, y_2 are hit. This leads to the possibility of there being six hits, three of which are ghost hits. This problem can be solved very simply by defining the number of hadron hits to be the maximum of *(number of x-strips, number of*

y-strips) with hits.

In this analysis, the following variables have been used, which are given as the output of the GEANT4 simulator and the track reconstruction program. For about 90% of the events, only one track is reconstructed. Multitracks are reconstructed for the other 10% of the events. For single track events, the variables used are (a) the absolute value of the track momentum, (b) the direction of the track and (c) the total number of non-track hits. For multitrack events, the variables used are (a) the sum of absolute values of all the track momenta, (b) the direction of the longest track and (c) the total number of non-track hits. This work concentrates only in the parameters $|\Delta_{31}|$ and $\sin^2 \theta_{23}$ but not in matter effect. Therefore, $\nu_\mu/\bar{\nu}_\mu$ CC events have been considered together, and the muon charge information has not been used. This improves the statistics in each bin. The time information of the events have not been used explicitly. The time stamps of hits, however, were used by the reconstruction program in determining the track direction. Since the co-ordinates of the hits are not relevant for this work, we need not worry about the ghost hits.

10.1.3   Analysis Methods

The analysis have done using two different binning schemes. These schemes are labeled as **2-Variable Analysis** and **3-Variable Analysis**:

- 2-Variable Analysis In this analysis method, the events have been binned according to the modulus of their reconstructed track momentum and their reconstructed track direction. For the events where more than one track have been reconstructed, the track momentum and direction are those of the

longest track. There are 10 momentum bins given by $(0.1, 0.5)$, $(0.5, 1.0)$, $(1.0, 1.5)$, $(1.5, 2.0)$, $(2.0, 2.5)$, $(2.5, 3.0)$, $(3.0, 5.0)$, $(5.0, 10.0)$, $(10.0, 20.0)$, $(20.0, 100.0)$. There are 40 direction bins spanning the range $(-1, 1)$ in steps of 0.05. This analysis uses 400 bins in the double differential distribution of the two variables.

- 3-Variable Analysis This analysis method incorporates additional information compared to two variable analysis method. We classified events into four classes based on E, the total track momentum, and $|\cos\theta_{track}|$, where θ_{track} is the direction of the longest reconstructed track. The four classes are:

  1. High energy, horizontal events with $E > 10$ GeV and $|\cos\theta_{track}| < 0.3$, with 2 * 12 = 24 bins.

  2. High energy, vertical events with $E > 10$ GeV and $|\cos\theta_{track}| > 0.3$, with 2 * 28 = 56 bins.

  3. Low energy, horizontal events with $E < 10$ GeV and $|\cos\theta_{track}| < 0.3$, with 8 * 12 = 96 bins.

  4. Low energy, vertical events with $E < 10$ GeV and $|\cos\theta_{track}| > 0.3$, with 8 * 28 = 224 bins.

For atmospheric neutrinos, the number of events at high energies is small and for ICAL the reconstruction ability for horizontal events is poor. Hence, the number of events in each bin of the first three classes are too small to be further subdivided based on non-track hits. Hence, the events in these 176 bins have been binned only in the two variables E and $\cos\theta_{track}$. Binning in the third variable,

non-track hits, has been done only for the 224 bins of low energy, vertical events. The bins used for the third variable are $(0, 4)$, $(5, 10)$ and > 10.

The **data** and the **theory** samples have been binned according to the scheme described above. Each entry of the **theory** sample is divided by **99**. Thus, the theoretical prediction for a five-year muon event sample has been obtained if the values of the oscillation parameters were equal to the chosen test values. Since this **theory** event sample is generated by scaling a huge generated sample, it is expected that the effect of fluctuations in each entry is negligibly small. On the other hand, event number fluctuations are expected to distort both the track momentum and track direction distributions in the **data** event sample.

10.1.4 Systematic Errors and χ^2 Calculation

The **theory** event sample is calculated using standard inputs for atmospheric neutrino fluxes and cross-sections. However, these inputs have uncertainties associated with them. They have been taken into account as systematic errors through the method of pulls. Usually three systematic errors are considered: a) Normalization error, b) Energy dependent tilt error and c) Zenith angle dependent error. The second and third errors are defined in terms of neutrino energy and direction, respectively. But in our analysis, the variables used are track momentum and direction. Hence, the systematic errors specified as functions of neutrino energy and direction have to be transformed into functions of track momentum and track direction. Following the method used in [156] the neutrino energy dependent tilt error has been transformed to track momentum dependent tilt error and neutrino direction dependent error has been transformed to recon-

structed track direction dependent error. These two errors have been assumed to be independent of each other. As described in the 3-variable binning scheme, some events have been binned using the non-track hit information. An overall 5% systematic error has been considered for each of those bins. This has been assumed to be independent of the momentum and direction of the longest track. The method of pulls has been used to apply the systematic errors.

N_{ijk}^{test} has been defined as

$$N_{ijk}^{test} = N_{ijk}^{theory}[1 + \pi_{ijk}^l]\xi_l, \tag{10.1}$$

where ξ_l is the pull variable for the systematic error l, varied in the range -3 to 3 in step of 0.5. The pull coefficient π_{ijk}^l is for the lth systematic error. The first three systematic errors are flux normalization dependent error(π_{norm}), track momentum dependent tilt error (π_{tilt}), track direction dependent error (π_{dir}) and the last one is systematic error (π_{had}) taken for each non-track hit information bin in case of 3 variable analysis. A constant value of 0.2 has been assumed for π_{norm} and 0.05 for π_{had}. The χ^2 between the data and test event samples is

$$\chi^2 = \Sigma_i \Sigma_j \Sigma_k \left[2 \left\{ \left(N_{ijk}^{test} - N_{ijk}^{data} \right) - N_{ijk}^{data} ln \left(\frac{N_{ijk}^{test}}{N_{ijk}^{data}} \right) \right\} \right] + \xi_l^2, \tag{10.2}$$

where the prior terms ξ_l^2 have been added in the pull variables. This χ^2 is a function of the test values of $|\Delta_{31}|$ and $\sin^2 \theta_{23}$. For each pair of test values of $|\Delta_{31}|$ and $\sin^2 \theta_{23}$, χ^2 is computed, and the minimum χ^2 is evaluated. The test values corresponding to minimum χ^2 are the best fit values of $|\Delta_{31}|$ and $\sin^2 \theta_{23}$.

10.2 Results

10.2.1 Procedure to Calculate Best fit point, $2\,\sigma$ and $3\,\sigma$ range

The procedure described above has been carried out for 25 mutually independent 5 year muon data samples, which are selected randomly. The value of $\Delta\chi^2$ for each of the data sample has been plotted as function of $|\Delta_{31}|$ and function of $\sin^2\theta_{23}$. From these plots, for each data sample, the value of $|\Delta_{31}|$ and $\sin^2\theta_{23}$ have been found out for which $\Delta\chi^2$ is minimum. This value of the oscillation parameter has been noted down as the best fit point for that data sample. Next, for each data sample, the range of the oscillation parameters which cannot be ruled out at $2\,\sigma$ and $3\,\sigma$ confidence level have been calculated. For this the values of the parameters for which $\Delta\chi^2$ is 4 and 9 have been noted down. These correspond to the $2\,\sigma$ and $3\,\sigma$ limit, respectively. It has been observed that for some samples, the upper bound of $2\,\sigma$ and $3\,\sigma$ for $|\Delta_{31}|$ lies outside the corresponding test value range. For those samples it has been assumed that the upper bound of $2\,\sigma$ is $7\times10^{-3}eV^2$ and that for $3\,\sigma$ range is $10\times10^{-3}eV^2$. Once the $2\,\sigma$ and $3\,\sigma$ limits of the oscillation parameters for each of the data sample have been calculated, the respective range has been found out by subtracting the lower bound from the upper bound. To find out the uncertainty for each of the analysis method, the best fit point, $2\,\sigma$ and $3\,\sigma$ range have been averaged over the 25 mutually exclusive sets. In the following sections, the results for 5 year and 10 year exposure time and 2-Variable analysis and 3-variable analysis have been discussed.

10.2.2 Results for 5 and 10 year exposure time

The results obtained for $\sin^2\theta_{23}$ and its allowed ranges in 2 σ and 3 σ are comparable for 2-variable analysis and for 3-variable analysis. On the other hand, the allowed ranges for $|\Delta_{31}|$ show a noticeable improvement for 3-variable analysis compared to 2-variable analysis. In figure 10.1 we have compared the allowed range of the two variables for both 2-variable and 3-variable analysis methods for one of such set. For example, for five years exposure, the 2-Variable analysis does not give an upper limit in the explored range at 2 σ in 2 of the 25 cases, whereas the 3-variable analysis does so for every case. Such an example is shown in figure 10.2. If the exposure is increased to 10 years, the corresponding numbers are one and zero respectively. The average allowed ranges of $|\Delta_{31}|$, both at 2 σ and at 3 σ, are smaller for 3-variable analysis compared to 2-variable analysis. The results for 5 year exposure are summarized in tables 10.2 and 10.3 and those for 10 years exposure are summarized in tables 10.4 and 10.5.

10.3 Conclusion

First, we compare the results of our analysis: 2-variable vs 3-variable and 5 years vs 10 years exposure. From table 10.6, we see that both the 2 σ and 3 σ ranges of $|\Delta_{31}|$ from the 3-variable analysis are smaller by a factor of 1.5 compared to the corresponding ranges of the 2-variable analysis for a 5-year exposure. On the other hand, the ranges of $\sin^2\theta_{23}$, both 2 σ and 3 σ, are the same for 2 and 3-variable analyses. For a 10-year exposure, the parameter ranges are smaller compared to the 5-year exposure, but the relation between the ranges of 2 and 3-variable analyses are similar to those of 5 year exposure. The

((a)) Allowed ranges for 2-variable analysis method.

((b)) Allowed ranges for 3-variable analysis method.
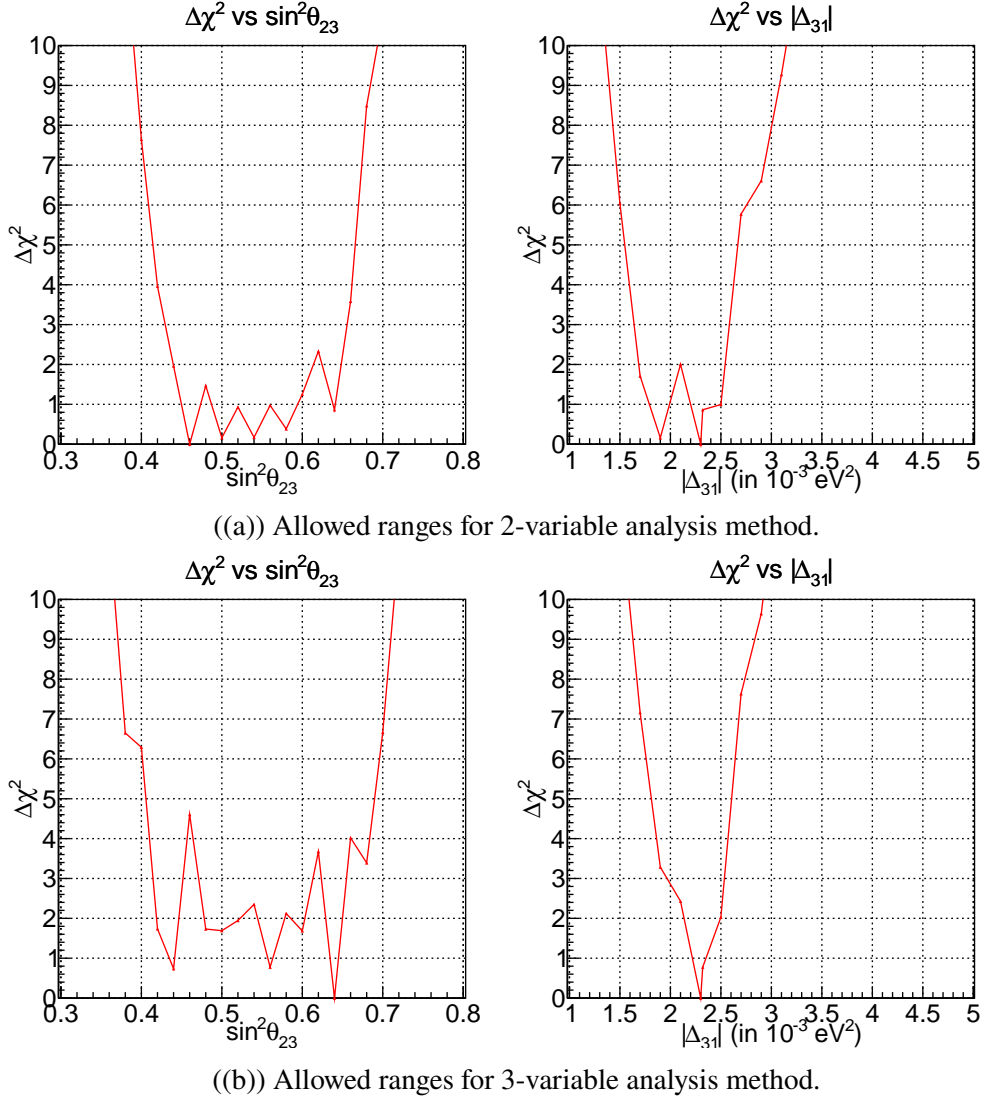
Figure 10.1: Comparison between 2-variable and 3-variable analysis methods for one of the randomly selected sample set.

precision in $|\Delta_{31}|$ is greatly improved by the inclusion of the third variable. In conclusion, we find that the precision in $\sin^2 \theta_{23}$ improves by negligible amount by the inclusion of the third variable. The precision on $|\Delta_{31}|$ on the other hand improves by 32% when the third variable is included. The three variable analysis method takes care of the energy of the other particles produced in the neutrino

((a)) Allowed ranges for 2-variable analysis method.

((b)) Allowed ranges for 3-variable analysis method.
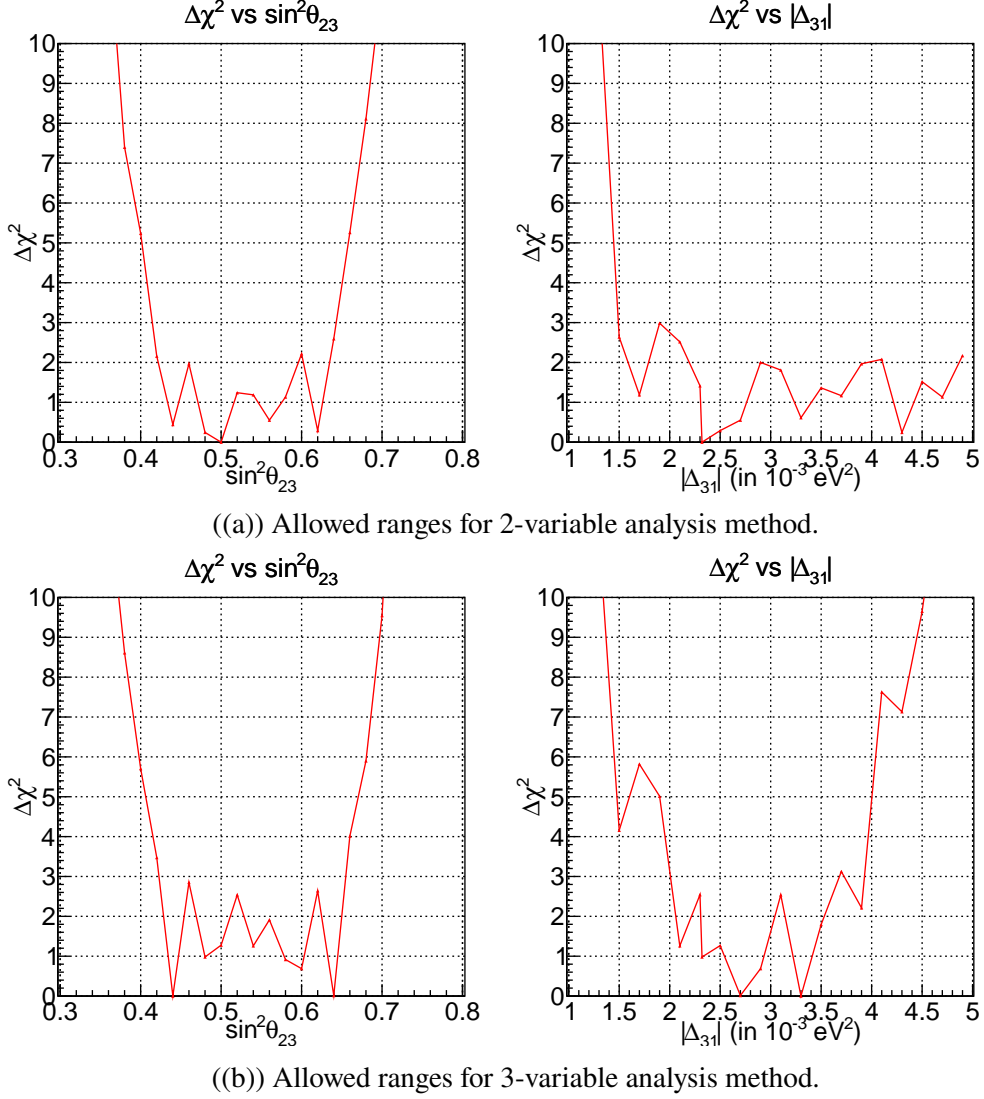
Figure 10.2: Comparison between 2-variable and 3-variable analysis methods for one of the randomly selected sample set.

CC interactions. The parameter Δ_{31} being dependent on the value of L/E_ν can be measured more precisely if we have better reconstruction of neutrino energy E_ν. On the other hand, $\sin^2 \theta_{23}$ is measured from the oscillation dip. The better the dip is reconstructed, the more precise it will become. This has been observed when we increased the exposure time to 10 years.

$|\Delta_{31}|(*10^{-3}eV^2)$						
Set Number	Binning Scheme	$3\,\sigma$ Lower Bound	$2\,\sigma$ Lower Bound	Best Fit Point	$2\,\sigma$ Upper Bound	$3\,\sigma$ Upper Bound
Set1	2-variable	1.55	1.7	2.7	3.25	3.7
	3-variable	1.62	2.12	2.9	3.5	4.76
Set2	2-variable	1.35	1.6	2.3	2.6	3.1
	3-variable	1.62	1.88	2.3	2.56	2.86
Set3	2-variable	1.9	2.32	3.3	4.9	-
	3-variable	1.56	1.74	2.1	2.62	3
Set4	2-variable	1.65	2	3.5	4	-
	3-variable	1.56	2.32	2.5	3.18	3.94
Set5	2-variable	1.6	2	2.9	4.55	-
	3-variable	1.14	1.38	2.32	2.94	3.44
Set6	2-variable	1.4	1.65	2.32	3.1	4.7
	3-variable	1.62	1.88	2.3	3.56	4.84
Set7	2-variable	1.3	1.5	2.32	-	-
	3-variable	1.4	1.96	2.7	3.96	4.46
Set8	2-variable	1.55	2.3	2.9	4.9	-
	3-variable	1.3	1.4	1.9	2.5	2.7
Set9	2-variable	1.3	1.6	2.3	2.75	3.15
	3-variable	1.7	1.9	2.32	2.6	3.1
Set10	2-variable	1.3	1.55	1.9	3.00	3.4
	3-variable	2.62	3.62	4.1	4.82	-
Average of 25 Sets	2-variable	1.53	1.80	2.43	3.43	5.13
	3-variable	1.67	1.99	2.53	3.19	4.13

Table 10.2: Best fit point, $2\,\sigma$ upper and lower limits and $3\,\sigma$ upper and lower limits of $|\Delta_{31}|$ for 10 of the 25 mutually exclusive data sets we considered. The exposure considered is 5 years. The values of the above five quantities averaged over the 25 sets have also been quoted. Of the 25 sets, 15 sets give smaller allowed range for 3-variable analysis compared to 2-variable analysis.

We now compare the results of our 5 year, 2-variable analysis with those of ref. [63]. The ranges obtained in our analysis are significantly smaller than those of ref. [63]. We believe this occurred due to the following reason. In the analysis of ref. [63] imposed a criterion of good reconstruction in choosing their events.

		$\sin^2 \theta_{23}$				
Set Number	Binning Scheme	$3\,\sigma$ Lower Bound	$2\,\sigma$ Lower Bound	Best Fit Point	$2\,\sigma$ Upper Bound	$3\,\sigma$ Upper Bound
Set1	2-variable	0.32	0.36	0.46	0.7	0.76
	3-variable	0.33	0.34	0.4	0.64	0.71
Set2	2-variable	0.39	0.42	0.48	0.66	0.68
	3-variable	0.37	0.41	0.64	0.68	0.71
Set3	2-variable	0.39	0.43	0.54	0.64	0.68
	3-variable	0.38	0.43	0.58	0.59	0.66
Set4	2-variable	0.4	0.46	0.52	0.6	0.63
	3-variable	0.43	0.47	0.58	0.61	0.64
Set5	2-variable	0.34	0.38	0.64	0.7	0.74
	3-variable	0.33	0.35	0.62	0.71	0.74
Set6	2-variable	0.37	0.45	0.52	0.65	0.68
	3-variable	0.34	0.4	0.6	0.67	0.71
Set7	2-variable	0.36	0.39	0.48	0.66	0.69
	3-variable	0.35	0.39	0.5	0.65	0.68
Set8	2-variable	0.42	0.45	0.54	0.62	0.64
	3-variable	0.4	0.45	0.52	0.59	0.66
Set9	2-variable	0.38	0.46	0.52	0.62	0.67
	3-variable	0.41	0.49	0.56	0.64	0.69
Set10	2-variable	0.38	0.41	0.54	0.64	0.69
	3-variable	0.41	0.46	0.5	0.63	0.66
Average of 25 Sets	2-variable	0.36	0.40	0.52	0.66	0.70
	3-variable	0.36	0.40	0.51	0.65	0.70

Table 10.3: Best fit point, 2 σ upper and lower limits and 3 σ upper and lower limits of $\sin^2 \theta_{23}$ for 10 of the 25 mutually exclusive data sets we considered. The exposure considered is 5 years. The values of the above five quantities averaged over the 25 sets have also been quoted. Of the 25 sets, 12 sets give smaller allowed range for 3-variable analysis compared to 2-variable analysis.

This restriction led to a loss of statistics, which in turn led to larger uncertainties.

In our analysis, we included all the reconstructed events. Due to larger statistics, the uncertainties we obtained are smaller.

$|\Delta_{31}|(*10^{-3}eV^2)$						
Set Number	Binning Scheme	$3\,\sigma$ Lower Bound	$2\,\sigma$ Lower Bound	Best Fit Point	$2\,\sigma$ Upper Bound	$3\,\sigma$ Upper Bound
Set1	2-variable	1.75	2.3	2.32	2.6	2.9
	3-variable	2.3	2.62	2.7	3.3	3.56
Set2	2-variable	1.8	2.2	2.32	2.5	2.8
	3-variable	2.12	2.24	2.3	2.5	2.68
Set3	2-variable	1.9	2.1	2.5	2.8	3.5
	3-variable	1.88	2	2.1	2.68	2.88
Set4	2-variable	1.85	2.1	3.1	3.35	3.6
	3-variable	1.62	1.94	2.5	2.88	3.62
Set5	2-variable	1.8	1.9	2.1	2.6	4.5
	3-variable	1.38	1.5	2.3	2.94	3.06
Set6	2-variable	1.7	2.1	2.3	3	4.15
	3-variable	1.62	1.82	2.3	2.56	2.82
Set7	2-variable	1.7	2.1	2.32	2.9	3.3
	3-variable	2.12	2.56	2.7	3.5	3.74
Set8	2-variable	1.7	2.1	2.5	3.35	3.5
	3-variable	1.74	2.3	2.5	2.68	2.94
Set9	2-variable	1.85	2	2.32	2.75	2.9
	3-variable	1.94	2.06	2.3	2.32	2.88
Set10	2-variable	1.65	1.8	2.1	2.75	3
	3-variable	2	2.38	2.9	3.06	3.8
Average of 25 Sets	2-variable	1.74	2.01	2.35	2.92	3.54
	3-variable	1.86	2.09	2.37	2.77	3.08

Table 10.4: Best fit point, $2\,\sigma$ upper and lower limits and $3\,\sigma$ upper and lower limits of $|\Delta_{31}|$ for 10 of the 25 mutually exclusive data sets we considered. The exposure considered is 10 years. We also quote the values of the above five quantities averaged over the 25 sets. Of the 25 sets, 18 sets give smaller allowed range for 3-variable analysis compared to 2-variable analysis.

$\sin^2 \theta_{23}$						
Set Number	Binning Scheme	$3\,\sigma$ Lower Bound	$2\,\sigma$ Lower Bound	Best Fit Point	$2\,\sigma$ Upper Bound	$3\,\sigma$ Upper Bound
Set1	2-variable	0.42	0.48	0.5	0.56	0.64
	3-variable	0.4	0.44	0.52	0.55	0.63
Set2	2-variable	0.45	0.48	0.54	0.59	0.64
	3-variable	0.41	0.51	0.52	0.57	0.65
Set3	2-variable	0.41	0.43	0.56	0.64	0.67
	3-variable	0.38	0.46	0.54	0.66	0.69
Set4	2-variable	0.46	0.51	0.54	0.57	0.61
	3-variable	0.49	0.41	0.54	0.55	0.6
Set5	2-variable	0.39	0.44	0.62	0.63	0.67
	3-variable	0.39	0.42	0.46	0.63	0.66
Set6	2-variable	0.41	0.54	0.58	0.64	0.66
	3-variable	0.39	0.46	0.62	0.66	0.7
Set7	2-variable	0.4	0.46	0.5	0.62	0.67
	3-variable	0.39	0.42	0.44	0.62	0.66
Set8	2-variable	0.4	0.43	0.54	0.59	0.64
	3-variable	0.42	0.47	0.54	0.62	0.65
Set9	2-variable	0.44	0.49	0.52	0.61	0.66
	3-variable	0.45	0.48	0.58	0.61	0.66
Set10	2-variable	0.42	0.45	0.56	0.61	0.65
	3-variable	0.44	0.52	0.54	0.58	0.64
Average of 25 Sets	2-variable	0.39	0.43	0.52	0.62	0.67
	3-variable	0.40	0.45	0.52	0.62	0.66

Table 10.5: Best fit point, $2\,\sigma$ upper and lower limits and $3\,\sigma$ upper and lower limits of $\sin^2 \theta_{23}$ for 10 of the 25 mutually exclusive data sets we considered. The exposure considered is 10 years. We also quote the values of the above five quantities averaged over the 25 sets. Of the 25 sets, 13 sets give smaller allowed range for 3-variable analysis compared to 2-variable analysis.

Method	Parameter	Input Value	Reconstructed Best Fit point	$2\,\sigma$ Range	$3\,\sigma$ Range
Ref. [63]	$|\Delta_{31}|(10^{-3}\text{ eV}^2)$	2.32	2.32	2.03	4.07
Ref. [63]	$\sin^2\theta_{23}$	0.5	0.496	0.38	0.48
5-yr, 2-var	$|\Delta_{31}|(10^{-3}\text{ eV}^2)$	2.32	2.43	1.63	3.6
5-yr, 2-var	$\sin^2\theta_{23}$	0.5	0.52	0.26	0.34
5-yr, 3-var	$|\Delta_{31}|(10^{-3}\text{ eV}^2)$	2.32	2.53	1.2	2.46
5-yr, 3-var	$\sin^2\theta_{23}$	0.5	0.51	0.25	0.34
10-yr, 2-var	$|\Delta_{31}|(10^{-3}\text{ eV}^2)$	2.32	2.35	0.91	1.8
10-yr, 2-var	$\sin^2\theta_{23}$	0.5	0.52	0.19	0.28
10-yr, 3-var	$|\Delta_{31}|(10^{-3}\text{ eV}^2)$	2.32	2.37	0.68	1.24
10-yr, 3-var	$\sin^2\theta_{23}$	0.5	0.51	0.17	0.26

Table 10.6: Comparison of uncertainty ranges from different methods.

Thesis Abstract

Name of the Student: Jaydeep Datta
Name of the CI/OCC: Bhabha Atomic Research Center   **Enrolment No.:** PHYS01201504022
Thesis Title: A Study of Alternative Gas Mixtures of RPC & Different Aspects of Neutrino Oscillation for ICAL at INO
Discipline: Physical Sciences   **Sub-Area of Discipline:** Experimental High Energy Physics
Date of viva voce: 28/07/2021 (28th July, 2021)

India-based Neutrino Observatory (INO) is an underground facility, which will house many low background experiments. Iron Calorimeter (ICAL) is one of them. To study different properties of neutrinos, ICAL will measure the zenith angle dependence of atmospheric neutrino and anti-neutrino fluxes. ICAL will have three modules. Each of them will consist of 151 layers of iron slabs interspersed with Resistive Plate Chambers (RPCs). The RPCs will detect the charged particles created in the neutrino nucleon interaction. This doctoral study is dedicated to improve different aspects of ICAL performance.

Physics goals of ICAL demand avalanche mode operation of the RPCs, which is fulfilled by using a gas mixture of R134a and SF_6. These gases are known for their high global warming potential. In search for an alternative eco-friendly gas mixture to operate RPCs without compromising the demands of ICAL, a simulation framework has been developed to simulate the efficiency and streamer probability of RPC from the first principle and has been validated by comparing the simulated results for various gases with experiments carried out as part of this study. The model has been used to propose an eco-friendly, inexpensive and non-flammable gas mixture of argon, carbon dioxide and nitrogen.

The next part discusses physics studies carried out for ICAL. The first project is related to the discrimination of matter effect from vacuum in atmospheric neutrino oscillation, which is imperative to break the degeneracy present in matter effect and CP violation. It has been found that ICAL has capability to discriminate matter effect from vacuum oscillation with 3σ confidence in 10 years, irrespective of mass hierarchy. The leptonic charge identification capability of ICAL plays a big role for such sensitivity.

To improve the precision in oscillation parameter measurement, an analysis method has been developed using non-track hit information along with the kinematical variables of the reconstructed muon tracks. Incorporation of statistical fluctuation and usage of reconstructed track information and non-track hit information makes the analysis method more realistic. It has been found that inclusion of hadron hit information has reduced the allowed ranges for the oscillation parameters by 30% with respect to the analysis method using only the reconstructed muon information.

Thesis Highlight

Name of the Student: Jaydeep Datta

Name of the CI/OCC: Bhabha Atomic Research Center   **Enrolment No.:** PHYS01201504022

Thesis Title: A Study of Alternative Gas Mixtures of RPC & Different Aspects of Neutrino Oscillation for ICAL at INO
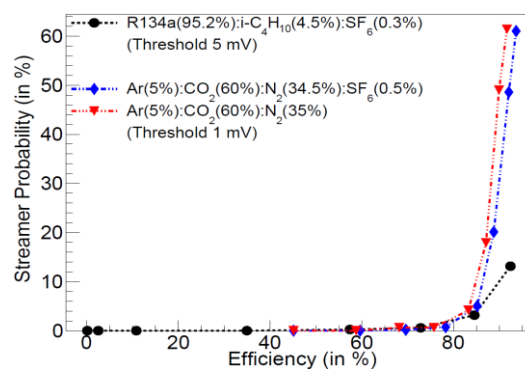
Discipline: Physical Sciences   **Sub-Area of Discipline:** Experimental High Energy Physics

Date of viva voce: 28/07/2021 (28th July, 2021)

India-based Neutrino Observatory (INO) is an underground facility, which will house many low background experiments. Iron Calorimeter (ICAL) is one of them. To study different properties of neutrinos, ICAL will measure the zenith angle dependence of atmospheric neutrino and anti-neutrino fluxes. ICAL will have three modules. Each of them will consist of 151 layers of iron slabs interspersed with Resistive Plate Chambers (RPCs). The RPCs will detect the charged particles created in the neutrino nucleon interaction. This doctoral study is dedicated to improve different aspects of ICAL performance.

Physics goals of ICAL demand avalanche mode operation of the RPCs, which is fulfilled by using a gas mixture of R134a and SF_6. These gases are known for their high global warming potential. In search for an alternative eco-friendly gas mixture to operate RPCs without compromising the demands of ICAL, a simulation framework has been developed to simulate the efficiency and streamer probability of RPC from the first principle and has been validated by comparing the simulated results for various gases with experiments carried out as part of this study. The model has been used to propose an eco-friendly, inexpensive and non-flammable gas mixture of

Figure 1: Comparison of streamer probability as function of efficiency between proposed Ar-based gas mixtures and R134a-based standard gas mixture.

argon, carbon dioxide and nitrogen. In figure 1 the proposed and standard gas mixture are compared on the basis of efficiency and streamer probability.

The next part discusses physics studies carried out for ICAL. The first project is related to the discrimination of matter effect from vacuum in atmospheric neutrino oscillation, which is imperative to break the degeneracy present in matter effect and CP violation. It has been found that ICAL has capability to discriminate matter effect from vacuum oscillation with 3σ confidence in 10 years, irrespective of mass hierarchy. The leptonic charge identification capability of ICAL plays a big role for such sensitivity.

To improve the precision in oscillation parameter measurement, an analysis method has been developed using non-track hit information along with the kinematical variables of the reconstructed muon tracks. Incorporation of statistical fluctuation and usage of reconstructed track information and non-track hit information makes the analysis method more realistic. It has been found that inclusion of hadron hit information has reduced the allowed ranges for the oscillation parameters by 30% with respect to the analysis method using only the reconstructed muon information.